TECHNISCHE UNIVERSITÄT WIEN
Vienna | Austria

AUTOMATION & CONTROL INSTITUTE
INSTITUT FÜR AUTOMATISIERUNGS- & REGELUNGSTECHNIK

Diplomarbeit

Design and Control of a Table-top Vibration Isolation System With Zero-Power Gravity Compensation

Ausgeführt zum Zwecke der
Erlangung des akademischen Grades
Diplom-Ingenieur (Dipl.-Ing.)

von
Benjamin Friedl, BSc, BSc (WU)
Matrikelnummer: 01612982

unter der Leitung von
Univ.-Prof. Dipl.-Ing. Dr.sc.techn. Georg Schitter
Associate-Prof. Dipl.-Ing. Dr.techn. Ernst Csencsics
Dipl.-Ing. Alexander Pechhacker

eingereicht am
Institut für Automatisierungs- und Regelungstechnik
Fakultät für Elektrotechnik und Informationstechnik
Technische Universität Wien

Wien, im Dezember 2023

Advanced Mechatronic Systems Group
Gußhausstraße 27-29, A-1040 Wien, www.acin.tuwien.ac.at

Acknowledgement

This thesis is the final part of my Master's degree in Energy Systems and Automation Technology. Certainly, it would not have the quality it has without the support and advice of my supervisors. I am therefore very grateful to Dipl.-Ing. Alexander Pechhacker and Associate-Prof. Dr.techn. Ernst Csencsics for sharing their profound expertise, and their tireless efforts to provide me with the best possible guidance during my work on this thesis. I am also indebted to Univ.-Prof. Dr.sc.techn. Georg Schitter for giving me the opportunity to realise this project, as well as for his helpful feedback and suggestions. Moreover, I would like to thank all my other colleagues at the research group for the very pleasant working atmosphere and their unfailing readiness to help.

I would also like to take this opportunity to express my deep gratitude to my family, who inspire and motivate me, and on whom I can always rely. I am particularly grateful to my parents Erika and Klaus, who always encouraged and supported me in my education and decisions. Also, I would like to thank my girlfriend Matylda for her patience, understanding and encouragement over the past year.

All this motivated me to give my best. Thank you.

Abstract

Vibration isolation is indispensable in many high-precision applications, both in industry and research. Prominent examples are wafer scanners, atomic force microscopes and large-scale reflecting telescopes. The stringent requirements cannot be met by purely passive systems and require active control strategies. Motivated by the high relevance, an active vibration isolation system with a levitating platform and zero-power gravity compensation is designed, implemented and evaluated in this thesis.

The levitating platform has six degrees of freedom (DoF), which are actuated by Lorentz actuators due to their linearity and quasi-zero stiffness. In order to avoid heat dissipation, which may have a negative effect on sensitive equipment, zero-power gravity compensation is integrated. This is achieved by using electropermanent magnets (EPM) which, compared to other approaches, enable the adaption to a variable payload mass while keeping the operating point of the platform constant.

Particular attention has to be paid to the control design due to the conflicting goals of position control and vibration suppression. For the positioning of the platform, decentralised control is used with a suitable decoupling of the six DoFs. The displacement is measured with six eddy current sensors. Moreover, the platform is equipped with an accelerometer, which is used to apply acceleration feedback. This increases the effective mass and reduces the transmission of floor vibrations. To achieve a lower position control bandwidth, which reduces the transmission of low-frequency disturbances, the negative stiffness of the EPMs is compensated by a positive virtual stiffness.

The decentralised position control achieves a bandwidth of 60 Hz in the out-of-plane DoFs and 20 Hz in the in-plane DoFs with a resolution of less than 100 nm. For vibration isolation, the crossover frequency of the position control in the vertical direction is reduced to 6 Hz, resulting in an attenuation of floor vibrations with $-40\,\mathrm{dB}$/decade starting at around 8 Hz. With the additional acceleration feedback, the transmissibility was further reduced by almost 10 dB. The evaluation of the gravity compensation showed that it can support a total load of 6.34 kg while reducing the power consumption by 98.9 %.

Kurzreferat

Die Unterdrückung unerwünschter Vibrationen ist bei vielen Präzisionsanwendungen, sowohl in der Industrie als auch in der Forschung, unverzichtbar. Prominente Beispiele hierfür sind Wafer-Scanner, Rasterkraftmikroskope und große Spiegelteleskope. Da die hohen Anforderungen durch rein passive Systeme nicht erfüllt werden können, sind aktive Vibrationsisolationssysteme erforderlich. Motiviert durch die hohe Relevanz wurde in der vorliegenden Arbeit ein solches System mit einer schwebenden Plattform und integrierter Gravitationskompensation entworfen, implementiert und evaluiert.

Die sechs Freiheitsgrade der schwebenden Plattform werden mittels Lorentz-Aktuatoren angesteuert. Um eine übermäßige Wärmeentwicklung zu vermeiden, die sich möglicherweise negativ auf empfindliche Messgeräte auswirkt, wurde eine leistungslose Gravitationskompensation vorgesehen. Hierzu kommen Elektropermanentmagnete (EPM) zum Einsatz, die im Vergleich zu anderen Ansätzen eine einfache Anpassung an die Nutzlast bei gleichbleibendem Arbeitspunkt ermöglichen.

Die Positionierung der Plattform erfolgt mittels einer dezentralen Regelung, was durch die Entkopplung der sechs Freiheitsgrade möglich ist. Die Auslenkung wird mit sechs Wirbelstromsensoren gemessen. Darüber hinaus ist die Plattform mit einem Beschleunigungssensor ausgestattet. Dieser ermöglicht es, die effektive Masse der Plattform durch Rückkopplung der Beschleunigung zu erhöhen und dadurch die Übertragung von Bodenvibrationen zu reduzieren. Um die Bandbreite der Positionsregelung zu verringern, wurde die negative Steifigkeit der EPMs durch eine positive virtuelle Steifigkeit kompensiert.

Mit der dezentralen Positionsregelung konnte in den out-of-plane Freiheitsgraden eine Bandbreite von 60 Hz und in den in-plane Freiheitsgraden 20 Hz bei einer Auflösung von unter 100 nm erreicht werden. Für die Vibrationsisolation wurde die Durchtrittsfrequenz der Positionsregelung in vertikaler Richtung auf 6 Hz reduziert, wodurch Bodenvibrationen ab einer Frequenz von etwa 8 Hz mit -40 dB/Dekade gedämpft wurden. Durch die zusätzliche Beschleunigungsrückkopplung wurde die Durchlässigkeit um weitere 10 dB verringert. Die Gravitationskompensation war in der Lage eine Gesamtlast von 6,34 kg zu tragen, während der Leistungsverbrauch um 98,9 % gesenkt wurde.

Contents

List of Figures

List of Tables

List of Abbreviations

3D	three-dimensional
AC	alternating current
ADC	analogue-to-digital converter
AFM	atomic force microscope
AlNiCo	aluminium-nickel-cobalt
CPU	central processing unit
DAC	digital-to-analogue converter
DC	direct current
DoF(s)	degree(s) of freedom
FEM	finite element method
FPGA	field-programmable gate array
IMU	inertial measurement unit
MEMS	microelectromechanical system
MIMO	multi-input multi-output
NdFeB	neodymium-iron-boron
PCB	printed circuit board
PI	proportional-integral
PID	proportional-integral-derivative
RMS	root mean square
SISO	single-input single-output
SNR	signal-to-noise ratio
SPI	Serial Peripheral Interface

Chapter 1

Introduction

Vibrations originate from various sources like human activity, traffic, heavy machinery or building motion, and are therefore present almost everywhere. Moreover, their intensity is increasing in areas such as automated production, driven by the demand for higher speeds and forces. These vibrations not only adversely affect human health and well-being, but also pose a challenge to production processes and research that necessitate increasingly precise conditions [1], [2]. Hence, their proper handling is required, to which this thesis is intended to make a contribution.

1.1 Motivation

The motivation for this thesis results from the indispensability of vibration isolation in many precision applications, which is illustrated by the examples presented in this section. The probably most important application is the mass production of high-performance semiconductor components, which form the foundation of the information age. They have found their way into almost every area of life, and their prevalence continues to grow. The production takes place in wafer scanners, which are regarded to be among the most sophisticated man-made machines, and requires positioning with sub-nanometre precision. This process can severely be affected by vibrations, which are not only transmitted from outside the plant, but also generated within due to the highly dynamic positioning processes. Therefore, sophisticated vibration isolation strategies are required [3]–[5].

This also applies to areas with less strict requirements on precision, but where powerful sources of vibration are present, like it is the case in industrial environments. Conducting precise in-line measurements, which are crucial for optimising both the throughput and quality of manufacturing processes, is only possible with the appropriate handling of disturbances [6].

Another field where vibration isolation plays an indispensable role is research. Without it, measurements at the atomic level, such as those performed with atomic force microscopes (AFM), would be impossible [7]. However, vibrations are not only problematic on a small scale, but also when measurements are done over long distances. Interferometers used to detect gravitational waves have optical path lengths in the kilometre range. At this distance, even very small deflections of the mirrors would lead to large errors [8]. This is also the case with large reflecting telescopes, which are made up of many individual segments [9].

In all these highly demanding applications, purely passive vibration isolation is not sufficient. As shown in the state of the art, these systems have inherent design constraints that can only be overcome by means of active approaches. This requires not only the implementation of appropriate control strategies, but also precision actuators and sensors.

1.2 Thesis Goals

Given the high relevance of vibration isolation in both industry and research, this thesis aims to design, implement and evaluate an active vibration isolation system suitable for table-top operation. In order to reduce the transmission of floor vibrations, the system should have a levitating platform with six degrees of freedom (DoF), on which the sensitive equipment is placed. Active levitation can cause high heat dissipation due to the continuous power consumption that is required to carry the payload. However, this must be avoided in high-precision applications, which usually require a constant temperature [10]. Therefore, a zero-power gravity compensation is required, which can easily be tuned to the mass of the payload and allows the operating point of the levitating platform to be kept constant.

The use case, from which the dimensions and requirements of the vibration isolation system are derived, is a table-top measuring instrument, such as an atomic force microscope (AFM), with outer dimensions of around 200 mm and a weight of 3 kg. The system should be able to lift the weight of the platform and the additional payload dynamically and require no significant power in static operation. The intended frequency range for the suppression of vibrations is 5 to 100 Hz, since usually this is the most critical in practical applications [2]. Above this frequency range, disturbances are attenuated anyway due to the inertia of the mass.

The specific objectives of this thesis are as follows:

- Design and implementation of a compact table-top vibration isolation system with a levitating 6-DoF platform and tunable zero-power gravity compensation.
- Design and implementation of an integrated control system for the positioning of the platform in all six DoFs and the suppression of floor vibrations in a frequency range of 5 to 100 Hz.
- Evaluation of the system performance in terms of position control, gravity compensation and vibration isolation.

1.3 Thesis Outline

The first part of the thesis provides an insight into the properties and limitations of passive vibration isolation. Subsequently, active control strategies for vibration isolation as well as the required actuators and sensors are presented. Also, two methods for gravity compensation are discussed, and the research questions of this thesis are derived. Chapter 3 is dedicated to the design of the platform and specifies the requirements for the actuators and sensors. Moreover, the mathematical model is derived. The following chapter describes the implementation of the prototype and the selected components. Chapter 5 shows the identification of the implemented system and the design of the controllers. This is followed by an evaluation of the performance of the position control, gravity compensation and vibration suppression. The thesis is concluded with a discussion of the results and an outlook on possible further research.

Chapter 2

State of the Art

This chapter reviews the state of the art in vibration isolation. First, passive systems and their main characteristics are discussed. Subsequently, active control strategies for vibration suppression and the required actuators and sensors are presented. Also, methods for zero-power gravity compensation are introduced. The chapter concludes with the research questions of this thesis.

2.1 Passive Vibration Isolation

The purpose of a vibration isolation system is to reduce the impact of mechanical disturbances on sensitive equipment [2]. Unwanted vibrations can be caused by human activity, car or rail traffic and heavy machinery, for example, and are transmitted from the floor via the support structure [1]. Direct disturbances may result from acoustic waves or originate from the payload itself, when it has dynamically moving components [2], [11].

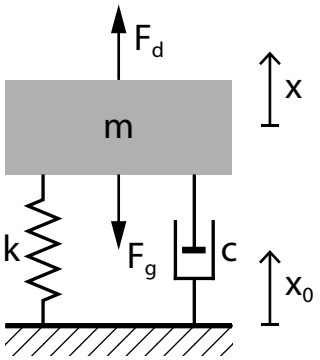

Figure 2.1: Model of a passive 1-DoF vibration isolation system.

In passive systems, vibration isolation is achieved with springs and dampers, with the former providing a softer suspension and the latter dissipating the vibration energy [12]. Figure 2.1 shows the model of a simple vibration isolation system with one DoF. The payload, represented by the rigid body with mass m, is exposed to a direct disturbance force F_d and vibrations of the ground x_0. The latter are transmitted by the support structure, which consists of a linear spring with stiffness k and a linear viscous damper with constant c [13]. The equation of motion of this system is given by

$$m\,\ddot{x} = F_d - c\,(\dot{x} - \dot{x}_0) - k\,(x - x_0). \tag{2.1}$$

Applying the Laplace transformation yields the relation in the frequency domain

$$\mathcal{L}\{x\} = \underbrace{\frac{1}{ms^2 + cs + k}}_{\text{Compliance } \mathcal{C}(s)} \mathcal{L}\{F_d\} + \underbrace{\frac{cs + k}{ms^2 + cs + k}}_{\text{Transmissibility } \mathcal{T}(s)} \mathcal{L}\{x_0\}\,. \tag{2.2}$$

The compliance $\mathcal{C}(s)$ indicates the displacement with which the payload reacts to the directly acting disturbance force F_d, while the transmissibility $\mathcal{T}(s)$ describes the extent to which ground vibrations are transmitted to the sensitive equipment. With the undamped resonance frequency $\omega_r = \sqrt{\frac{k}{m}}$ and the damping ratio $\zeta = \frac{c}{2\,m\,\omega_r}$, the transfer functions can also be expressed as follows [13]

$$\mathcal{C}(s) = \left.\frac{\mathcal{L}\{x\}}{\mathcal{L}\{F_d\}}\right|_{x_0 = 0} = \frac{1}{ms^2 + cs + k} = \frac{\frac{1}{m\,\omega_r^2}}{1 + 2\zeta\frac{s}{\omega_r} + \left(\frac{s}{\omega_r}\right)^2}, \tag{2.3}$$

$$\mathcal{T}(s) = \left.\frac{\mathcal{L}\{x\}}{\mathcal{L}\{x_0\}}\right|_{F_d = 0} = \frac{cs + k}{ms^2 + cs + k} = \frac{1 + 2\zeta\frac{s}{\omega_r}}{1 + 2\zeta\frac{s}{\omega_r} + \left(\frac{s}{\omega_r}\right)^2}. \tag{2.4}$$

The Bode plot of the transmissibility in Figure 2.2 shows that up to the resonance frequency ω_r floor vibrations are transmitted without attenuation or are even amplified. The suppression starts only at $\sqrt{2}\,\omega_r$, with an initial decrease in amplitude of $-40\,\text{dB/decade}$. However, due to the damping, this reduces to $-20\,\text{dB/decade}$ at higher frequencies.

Assuming that the mass m is given, the behaviour of the passive vibration isolation system can be adjusted via the stiffness and damping. The left Bode plot in Figure 2.2 shows that when the stiffness k is reduced (dashed lines), the resonance peak occurs at a lower frequency, which is beneficial for the suppression of seismic vibrations. However, the amplitude response of the compliance is shifted upwards, resulting in a higher sensitivity to direct disturbances [11], [13].

The effect of increasing the damping c can be observed in the right Bode plot (dashed lines). On the one hand, the resonance peak disappears, but on the other hand, the stronger dynamic coupling leads to an increased transmissibility of floor vibrations at higher frequencies. This illustrates two major trade-offs in the design of passive vibration isolation systems [13].

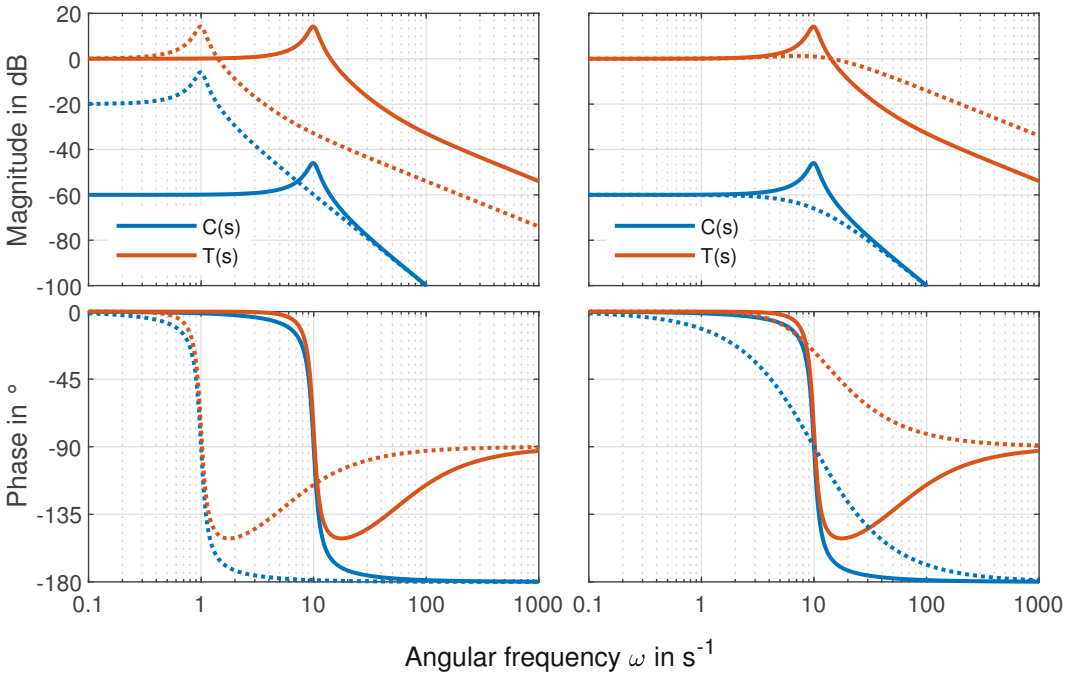

Figure 2.2: Bode plots of the compliance $\mathcal{C}(s)$ and transmissibility $\mathcal{T}(s)$ for $m = 10\,\mathrm{kg}$, $k = 10\,\mathrm{N/m}$, $\xi = 0.1$ (left and right, solid), reduced stiffness $k = 1\,\mathrm{N/m}$ (left, dotted), and increased damping ratio $\xi = 1$ (right, dotted).

Another limitation results from the static deflection Δx of the support structure due to the gravitational force $F_g = m\,g$

$$\Delta x = \frac{F_g}{k} = \frac{m\,g}{k} = \frac{g}{\omega_r^2}. \tag{2.5}$$

At a resonance frequency of 0.5 Hz, for example, the static deflection of a linear spring would be almost one metre. As this would result in design difficulties and problems with long-term stability, non-linear mounts with a high static and low dynamic stiffness are used [12], [13]. Very common are pneumatic springs, in which a gas, usually air, is pressurised to support the static load. The dynamic stiffness depends on the compressibility of the gas and the dimensions of the mount [12], [14]. Another approach uses a combination of a spring with positive stiffness, which carries the load, and an unstable mechanism with negative stiffness, which reduces the overall dynamic stiffness [15].

Commercial passive vibration isolation systems for table-top operation have a resonance frequency of around 8 Hz, and thus only provide isolation above 10 Hz. To achieve a slope of −40 dB/decade for the transmissibility, the damping ratio is very low. This, however, results in a distinct resonance peak, at which floor vibrations are amplified [16], [17]. For comparison, optical tables with pneumatic mounts and a mass of 600 kg have a resonance frequency as low as 1.4 Hz and start suppressing vibrations above 2 Hz [18].

2.2 Control Approaches for Active Vibration Isolation

As demonstrated in the previous section, passive vibration isolation systems require a trade-off between the suppression of direct and indirect disturbances [13]. This can be remedied by active control, which additionally requires sensors and actuators, but in return enables the implementation of a vibration isolation that is not possible with purely passive elements. The key characteristic of the two control strategies introduced below is the use of inertial sensors, which enable the measurement of the payload's motion with respect to an inertial (vibration-free) reference [19].

2.2.1 Feedback

To implement feedback control, the passive vibration isolation system presented earlier is extended by an inertial sensor placed on the payload and an actuator, as shown in Figure 2.3a. The controller uses the absolute measurement of the inertial sensor to set the actuator force according to the following control law [19]

$$F = -g_a\ddot{x} - g_v\dot{x} - g_p x. \tag{2.6}$$

This results in the compliance and transmissibility functions below

$$\mathcal{C}_{fb}(s) = \frac{1}{(m+g_a)s^2 + (c+g_v)s + (k+g_p)}, \tag{2.7}$$

$$\mathcal{T}_{fb}(s) = \frac{cs+k}{(m+g_a)s^2 + (c+g_v)s + (k+g_p)}. \tag{2.8}$$

from which it can be seen that feeding back acceleration, velocity and displacement changes the effective mass, damping and stiffness, respectively. The acceleration feedback gain g_a creates a virtual mass that is added to the payload mass m and thus shifts the mass line downwards, resulting in a better suppression of seismic vibrations [20]. The velocity and position feedback g_v and g_p create a virtual spring and damper, which, however, only appear in the denominator of the transfer functions. The reason for this is that the feedback is based on the measurement with respect to an inertial reference. Accordingly, the additional spring and damper in the equivalent mechanical model shown in Figure 2.3b

are not connected to the vibrating surface, but to a disturbance-free inertial reference [11], [19]. This is also referred to as *skyhook*, since one could think of the spring and damper being attached to the sky[1] [22].

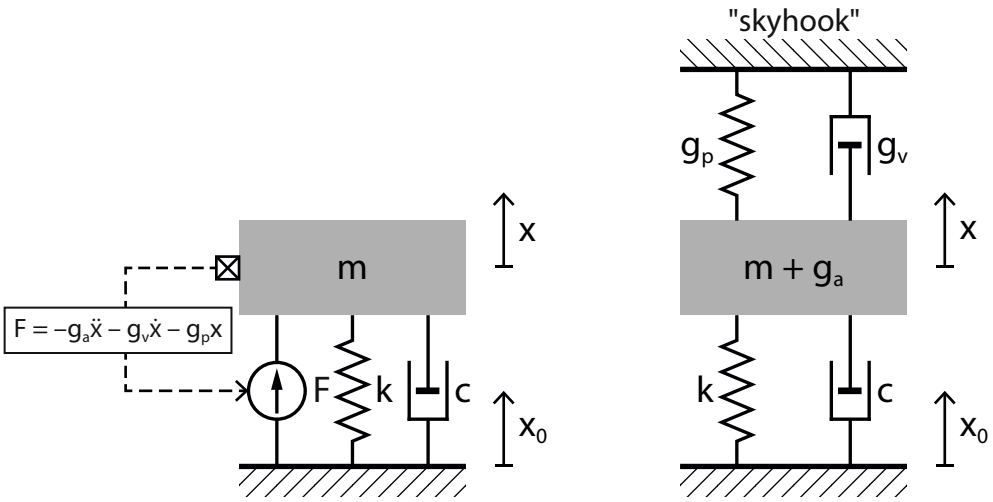

(a) Extended model with actuator, controller and sensor located on the payload.

(b) Equivalent mechanical model.

Figure 2.3: Model of an active 1-DoF vibration isolation system with feedback control.

Adding a so-called *skyhook damper* to the vibration isolation allows keeping the damping of the mechanical support structure low while still attenuating the resonance peak [22]. The additional stiffness improves the isolation from ground vibrations at low frequencies and reduces the sensitivity to direct disturbances [19], [20]. In a practical application, an accelerometer can be sufficient, as the velocity and displacement can be determined by integrating the acceleration. However, to prevent the signal from drifting, a high-pass filter must be added [20], [23]. Besides, the feedback with high gain can cause an undesired amplification of sensor noise [24].

In [25] and [26] active vibration isolation platforms with six DoFs were implemented. Both apply skyhook damping, generated by velocity feedback, to dampen the resonance of the suspension. The Stewart platform, presented in [25], suppresses vibrations in the range of 5 to 400 Hz. In [26], magnetic levitation with a low stiffness is used, resulting in a resonance frequency of 1.8 Hz in the vertical direction.

[1] In fact, the inertial reference is not located in the sky, but in the inertial sensor. However, due to the unavoidable connection between the seismic mass and the sensor frame, the measurement is only valid within a certain frequency range and sufficiently small amplitudes [19], [21].

2.2.2 Feedforward

In the second control approach, the seismic disturbances are measured directly by mounting the inertial sensor at the base of the vibration isolation system, as shown in Figure 2.4a. Since there is no feedback from the payload, this method is referred to as feedforward control [11]. Using the control law

$$F = -c\,\dot{x}_0 - k\,x_0, \tag{2.9}$$

yields the following compliance and transmissibility functions

$$\mathcal{C}_{ff}(s) = \frac{1}{ms^2 + cs + k}, \tag{2.10}$$

$$\mathcal{T}_{ff}(s) = 0. \tag{2.11}$$

Since the transmissibility $\mathcal{T}_{ff}(s)$ is zero, the controller obviously removes the connection between the payload and the vibration ground, as can also be seen from the equivalent mechanical model in Figure 2.4b. In contrast to feedback control, no additional stiffness or damping is generated here, but the existing spring and damper are *reconnected* to the skyhook. Ideally, the system is thus completely isolated from seismic disturbances. However, this is only possible if the transmissibility of the support structure is exactly known [11], [20]. For a real system, the simple model of a linear spring and damper assumed here is usually not sufficient. Moreover, the transmissibility can only be identified with limited accuracy, as sufficient excitation of the system is often difficult to achieve [27]. Therefore, also a combination of feedforward and feedback control is used in practical applications [24].

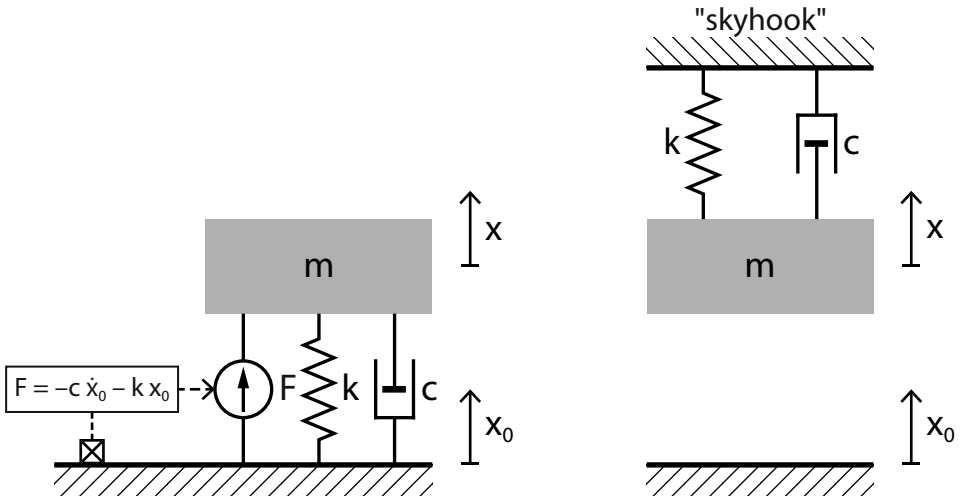

(a) Extended system with actuator, controller and sensor located on the ground.

(b) Equivalent mechanical model.

Figure 2.4: Model of an active 1-DoF vibration isolation system with feedforward control.

The measurement of the transmissibility and implementation of feedforward control is demonstrated for example in [11]. The vibration isolation system consists of a payload with a weight of 289 kg, which is suspended by four pneumatic mounts. The compensation forces are applied by Lorentz actuators. Using feedforward control, the transmissibility of floor vibrations was reduced by up to 30 Hz within a frequency range of 0.2 to 300 Hz.

2.3 Actuators

Actuators can be used to actively counteract unwanted disturbances. In vibration isolation systems, Lorentz and piezoelectric actuators are commonly applied for this purpose [28] and are explained in more detail below.

2.3.1 Lorentz Actuator

Due to their linearity and quasi-zero stiffness, Lorentz actuators are an indispensable component of high-precision positioning and vibration isolation systems [21], [28]. Their name and actuation principle are based on the Lorentz force, which is given by the following expression for a conductor carrying the current I in a magnetic field with flux density $\vec{B}$

$$\vec{F} = I \int_{\mathscr{C}} \mathrm{d}\vec{s} \times \vec{B}, \tag{2.12}$$

where the path of the conductor is determined by the curve $\mathscr{C}$ with the segments $\mathrm{d}\vec{s}$ orientated in the direction of the current. The equation shows the important linear relationship between force and current.

A widespread implementation of this actuation principle is the rotationally symmetrical design shown in Figure 2.5, which is also referred to as *voice coil actuator* [21], [29]. The magnetic circuit, consisting of the yoke with a permanent magnet, is usually the stationary part due to its greater weight, while the current-carrying coil is movable. The maximum motor constant is achieved, when the coil windings are orthogonal to the direction of the magnetic flux, as is the case with the voice coil actuator in Figure 2.5. An important property is the absence of a mechanical connection between the moving and the stationary part of the actuator, resulting in a contact- and frictionless force transmission. Furthermore, as can be seen from Equation 2.12, the force does not depend on the position of the mover, which is why there is theoretically no stiffness. In reality, however, a certain stiffness may result from the inhomogeneity of the magnetic field and the supply wires of the coil [21].

In order to avoid the support structure, which transmits floor vibrations, this actuator can be used to levitate the payload. The positioning can be achieved with quasi-zero stiffness at an arbitrary operating point within the actuation range [30], [31]. However, the force required to lift the weight of the payload results in a static power consumption and heat

dissipation, which may negatively impact sensitive measuring instruments and limit the positing accuracy [10], [32]. Moreover, the static current reduces the range available for dynamic actuation.

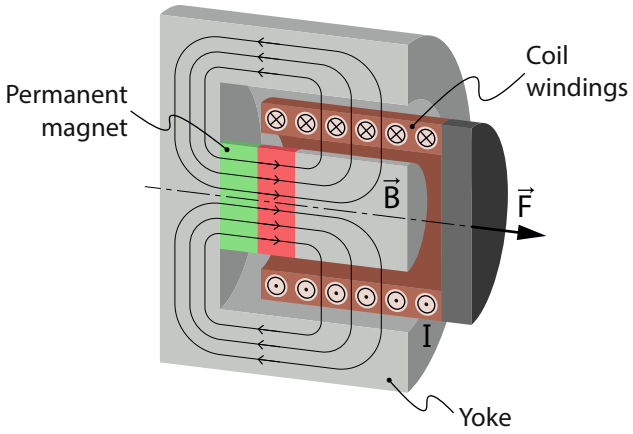

Figure 2.5: Cross-section of a voice coil actuator [21].

2.3.2 Piezoelectric Actuator

Compared to the previously presented Lorentz actuators, piezoelectric transducers have a very high stiffness and a relatively limited actuating range. Their operation is based on the inverse piezoelectric effect exhibited by some natural materials, such as quartz. These react to an external electric field with an expansion or contraction depending on the direction of the field. For practical applications, synthetic materials such as lead zirconate titanate (PZT), which has a higher electromechanical coupling, are commonly used [21], [33]. When used in positioning systems, usually multiple piezoelectric elements are stacked as shown in Figure 2.6 to increase the stroke. Moreover, the stack has to be mechanically prestressed, because it can only produce a pushing force due to its low tensile strength [33].

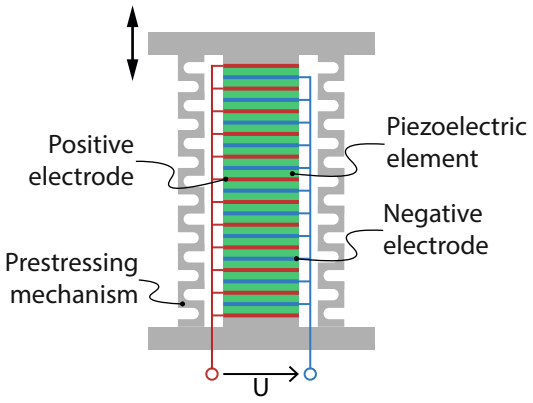

Figure 2.6: Piezoelectric stack actuator [34].

The main advantages of piezoelectric actuators are the high achievable force, bandwidth and positioning accuracy, as well as the ease of miniaturisation. For these reasons, they are also used for active vibration isolation, but can only suppress disturbances within the control bandwidth [28], [35] However, since the actuators are usually operated below the mechanical resonance, there is a gap between the frequency ranges of active and passive suppression (due to the inertia of the mass), in which vibrations are amplified [28].

2.4 Sensors

The performance of positioning and vibration isolation systems is not only determined by the actuators, but also by the sensors used to measure the position and acceleration of the payload [21]. The following section provides a brief overview of common sensor types and measuring principles.

2.4.1 Inertial Sensors

As demonstrated in Section 2.2, inertial sensors are a key component of active vibration isolation systems, since they allow the measurement of position, velocity and acceleration with respect to an inertial reference within a certain frequency range. Their mechanical structure consists of a so-called *seismic mass* (also known as *proof mass*), which acts as the vibration-free reference and is suspended from the sensor frame. Assuming that the suspension can be modelled by a spring and damper, the 1-DoF system from Figure 2.1 can be reused as a mechanical model of the sensor. In order to determine the motion of the object to which the sensor frame is attached, the relative position $y = x - x_0$ of the mass with respect to the frame is measured [36]. The frequency behaviour can be described by the following transfer function

$$\frac{\mathcal{L}\{y\}}{\mathcal{L}\{x_0\}} = -\frac{ms^2}{ms^2 + cs + k}. \tag{2.13}$$

This shows that above the resonance frequency $\omega_r = \sqrt{\frac{k}{m}}$, where the mass is decoupled from the frame, the relative distance y is proportional to the absolute position x_0 of the frame [36], [37]. Using $\mathcal{L}\{\ddot{x}_0\} = s^2\mathcal{L}\{x_0\}$, the transfer function can also be expressed as follows

$$\frac{\mathcal{L}\{y\}}{\mathcal{L}\{\ddot{x}_0\}} = -\frac{m}{ms^2 + cs + k}. \tag{2.14}$$

In this case, measuring y below the resonance frequency yields the acceleration of the frame $\ddot{x}_0$ scaled by the ratio of the mass m and stiffness k [36]. These equations describe the properties of the sensors presented below.

Geophone

The voice coil actuator in Figure 2.5 can also serve as a velocity sensor and is then called a *geophone* [29]. In this case, either the coil or the permanent magnet acts as the seismic mass and is connected to the other by a spring and a damper. When there is a relative motion between the two parts, caused for example by floor vibrations, a voltage is induced in the coil. This voltage U is related to the relative velocity $\dot{y}$ by the motor velocity constant K_v. Together with Equation 2.13, this results in

$$\frac{\mathcal{L}\{\dot{y}\}}{\mathcal{L}\{\dot{x}_0\}} = \frac{K_v \mathcal{L}\{U\}}{\mathcal{L}\{\dot{x}_0\}} = -\frac{ms^2}{ms^2 + cs + k}. \tag{2.15}$$

Above the resonance frequency ω_r, the seismic mass decouples from the sensor frame, and thus the measured voltage is proportional to the absolute velocity of the frame. Usually, the resonance frequency lies in the range of 1 to 10 Hz and is limited, similarly to passive vibration isolation systems, by the static deflection of the spring due to gravity [21], [36]. On the upper end, the operating range is limited to a few hundred hertz by higher-order modes of the spring [36].

Piezoelectric accelerometer

Piezoelectric materials can not only be used as actuators, but also as sensors. An externally applied mechanical pressure leads to a separation of charges, which can be measured. To be used as an accelerometer, a seismic mass is attached to the piezoelectric transducer. Assuming that the electric charge Q on the electrodes of the transducer is proportional to its deformation, which equals the distance y between the mass and the frame, and using Equation 2.14, the frequency behaviour is given by

$$\frac{\mathcal{L}\{y\}}{\mathcal{L}\{\ddot{x}_0\}} = -\frac{m}{ms^2 + cs + k} \sim \frac{\mathcal{L}\{Q\}}{\mathcal{L}\{\ddot{x}_0\}}. \tag{2.16}$$

Therefore, the acceleration $\ddot{x}_0$ of the frame is proportional to the charge Q below the mechanical resonance frequency. Due to the high stiffness of the piezoelectric material, it allows the measurement of the acceleration up to frequencies in the range of multiple kilohertz [21], [36]. Moreover, piezoelectric sensors achieve a very low noise level and are therefore commonly used in vibration isolation and monitoring systems. However, in order to measure the electric charge, it has to be converted into a voltage by a charge amplifier, which limits the sensitivity at very low frequencies [21], [38].

MEMS accelerometer

Microelectromechanical systems (MEMS) are miniaturised actuators and sensors with dimensions in the micrometre range that are implemented on a semiconductor chip. They are characterised by excellent mechanical and electrical properties. Moreover, the integration of the necessary electronics on the same chip reduces sensitivity to electromagnetic disturbances [21], [39].

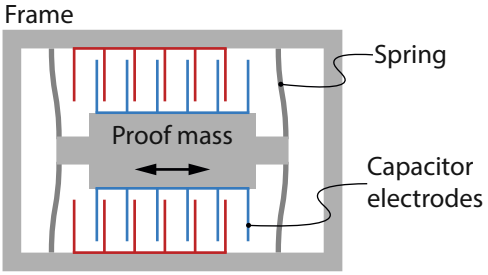

Figure 2.7: MEMS accelerometer with one DoF] [40].

Like the piezoelectric accelerometer, MEMS-based sensors also determine the acceleration from the displacement of a seismic mass. Typically, a comb structure as shown in Figure 2.7 is used for this purpose, in which the capacitance change between the fixed and movable electrode is measured. The measurement is limited by the mechanical resonance, which is usually in the kilohertz range [39], [40]. By arranging three such comb structures orthogonally, the linear acceleration can be measured in all spatial directions. In a gyroscope, a similar measurement principle is used to determine the angular rate of a rotation around an axis [39]. A sensor that combines three accelerometers and three gyroscopes is called an inertial measurement unit (IMU) and allows measuring the motion of an object in all six DoFs [41].

Force-balance accelerometer

Since the measurement principles presented so far are all passive, their bandwidth and dynamic range are mainly limited by the mechanical structure. They can be extended by a compensation-based measurement. In the case of the geophone, it is operated as a voice coil actuator and the acceleration is determined from the current required to keep the distance between the seismic mass and the sensor frame constant. The distance has to be measured by an additional displacement sensor [21], [29], [36]. In the same way, the electrostatic attraction force between the capacitor plates of a MEMS accelerometer can be used to counteract the acceleration of the seismic mass [39]. Due to the additional stiffness introduced by the feedback control loop, the bandwidth of the sensor is increased. In addition, larger amplitudes can be measured without saturation [29], [36].

2.4.2 Displacement Sensors

Important characteristics of a positioning system, such as bandwidth and precision, are largely determined by the sensors used. Below, three of the most frequently applied sensor principles in high-precision positioning systems are presented.

Capacitive sensor

Positioning systems with a small range and high precision usually use capacitive sensors, because they offer very good linearity, resolution in the nanometre range and a high bandwidth. The measurement principle is based on the dependence of the capacitance of two conductive surfaces on their geometric arrangement [42], [43]. Neglecting fringe effects, the capacitance C of the parallel plate capacitor shown Figure 2.8a is given by

$$C = \frac{\varepsilon A}{d}, \tag{2.17}$$

where A denotes the area of the capacitor plates, which are at a distance d from each other, and ε is the permittivity of the dielectric. As shown in Figure 2.8, there are three possible arrangements for determining the displacement Δx from the capacity C. In Figure 2.8b, one of the capacitor plates is shifted laterally, which changes the overlapping area A, in Figure 2.8c the dielectric is moved, and in Figure 2.8d the distance between the capacitor plates d is varied. Since the latter approach offers the greatest sensitivity, it is usually applied despite the smaller range and nonlinearity [42]. However, by means of differential measurement, the output voltage can be linearised [21].

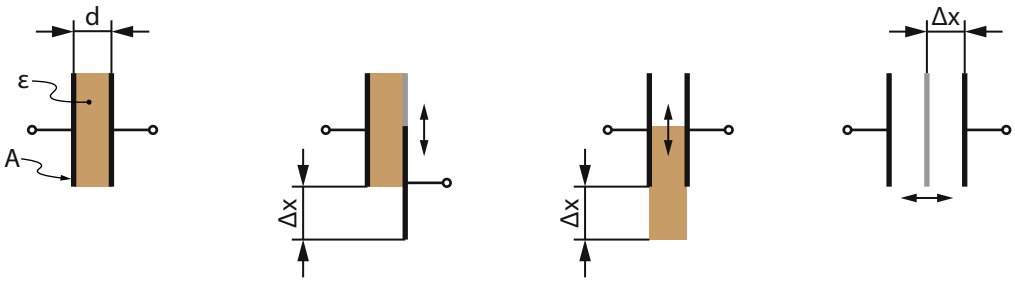

(a) Parallel plate capacitor. **(b)** Laterally moving plate. **(c)** Moving dielectric. **(d)** Axially moving plate.

Figure 2.8: Arrangements for the displacement measurement with a capacitive sensor [42].

Because it is impractical to place an electrode on the measurement object, the head of a capacitive sensor usually contains two electrodes and the conductive target acts as the third electrode. This results in two capacitances connected in series, each of which depends

on the distance to the target object [21]. Commercial products offer a resolution of 1 nm at a measuring range of 50 µm, but are also available for a range of up to 10 mm at a resolution of 200 nm [44].

Eddy-current sensor

The operation of eddy-current sensors is based on Faraday's law of induction. As shown in Figure 2.9, its main part is a coil, which is excited by an AC current, which generates a magnetic field. In the vicinity of a conductive target, the alternating magnetic field induces a voltage, which causes eddy currents counteracting the magnetic field. This leads to a change of the AC resistance on the primary side, from which the distance to the target can be determined [21], [42].

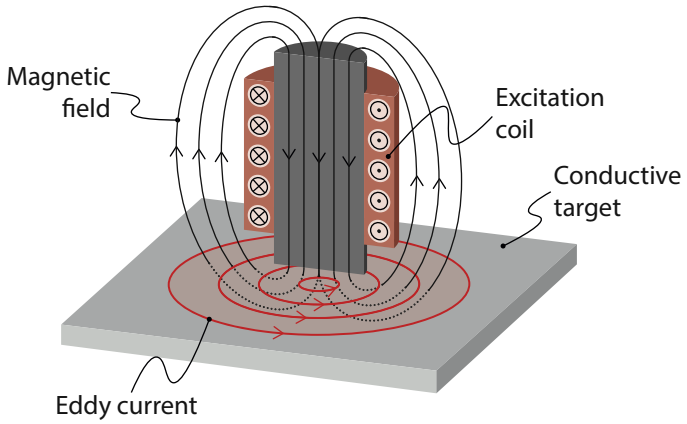

Figure 2.9: Cross-section of an eddy current displacement sensor [42].

The head of eddy-current sensors can be shielded or unshielded, with the former having a greater range but also being more sensitive to nearby magnetic fields and conductors. Compared to capacitive sensors, they are more sensitive to temperature and have a lower resolution. However, especially in industrial applications, they offer the advantage of being insensitive to dust, oil and similar contaminations of the air gap [42]. Commercially available sensors offer a measuring range of 0.4 to 80 mm and a resolution of 20 nm for smaller ranges [45].

Interferometer

When two coherent light beams are superimposed, constructive or destructive interference occurs, depending on their spatial phase shift. This effect is used in the Michelson interferometer shown in Figure 2.10 to determine the displacement of a target. The laser beam is split into two paths by a beam splitter, one of which leads to the static reference reflector

and the other to the moving target. After reflection, the two beams recombine again at the beam splitter and interfere [21], [42]. The intensity I measured by the detector is given by the following expression [46]

$$I(\Delta x) = I_0 \cos^2\left(\frac{2\pi}{\lambda}\Delta x\right), \tag{2.18}$$

where I_0 is the intensity of the incoming light beam, which has the wave length λ, and Δx is the displacement of the moving target. The intensity pattern has a periodicity of $\frac{\lambda}{2}$, enabling a resolution of the displacement measurement below the wavelength of the used laser light [21], [42].

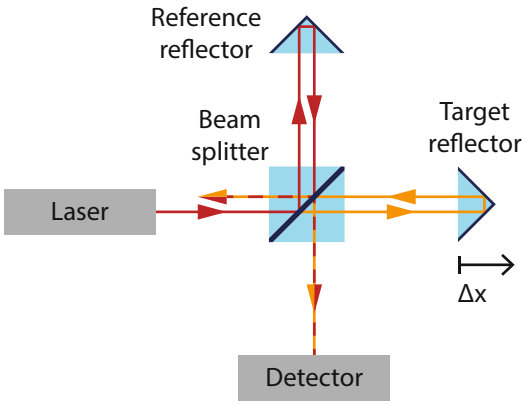

Figure 2.10: Optical paths in a Michelson interferometer [42].

Modern interferometers, however, are based on the heterodyne principle, in which two laser beams with different frequency and orthogonal polarisation are used. This reduces the sensitivity to differences in the reference and measurement path. In addition to the sub-wavelength resolution, interferometers also provide a very long range, which can be several metres. However, the disadvantages are the relatively high cost and the sensitivity to environmental influences [42], [43]. A representative model allows the measurement on a range of 5 m with a resolution of 1 pm at a bandwidth of 10 MHz [47].

2.5 Gravity Compensation

The transmission of floor vibrations to the sensitive equipment through the support structure can be reduced if it is suspended without any mechanical connection. Very often this is achieved by electromagnetic levitation using Lorentz actuators due to their low stiffness [48], [49]. However, for a heavy load, they become quite large and heavy themselves. Moreover, the heat dissipation due to the constant power consumption may negatively

impact the thermal stability of the equipment and limit the positioning accuracy [10]. To avoid these problems, powerless gravity compensation methods are required, of which two are presented below.

2.5.1 Permanent Magnets

A common approach for achieving zero-power gravity compensation is to use a suitable arrangement of permanent magnets, of which three simple possibilities are shown in Figure 2.11. Since, according to Earnshaw's theorem, stable passive magnetic levitation is not possible, the floating part has to be stabilised by additional actuators [49], [50].

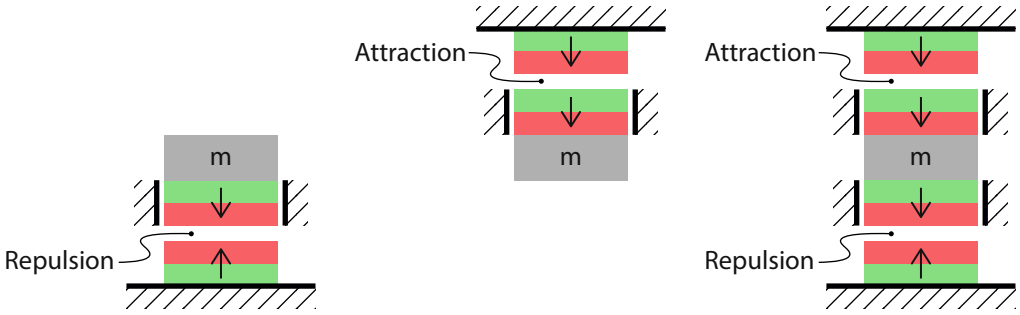

(a) Repulsive. **(b)** Attractive. **(c)** Repulsive and attractive.

Figure 2.11: Three permanent magnet arrangements for gravity compensation [48].

In Figure 2.11a, the repulsive forces of two opposing permanent magnets is used to levitate the payload m. In Figure 2.11b, the load is held by the attraction of two magnets that are magnetised in the same direction. The disadvantage of this option compared to the first one is that the load falls down if the stabilising actuators fail. Another drawback, common to both configurations, is that the weight of the load is only accurately compensated at a certain distance. If the weight or the operating point is changed, the arrangement of the magnets must be adjusted. In addition, there is a significant stiffness due to the strong dependence of the force on the distance [48], [51]. The last problem can be countered by the arrangement in Figure 2.11c, in which both attraction and repulsion are applied. At the position where the attractive and repulsive forces acting on the mover exactly cancel each other out, the stiffness vanishes [48], [49]. With this approach, a vibration isolation system with a resonance frequency of just under 2 Hz and a static lifting capacity of around 40 N was realised in [49].

2.5.2 Electropermanent Magnets

An alternative to the permanent magnet arrangements, which can provide zero-power gravity compensation for a variable mass and operating point, is the so-called electropermanent magnet (EPM) shown in Figure 2.12. Its magnetic circuit comprises two different

permanent magnets, one with a very high coercivity and one with a relatively low one. The latter is wrapped into a coil, which is used to adjust its magnetisation. Usually, NdFeB and AlNiCo magnets are combined, since they have a similar remanence flux density [52].

If the AlNiCo magnet is magnetised antiparallel to the NdFeB magnet, as depicted in Figure 2.12a, the magnetic flux closes within the stator (assuming that both magnets have the same remanence flux density and dimensions) and no reluctance force is exerted on the mover. By applying a strong current pulse to the magnetising coil, the magnetisation of the AlNiCo magnet can be adjusted, while the NdFeB magnet is unaffected due to its much higher coercivity. If the magnetisation of the AlNiCo magnet is reduced, or it is magnetised parallel to the NdFeB magnet, the flux closes over the air gaps and through the mover yoke. This creates the following attractive force F at each vertical yoke [53]

$$F = \frac{B^2 A}{2\mu}, \tag{2.19}$$

where B denotes the flux density in the air gap, A is the cross-section of a single vertical yoke, and $\mu \approx \mu_0 = 4\pi\,10^{-7}\,\mathrm{H/m}$ is the magnetic permeability of air. Since there are two air gaps, the total force is $2F$.

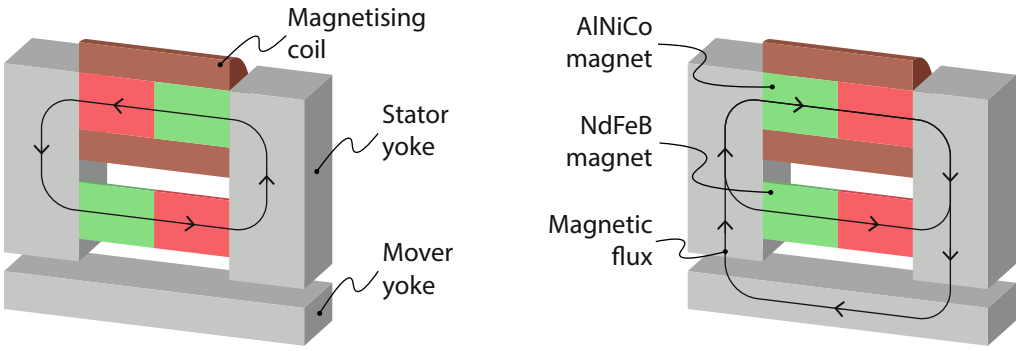

(a) Antiparallel magnetised magnets. **(b)** Parallel magnetised magnets.

Figure 2.12: Cross-section of (a) fully turned-off and (b) fully turned-on electropermanent magnet (EPM) [52].

This method allows the generated force to be adjusted to the mass of the payload and the desired operating point. However, due to the negative stiffness of the EPM, a flexure or another actuator is required for stabilisation. In [53] an EPM and a Lorentz actuator are integrated into one actuator, which can provide a static force between 0 and 25 N without significant energy consumption. When tuning the EPM, the hysteresis of the AlNiCo must be taken into account, which requires a non-linear control method [54].

2.6 Research Questions

At the beginning of this chapter, it was shown that there are inevitable trade-offs when designing a passive vibration isolation system. A particular drawback is that a better damping of floor vibrations always comes at the expense of a worse suppression of direct disturbances. There are also limitations in terms of damping and static deflection. Although the presented active control strategies require more effort in terms of actuators and sensors, they make it possible to overcome these restrictions. A further improvement in the suppression of floor vibrations is possible with electromagnetic levitation. However, due to the heat dissipation and high static power consumption, this is only practical in combination with gravity compensation.

In the introduction, the aim of this thesis was formulated as implementing a levitating platform with active vibration suppression. Before the active vibration isolation can be implemented, the following question must be answered first:

> *Is it feasible to design a levitating platform with six DoFs that can be positioned without static power consumption at an arbitrary operating point, independent of the payload?*

As mentioned in Section 2.5.1, magnetic levitation requires position control for stabilisation. However, position control and vibration isolation have conflicting goals, as the former tries to keep the distance between the platform and the base constant, while for the latter a weak connection between the two is required. Similarly, the relatively high negative stiffness also impairs the suppression of floor vibrations. The second research question of this thesis is therefore:

> *Can position control, magnetic levitation with zero-power gravity compensation and active vibration suppression be achieved at the same time?*

Chapter 3

Design and Modelling of the Vibration Isolation System

The first part of this chapter gives an overview of the mechanical structure of the vibration isolation system and the most important design aspects. Subsequently, the requirements for the actuators and sensors are explained in detail. In the second part, the dynamic model of the platform and the transformations of the actuator forces and sensor signals are derived.

3.1 Concept and Design Considerations

The mechanical construction of the vibration isolation system consists of a static base and a levitating platform. Since there is no mechanical connection between the two, the platform has to be stabilised in all of its six degrees of freedom, requiring at least the same number of actuators. For this purpose, Lorentz actuators are used due to their low stiffness and approximately linear characteristic. An important design aspect is the air gap between the mover and the stator of the actuators. On the one hand, a larger distance allows compensating disturbances with higher amplitudes and lowers the accuracy requirements for the components and the assembly. On the other hand, however, it reduces the motor constant of the actuators, which increases the power requirements and energy consumption.

To determine the position and orientation of the platform, at least six displacement sensors are required. These should measure without contact and have a measuring range that is at least as large as the travel range of the actuators. Vibrations are measured using compact and lightweight inertial sensors mounted on the platform and base, enabling both feedback and feedforward control, as discussed in Section 2.2.

Gravity compensation is achieved using EPMs, which allow the system to adapt to varying payloads while maintaining a constant operating point. As the load may not be placed exactly at the centre of the platform, at least three EPMs are required. Taking into account the limited capacity of the gravity compensation, the weight of the platform should be as low as possible in order to allow a higher payload. At the same time, however, the platform has to be rigid enough to prevent the occurrence of structural modes within the control bandwidth.

Minimum load capacity	3 kg
Minimum platform diameter	200 mm
Vibration isolation range	5 to 100 Hz
Positioning range (linear)	±0.5 mm
Positioning range (rotatory)	±0.3°

Table 3.1: Target specifications of the vibration isolation system.

To be suitable for table-top operation, the vibration isolation system must have a compact design, which can be achieved by a good integration of the components. The design must also ensure that they can be manufactured and assembled with reasonable effort. Moreover, there should be sufficient clearance for the assembly to be able to compensate for manufacturing tolerances. An overview of the target specifications of the vibration isolation system is provided in Table 3.1.

3.2 Actuation

In order to achieve a compact design, only the minimum number of six actuators is used, which are placed on the base as shown in Figure 3.1. The actuators for the in-plane and out-of-plane DoFs have different designs, but both are based on the Lorentz force due to its favourable properties. Three of the actuators (denoted by $V1$, $V2$, $V3$) operate in the vertical direction and are arranged on a circle with an offset of 120° between each other. They actuate the three out-of-plane DoFs (translation along the z-axis, and rotation around the x- and y-axis). Another three actuators are oriented in the circumferential direction (labelled as $H1$, $H2$, $H3$) and are responsible for the in-plane DoFs (translation along the x- and y-axis, and rotation around the z-axis). However, as they are placed under the platform with a vertical offset from the platform's centre of gravity, they also generate a torque around the x- and y-axis. Figure 3.2 shows which components belong to the mover and which to the stator.

A 3D model of the vertical actuator is shown in Figure 3.4. It is a slightly modified version of the actuator designed in [53]. The main difference is that in this case the Lorentz actuator has only two coils instead of four, because the movers of the three actuators are rigidly connected to each other via the platform, and therefore independent tilting is not possible anyway. What is unique about this design is the compact integration of a Lorentz actuator and an EPM, both generating forces in the vertical direction. The integration is achieved by using the vertical yoke parts for both magnetic circuits. Since the respective magnetic fluxes are perpendicular, they do not influence each other.

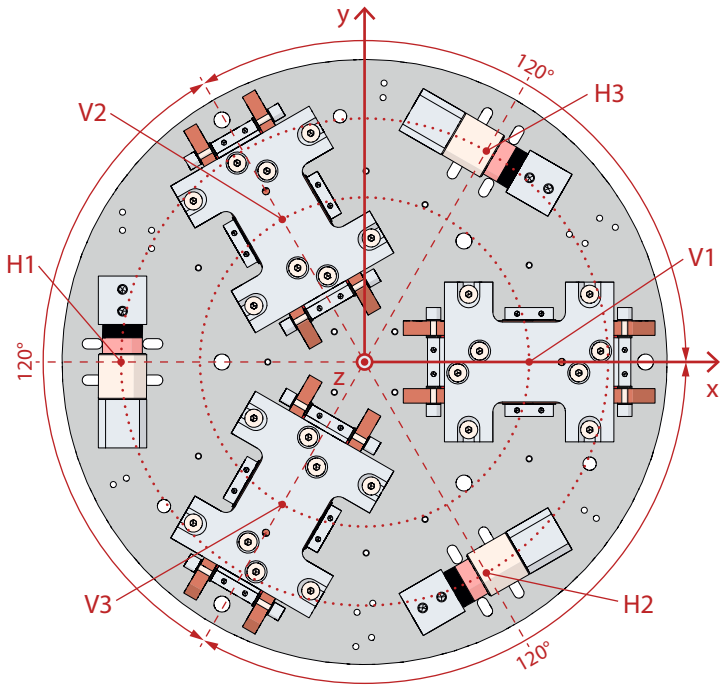

Figure 3.1: Location of the three Lorentz actuators with integrated EPMs ($V1$, $V2$, $V3$) and the three voice coils ($H1$, $H2$, $H3$).

As can be seen in Figure 3.4d, the magnetic flux for the Lorentz actuator is created by two Halbach arrays consisting of NdFeB cube magnets. They are arranged in such a way that they generate a circular magnetic field across the yoke between them. In the two air gaps are the coils, which are connected to the moving platform via aluminium brackets. As both the magnetic flux and the current change direction in the lower half, there is a resulting force that is directed either upwards or downwards, depending on the sign of the current.

The magnetic circuit of the EPM is depicted in Figure 3.4e and comprises a NdFeB magnet and an AlNiCo magnet wrapped in a magnetising coil. When the EPM is turned off (the AlNiCo magnet is magnetised antiparallel to the NdFeB magnet), the magnetic flux closes only via the stator yoke parts and there is no flux present in the gap to the horizontal yoke.

In the other case, when the EPM is turned on (the AlNiCo magnet is magnetised parallel to the NdFeB magnet), the flux of both magnets closes via the air gap and the horizontal yoke, which is consequently pulled upwards by the reluctance force, and connected to the platform via aluminium brackets.

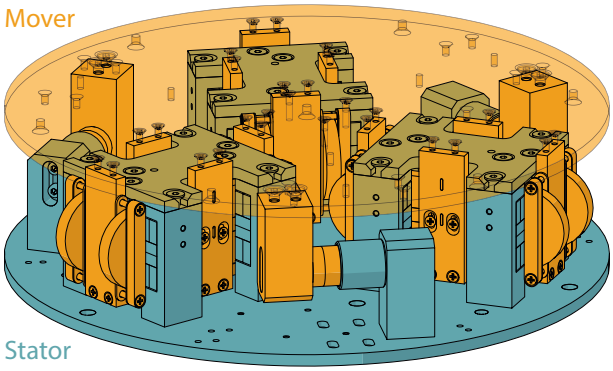

Figure 3.2: 3D model of the mover and stator.

The actuator was implemented and characterised in [53], according to which the maximum reluctance force the EPM can achieve for an air gap of 1 mm is 17 N. Therefore, three of them can carry a weight of almost 5.2 kg if the load is distributed equally. According to the CAD model, the total weight of the platform is about 1.9 kg, leaving 3.3 kg for an additional payload. If necessary, the load capacity can easily be increased by using a neodymium magnet with a larger diameter or higher grade. When the gravity compensation is disabled, the Lorentz actuators must carry the entire weight. For a load of 5.2 kg and a motor constant of 19.3 N/A as specified in [53], each actuator requires a current of approximately 0.9 A, which has to be supplied by the power amplifier.

Since the three EPMs can be tuned independently, the load does not necessarily have to be symmetrically distributed. However, as shown in Figure 3.3, the allowable ratio between the maximum load m and the weight m_{max} that a single EPM can lift decreases as the load's centre of gravity moves away from the centre of the platform. Moreover, the load's centre of gravity must not lie outside the triangle spanned by the three EPMs, because these can only generate an upward force.

Compared to the vertical actuators, the horizontal ones do not need to lift any weight and the disturbances mainly affect the platform in the vertical direction. Their main purpose is therefore to prevent the platform from drifting, which is why they can be significantly weaker and smaller than the vertical actuators. A simple and compact design that is used here are the voice coil actuators shown in the 3D model.

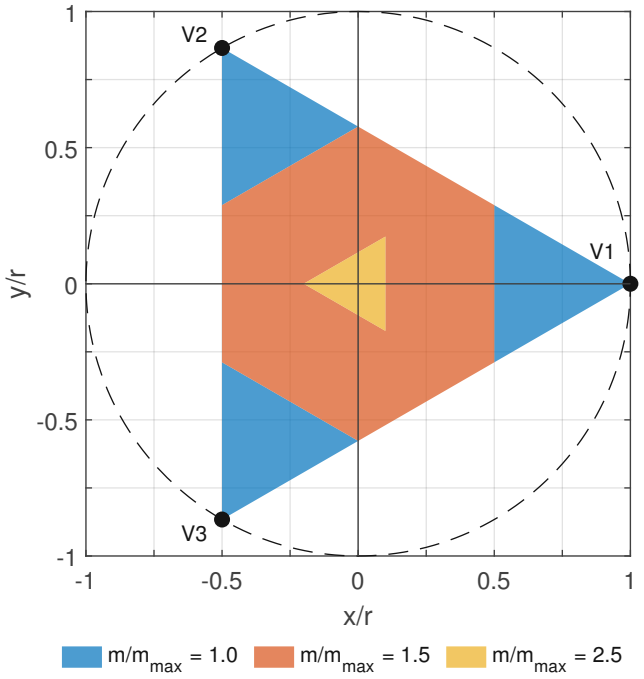

Figure 3.3: Maximum ratio of the total payload weight and load capacity of a single EPM m/m_{max} depending on the location of the centre of gravity. The coordinates x and y are relative to the radial distance of the actuators.

3.3 Sensors

The vibration isolation system integrates three types of sensors, which measure displacement, acceleration, and flux density. This section discusses the requirements for selection and implementation.

3.3.1 Displacement

The position and orientation of the levitating platform is measured by six non-contact displacement sensors, which is sufficient to capture all six DoFs. The measuring range should be at least the same as the travel range of the actuators, which is 1 mm. Although for vibration isolation a high bandwidth is not required, the sensors should be sufficiently fast to enable reliable identification of the system dynamics up to a few hundred hertz. If the platform is used for positioning, the bandwidth and precision are primarily determined by the bandwidth and resolution of the sensors. The noise level should be low, in order not to introduce additional disturbances. Moreover, low drift and good linearity are desirable.

To achieve collocation, the sensors are placed as close as possible to the application points of the actuator forces [21]. Figure 3.5 shows that the sensors measuring in the vertical direction are attached to the side of the actuators, because there is no space in the centre.

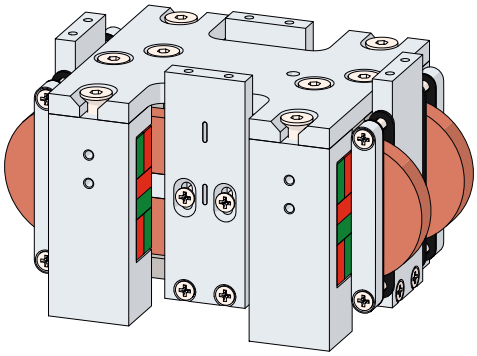

(a) Assembled actuator.

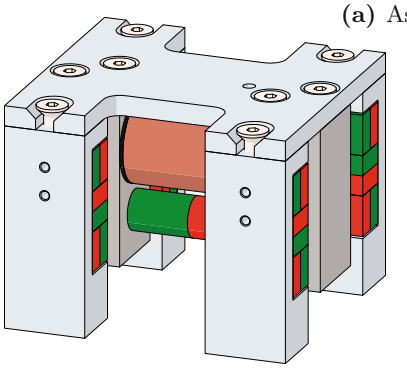

(b) Stator.

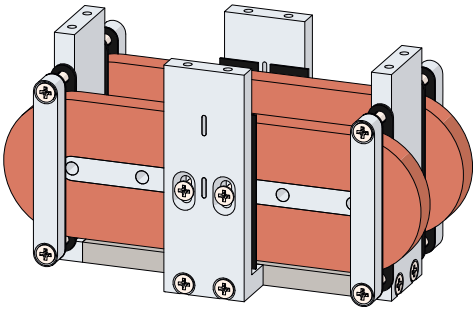

(c) Mover.

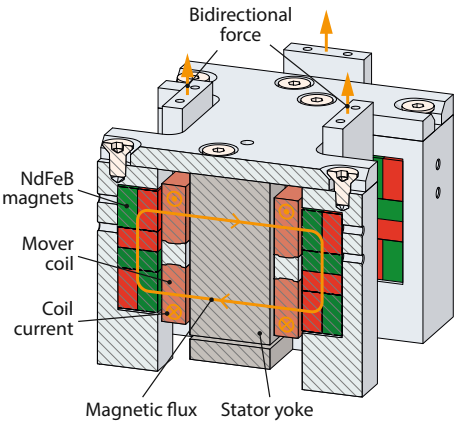

(d) Cross-section of the magnetic circuit of the Lorentz actuator.

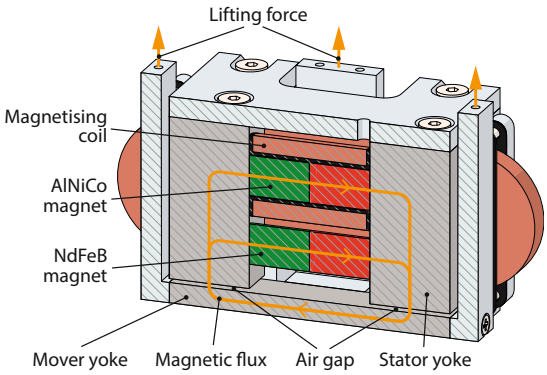

(e) Cross-section of the magnetic circuit of the EPM.

Figure 3.4: 3D model of the Lorentz actuator with integrated EPM [53].

The horizontal sensors are mounted slightly above the actuator axis due to the attachment of the actuator coil. In order to protect the sensor heads from damage, additional spacers are integrated.

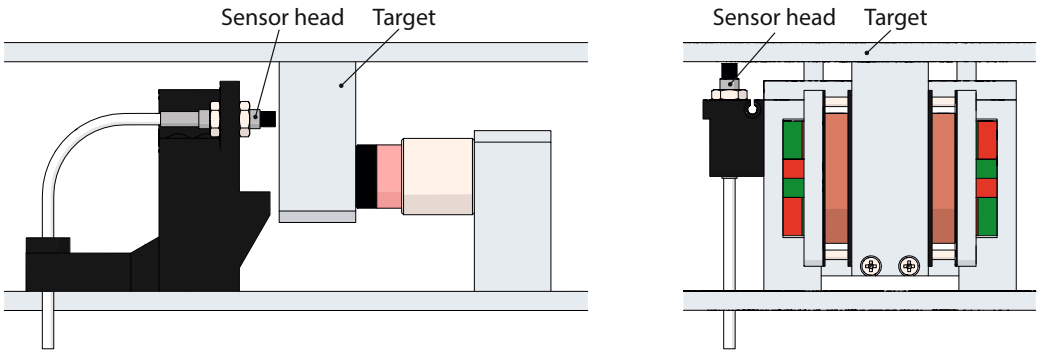

(a) Vertical. **(b)** Horizontal.

Figure 3.5: Mounting of the displacement sensors.

3.3.2 Acceleration and Angular Rate

Active vibration isolation requires the measurement of disturbances with respect to an inertial reference, which is possible with accelerometers and gyroscopes. As described in Section 2.2, the sensors are placed on the platform for feedback control and on the base for feedforward control. This vibration isolation system is designed to enable the implementation of both principles. Moreover, the sensor on the base is used to evaluate the performance of the vibration isolation.

In order to be able to suppress disturbances in all degrees of freedom, six sensors are required. The acceleration along the three linear axes is measured with accelerometers. The rotational motion in the other three degrees of freedom is measured using gyroscopes. The sensors should have a low noise density and high sensitivity within the targeted bandwidth of 5 to 100 Hz, since this determines the performance of the vibration isolation. Moreover, a compact size is required for a simple integration into the system. For the same reason, communication via a digital bus system is preferred, as at least twelve wires would be required to read all the sensor signals with analogue outputs.

3.3.3 Flux Density

The gravity compensation can be tuned more easily by measuring the flux density in the air gap of the EPMs, as it determines the reluctance force [54]. For this purpose, each EPM is equipped with a Hall sensor, which outputs a voltage that is proportional to the magnetic flux density. This voltage is generated when a current flowing through a

magnetic field is diverted due to the Lorentz force. The sensitivity of the sensor depends on the current, the geometry and the material. In order to achieve a constant sensitivity for the measurement, a stable current source is required [55].

Since the Hall sensors have to be placed in the air gap, they should be as thin as possible, because a larger air gap increases the reluctance of the magnetic circuit and reduces the maximum achievable force of the gravity compensation. The sensors also need mechanical protection against damage, which is achieved using spacers.

In addition, each EPM is provided with a search coil, which is wrapped around one of the static yoke parts. As this method is based on Faraday's law, only a time-varying magnetic field can be measured. Accordingly, the voltage U at the terminals of a coil with N turns and the cross-section A is calculated as follows

$$U = \frac{\mathrm{d}\Phi_v}{\mathrm{d}t} = NA\,\frac{\mathrm{d}B}{\mathrm{d}t}. \tag{3.1}$$

This assumes a homogeneous flux density B, which can be determined by integrating the voltage

$$B = \frac{1}{NA}\int U\,\mathrm{d}t. \tag{3.2}$$

Since an offset cannot be avoided and would lead to a drift of the signal, a high-pass filter is applied, resulting in the following transfer function

$$\frac{\mathcal{L}\{B\}(s)}{\mathcal{L}\{U\}(s)} = \frac{1}{sNA}\,\frac{s}{1+\frac{s}{\omega_c}} = \frac{1}{NA}\,\frac{1}{1+\frac{s}{\omega_c}}. \tag{3.3}$$

Effectively, the voltage signal only needs to be low-pass filtered to obtain the AC component of the flux density.

3.4 Mechanical Design

The mover of the vibration isolation system is designed as a circular disc on which the movers of the six actuators are mounted. As the weight of the platform must be supported by the gravity compensation, it should be as light as possible. In addition, when choosing the material and determining the dimensions, it must be ensured that structural modes, which are excited by the actuators and may complicate control, only occur sufficiently above the targeted control bandwidth of 100 Hz.

As aluminium allows weight savings of 40 to 50 % compared to steel while maintaining the same rigidity, the commonly used alloy *EN AW-6061* is chosen [56]. The dimensions of the disc are ⌀250 mm × 5 mm. With these properties, an eigenfrequency analysis of the mover was performed in SolidWorks, the results of which are shown in Figure 3.6.

According to this, the first eigenmode occurs at 268 Hz, which is well above the desired control bandwidth of 100 Hz. For the base, which carries the displacement sensors and the stators of the actuators, a disc with same dimensions and material is used.

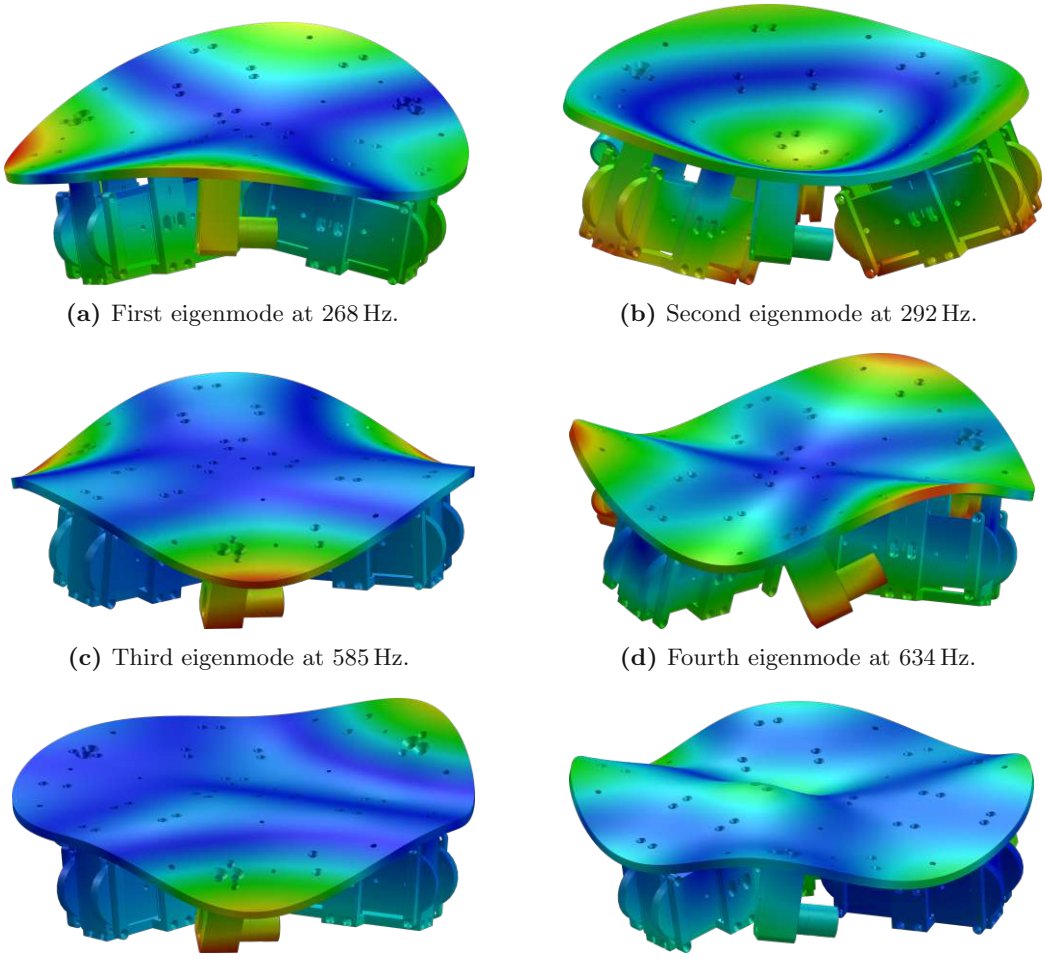

(a) First eigenmode at 268 Hz. **(b)** Second eigenmode at 292 Hz.

(c) Third eigenmode at 585 Hz. **(d)** Fourth eigenmode at 634 Hz.

(e) Fifth eigenmode at 714 Hz. **(f)** Sixth eigenmode at 1101 Hz.

Figure 3.6: Mode shapes of the first six eigenmodes of the levitating platform obtained by eigenfrequency analysis.

3.5 Model

Below, the mathematical model of the platform is derived. In the first part, the transfer function matrix is determined from the equation of motion. Subsequently, the transformations of the actuator forces and position sensor signals into the platform coordinate system are described.

3.5.1 Dynamic Model

In the model, the platform is treated as a rigid, free-floating body with six DoFs and a given mass and moment of inertia. Its position and orientation, measured in a coordinate system fixed to the base, is specified by the vector $\boldsymbol{x} \in \mathbb{R}^6$

$$\boldsymbol{x} = \begin{bmatrix} x & y & z & \alpha & \beta & \gamma \end{bmatrix}^{\mathrm{T}}, \tag{3.4}$$

where the angles α, β and γ denote the rotation around the axes x, y and z respectively (see Figure 3.7). The forces and torques acting on the platform in the corresponding axes are expressed by the vector $\boldsymbol{u} \in \mathbb{R}^6$

$$\boldsymbol{u} = \begin{bmatrix} F_x & F_y & F_z & M_\alpha & M_\beta & M_\gamma \end{bmatrix}^{\mathrm{T}}. \tag{3.5}$$

With the mass and inertia matrix $M \in \mathbb{R}^{6\times 6}$ the equation of motion can be formulated as follows

$$M \frac{\mathrm{d}^2 \boldsymbol{x}}{\mathrm{d}t^2} = \boldsymbol{u}. \tag{3.6}$$

As mentioned above, the stiffness and damping between the platform and the base are not taken into account in this model due to the magnetic levitation. Applying the Laplace transformation and rearranging the equation gives

$$\mathcal{L}\{\boldsymbol{x}\}(s) = \frac{1}{s^2} M^{-1} \mathcal{L}\{\boldsymbol{u}\}(s) = G(s)\, \mathcal{L}\{\boldsymbol{u}\}(s). \tag{3.7}$$

Since the coordinate axes are all perpendicular to each other, the matrix M is diagonal and contains only the platform mass m and the moments of inertia around the main axes J_x, J_y and J_z. With $M = \mathrm{diag}(m, m, m, J_x, J_y, Jz)$, the previous equation can also be written as follows

$$\underbrace{\mathcal{L}\begin{bmatrix} x \\ y \\ z \\ \alpha \\ \beta \\ \gamma \end{bmatrix}(s)}_{\mathcal{L}\{\boldsymbol{x}\}(s)} = \underbrace{\begin{bmatrix} \frac{1}{ms^2} & 0 & \dots & \dots & \dots & 0 \\ 0 & \frac{1}{ms^2} & \ddots & & & \vdots \\ \vdots & \ddots & \frac{1}{ms^2} & \ddots & & \vdots \\ \vdots & & \ddots & \frac{1}{J_x s^2} & \ddots & \vdots \\ \vdots & & & \ddots & \frac{1}{J_y s^2} & 0 \\ 0 & \dots & \dots & \dots & 0 & \frac{1}{J_z s^2} \end{bmatrix}}_{G(s)} \underbrace{\mathcal{L}\begin{bmatrix} F_x \\ F_y \\ F_z \\ M_\alpha \\ M_\beta \\ M_\gamma \end{bmatrix}(s)}_{\mathcal{L}\{\boldsymbol{u}\}(s)}. \tag{3.8}$$

This shows that the transfer function matrix $G(s) \in \mathbb{C}^{6\times6}$ has diagonal form and is therefore decoupled. As explained in more detail in Section 5.1.1, this allows the implementation of decentralised control.

3.5.2 Actuator Force Transformation

The transfer function matrix $G(s)$ is only decoupled if the forces and torques are applied in the orthogonal axes. However, as can be seen in Figure 3.7, the six actuators are not aligned with the coordinate axes and can only generate a torque in pairs. Therefore, a transformation $V \in \mathbb{R}^{6\times6}$ is required between the actuator forces $\boldsymbol{f} \in \mathbb{R}^6$ and the resulting forces and torques $\boldsymbol{u}$ (see Equation 3.5) acting on the platform

$$\boldsymbol{u} = V\boldsymbol{f}, \tag{3.9}$$

with

$$\boldsymbol{f} = \begin{bmatrix} F_{V1} & F_{V2} & F_{V3} & F_{H1} & F_{H2} & F_{H3} \end{bmatrix}^{\mathrm{T}}.$$

If the matrix V is invertible, the actuator forces $\boldsymbol{f}$ can be uniquely determined from the resulting forces and torques $\boldsymbol{u}$. As a result, an arbitrary translation and rotation can be generated, meaning that the system is fully actuated.

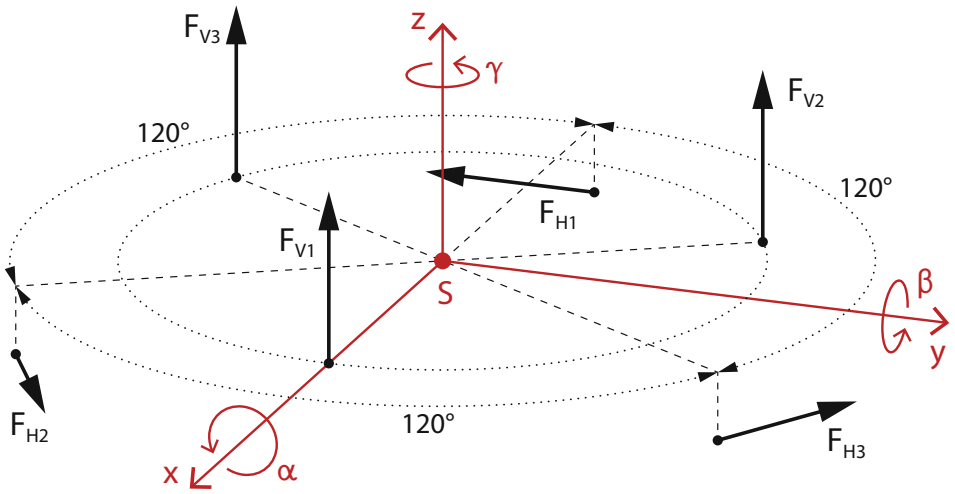

Figure 3.7: Schematic of the actuator location and orientation in the platform coordinate system.

To determine the matrix V, the direction of the actuator forces and the lever they have with respect to the platform's centre of gravity are required. Considering the arrangement of the actuators shown in Figure 3.7, this results in the expressions listed in Table 3.2. Due to the circular arrangement of the actuators, their position can be described by the radius, angle and vertical position. Since the platform's centre of gravity depends on the payload, the coordinates are referenced to an origin located on the base. This yields the

following expression for the matrix V

$$V = \begin{bmatrix} \boldsymbol{q}_{V1} & \cdots & \boldsymbol{q}_{H3} \\ (P_{V1} - P_s) \times \boldsymbol{q}_{V1} & \cdots & (P_{H3} - P_s) \times \boldsymbol{q}_{H3} \end{bmatrix}$$
$$= \begin{bmatrix} 0 & 0 & 0 & 0 & \frac{\sqrt{3}}{2} & -\frac{\sqrt{3}}{2} \\ 0 & 0 & 0 & -1 & \frac{1}{2} & \frac{1}{2} \\ 1 & 1 & 1 & 0 & 0 & 0 \\ 0 & \frac{\sqrt{3}}{2} r_V^A & -\frac{\sqrt{3}}{2} r_V^A & z_H^A - z_s & -\frac{1}{2}(z_H^A - z_s) & -\frac{1}{2}(z_H^A - z_s) \\ -r_V^A & \frac{1}{2} r_V^A & \frac{1}{2} r_V^A & 0 & \frac{\sqrt{3}}{2}(z_H^A - z_s) & -\frac{\sqrt{3}}{2}(z_H^A - z_s) \\ 0 & 0 & 0 & r_H^A & r_H^A & r_H^A \end{bmatrix}, \tag{3.10}$$

where $P_s = \begin{bmatrix} x_s & y_s & z_s \end{bmatrix}^{\mathrm{T}}$ denotes the position of the platform's centre of gravity with respect to the origin located on the base. For the transformation above, it is assumed that the load is placed in the centre of the platform, meaning that only the vertical position z_s changes while $x_s = y_s = 0$.

As shown in Section 2.3.1, the Lorentz actuators have a linear relationship between the current and the generated force, which can therefore be expressed as follows

$$\boldsymbol{f} = K_M \boldsymbol{i}, \tag{3.11}$$

where the diagonal matrix $K_M = \mathrm{diag}\,(K_{V1}, K_{V2}, K_{V3}, K_{H1}, K_{H2}, K_{H3})$ contains the motor constants of the actuators and $\boldsymbol{i} \in \mathbb{R}^6$ the respective currents. With the inverted matrices K_M^{-1} and V^{-1}, the currents can be calculated from the resulting forces and torques $\boldsymbol{u}$

$$\boldsymbol{i} = K_M^{-1} \boldsymbol{f} = K_M^{-1} V^{-1} \boldsymbol{u}. \tag{3.12}$$

This transformation is used in the position control loop to calculate the reference for the current controllers from the required forces and torques (see Section 5.1.1).

3.5.3 Position Signal Transformation

For the implementation of the position control, it is necessary to determine the position and orientation of the platform $\boldsymbol{x}$ from the signals of the displacement sensors. Since these are not aligned with the coordinate axes and cannot measure the rotation angles directly, another transformation is required. To derive this transformation, it is assumed that each sensor measures the displacement of a point P_i located on the target along their respective sensor axis $\boldsymbol{q}_i$, as shown in Figure 3.8. Consequently, for an arbitrary shift of P_i by the

Actuator i	P_i	$\boldsymbol{q}_i$
V1	$\begin{bmatrix} r_V^A & 0 & z_V^A \end{bmatrix}^{\mathrm{T}}$	$\begin{bmatrix} 0 & 0 & 1 \end{bmatrix}^{\mathrm{T}}$
V2	$\begin{bmatrix} -\frac{1}{2}r_V^A & \frac{\sqrt{3}}{2}r_V^A & z_V^A \end{bmatrix}^{\mathrm{T}}$	$\begin{bmatrix} 0 & 0 & 1 \end{bmatrix}^{\mathrm{T}}$
V3	$\begin{bmatrix} -\frac{1}{2}r_V^A & -\frac{\sqrt{3}}{2}r_V^A & z_V^A \end{bmatrix}^{\mathrm{T}}$	$\begin{bmatrix} 0 & 0 & 1 \end{bmatrix}^{\mathrm{T}}$
H1	$\begin{bmatrix} -r_H^A & 0 & z_H^A \end{bmatrix}^{\mathrm{T}}$	$\begin{bmatrix} 0 & -1 & 0 \end{bmatrix}^{\mathrm{T}}$
H2	$\begin{bmatrix} \frac{1}{2}r_H^A & -\frac{\sqrt{3}}{2}r_H^A & z_H^A \end{bmatrix}^{\mathrm{T}}$	$\begin{bmatrix} \frac{\sqrt{3}}{2} & \frac{1}{2} & 0 \end{bmatrix}^{\mathrm{T}}$
H3	$\begin{bmatrix} \frac{1}{2}r_H^A & \frac{\sqrt{3}}{2}r_H^A & z_H^A \end{bmatrix}^{\mathrm{T}}$	$\begin{bmatrix} -\frac{\sqrt{3}}{2} & \frac{1}{2} & 0 \end{bmatrix}^{\mathrm{T}}$

Table 3.2: Point of application P_i and direction $\boldsymbol{q}_i$ of the actuator forces.

vector $\boldsymbol{p}_i$, it can only determine the distance y_i, which is the normal projection of $\boldsymbol{p}_i$ onto $\boldsymbol{q}_i$. The index $i \in \{V1, V2, V3, H1, H2, H3\}$ indicates the actuator to which the respective displacement sensor is attached.

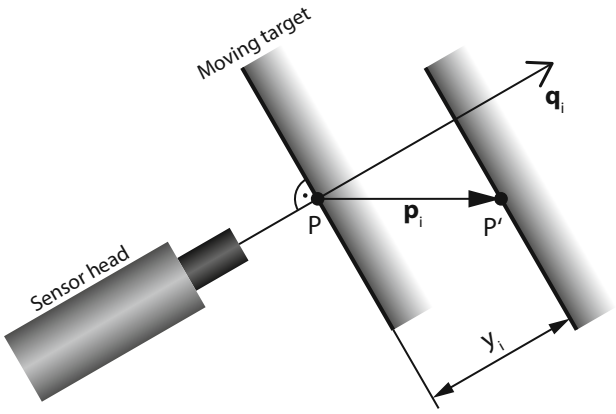

Figure 3.8: Geometric model of the displacement measurement.

If the platform is moved from its centre position $\boldsymbol{x}_0 \in \mathbb{R}^6$ according to the values in $\boldsymbol{x}$, the shift of the point P_i to P_i' can be described by the following affine transformation

$$P_i' = S(\boldsymbol{x})P_i\,, \tag{3.13}$$

where $P_i, P_i' \in \mathbb{R}^4$ are expressed in homogeneous coordinates and the transformation matrix $S(\boldsymbol{x}) \in \mathbb{R}^{4\times4}$ is given by

$$S(\boldsymbol{x}) = \begin{bmatrix} R(\alpha,\beta,\gamma) & T(x,y,z) \\ \mathbf{0} & 1 \end{bmatrix}. \tag{3.14}$$

It is composed of $T(x,y,z) \in \mathbb{R}^3$ and $R(\alpha,\beta,\gamma) \in \mathbb{R}^{3\times3}$, which describe the translation and rotation respectively

$$T(x,y,z) = \begin{bmatrix} x \\ y \\ z \end{bmatrix}, \tag{3.15}$$

$$R(\alpha,\beta,\gamma) = \underbrace{\begin{bmatrix} 1 & 0 & 0 \\ 0 & \cos\alpha & -\sin\alpha \\ 0 & \sin\alpha & \cos\alpha \end{bmatrix}}_{\text{x-axis}} \underbrace{\begin{bmatrix} \cos\beta & 0 & \sin\beta \\ 0 & 1 & 0 \\ -\sin\beta & 0 & \cos\beta \end{bmatrix}}_{\text{y-axis}} \underbrace{\begin{bmatrix} \cos\gamma & -\sin\gamma & 0 \\ \sin\gamma & \cos\gamma & 0 \\ 0 & 0 & 1 \end{bmatrix}}_{\text{z-axis}}. \tag{3.16}$$

Using this transformation matrix, the normal projection $y_i \in \mathbb{R}$ measured by a sensor due to the displacement $\boldsymbol{x}$ can be calculated as follows

$$y_i(\boldsymbol{x}) = \boldsymbol{q}_i^{\mathrm{T}} \boldsymbol{p}_i(\boldsymbol{x}) = \boldsymbol{q}_i^{\mathrm{T}} (P_i'(\boldsymbol{x}) - P_i) = \boldsymbol{q}_i^{\mathrm{T}} (S(\boldsymbol{x}) - E) P_i\,, \tag{3.17}$$

where $E \in \mathbb{R}^{4\times4}$ is the identity matrix. Clearly, this is only an approximation, which becomes less accurate the larger the displacement is. But since the platform is stabilised at a constant operating point during normal operation, it can be assumed that the deviations are small. If the measurement points of the sensors P_i are defined with respect to the origin located on the base, the location of the platform's centre of gravity $P_s = \begin{bmatrix} x_s & y_s & z_s \end{bmatrix}^{\mathrm{T}}$ has to be subtracted, which results in

$$y_i(\boldsymbol{x}) = \boldsymbol{q}_i^{\mathrm{T}} (S(\boldsymbol{x}) - E)(P_i - P_s). \tag{3.18}$$

Next, the six sensor signals are combined in the vector $\boldsymbol{y} \in \mathbb{R}^6$ and the equation is linearised at $\boldsymbol{x} = \boldsymbol{0}$

$$\boldsymbol{y}(\boldsymbol{x}) = \begin{bmatrix} y_{V1}(\boldsymbol{x}) & \dots & y_{H3}(\boldsymbol{x}) \end{bmatrix}^{\mathrm{T}} \approx \underbrace{\boldsymbol{y}(\boldsymbol{0})}_{=\boldsymbol{0}} + \left.\frac{\partial \boldsymbol{y}(\boldsymbol{x})}{\partial \boldsymbol{x}}\right|_{\boldsymbol{x}=\boldsymbol{0}} \boldsymbol{x} = W\boldsymbol{x}, \tag{3.19}$$

where

$$W = \left.\begin{bmatrix} \frac{\partial y_{V1}(\boldsymbol{x})}{\partial \boldsymbol{x}} \\ \vdots \\ \frac{\partial y_{H3}(\boldsymbol{x})}{\partial \boldsymbol{x}} \end{bmatrix}\right|_{\boldsymbol{x}=\boldsymbol{0}} \in \mathbb{R}^{6\times6}. \tag{3.20}$$

The measurement points P_i and the directions $\boldsymbol{q}_i$ of each sensor, which are required to determine the matrix W, are provided in Table 3.3. Due to the circular arrangement of the sensors, their position can be described by the radius, angle and vertical position. Assuming again that the load is placed in the centre of the platform ($x_s = y_s = 0$),

Equations 3.18 and 3.19 yield the following expression for the matrix W

$$W = \begin{bmatrix} 0 & 0 & 1 & r_V^S \sin\left(\varphi_V^S\right) & -r_V^S \cos\left(\varphi_V^S\right) & \cdots \\ 0 & 0 & 1 & r_V^S \cos\left(\varphi_V^S + \frac{\pi}{6}\right) & r_V^S \sin\left(\varphi_V^S + \frac{\pi}{6}\right) & \\ 0 & 0 & 1 & -r_V^S \sin\left(\varphi_V^S + \frac{\pi}{3}\right) & r_V^S \cos\left(\varphi_V^S + \frac{\pi}{3}\right) & \\ 0 & -1 & 0 & z_H^S - z_s & 0 & \\ \frac{\sqrt{3}}{2} & \frac{1}{2} & 0 & -\frac{1}{2}(z_H^S - z_s) & \frac{\sqrt{3}}{2}(z_H^S - z_s) & \\ -\frac{\sqrt{3}}{2} & \frac{1}{2} & 0 & -\frac{1}{2}(z_H^S - z_s) & -\frac{\sqrt{3}}{2}(z_H^S - z_s) & \end{bmatrix}$$

$$\begin{bmatrix} 0 \\ 0 \\ 0 \\ -r_H^S \cos\left(\varphi_H^S\right) \\ -\frac{r_H^S}{2}\left(\sqrt{3}\cos\left(\varphi_H^S + \frac{\pi}{6}\right) + \sin\left(\varphi_H^S + \frac{\pi}{6}\right)\right) \\ -\frac{r_H^S}{2}\left(\sqrt{3}\sin\left(\varphi_H^S + \frac{\pi}{3}\right) + \cos\left(\varphi_H^S + \frac{\pi}{3}\right)\right) \end{bmatrix} \quad \cdots \quad . \tag{3.21}$$

By inverting the matrix W, the displacement of the platform $\boldsymbol{x}$ from its centre position $\boldsymbol{x}_0$ can be determined from the sensor values $\boldsymbol{y}$

$$\boldsymbol{x} = W^{-1}\boldsymbol{y}. \tag{3.22}$$

This allows the position control loop to be closed.

Sensor i	P_i	$\boldsymbol{q}_i$
V1	$\begin{bmatrix} r_V^S \cos\varphi_V^S & r_V^S \sin\varphi_V^S & z_V^S \end{bmatrix}^{\mathrm{T}}$	$\begin{bmatrix} 0 & 0 & 1 \end{bmatrix}^{\mathrm{T}}$
V2	$\begin{bmatrix} -r_V^S \sin\left(\varphi_V^S + \frac{\pi}{6}\right) & r_V^S \cos\left(\varphi_V^S + \frac{\pi}{6}\right) & z_V^S \end{bmatrix}^{\mathrm{T}}$	$\begin{bmatrix} 0 & 0 & 1 \end{bmatrix}^{\mathrm{T}}$
V3	$\begin{bmatrix} -r_V^S \cos\left(\varphi_V^S + \frac{\pi}{3}\right) & -r_V^S \sin\left(\varphi_V^S + \frac{\pi}{3}\right) & z_V^S \end{bmatrix}^{\mathrm{T}}$	$\begin{bmatrix} 0 & 0 & 1 \end{bmatrix}^{\mathrm{T}}$
H1	$\begin{bmatrix} r_H^S \cos\varphi_H^S & r_H^S \sin\varphi_H^S & z_H^S \end{bmatrix}^{\mathrm{T}}$	$\begin{bmatrix} 0 & -1 & 0 \end{bmatrix}^{\mathrm{T}}$
H2	$\begin{bmatrix} -r_H^S \sin\left(\varphi_H^S + \frac{\pi}{6}\right) & r_H^S \cos\left(\varphi_H^S + \frac{\pi}{6}\right) & z_H^S \end{bmatrix}^{\mathrm{T}}$	$\begin{bmatrix} \frac{\sqrt{3}}{2} & \frac{1}{2} & 0 \end{bmatrix}^{\mathrm{T}}$
H3	$\begin{bmatrix} -r_H^S \cos\left(\varphi_H^S + \frac{\pi}{3}\right) & -r_H^S \sin\left(\varphi_H^S + \frac{\pi}{3}\right) & z_H^S \end{bmatrix}^{\mathrm{T}}$	$\begin{bmatrix} -\frac{\sqrt{3}}{2} & \frac{1}{2} & 0 \end{bmatrix}^{\mathrm{T}}$

Table 3.3: Measurement points P_i and directions $\boldsymbol{q}_i$ of the displacement sensors.

Chapter 4

Implementation of the Experimental Setup

This chapter provides details on the implementation of the prototype and starts with an overview of the experimental setup. Subsequently, the actuators, sensors and electronic components are explained in detail.

4.1 Overview

Figure 4.1 provides an overview of the entire experimental system. In the centre, the vibration isolation system is shown, of which only the platform is visible from this perspective (the inside can be seen in Figure 4.2). To the left is the current pulse generator for tuning the EPMs. On the right-hand side, are the analogue power amplifiers, with the heat sinks and transformer power supplies providing ±24 V. Slightly above this is the board for measuring the flux density in the EPMs. The components were arranged in a way that the distance for the cabling is minimised. Not visible in the picture are two further power supply units, which provide 5 V, ±15 V and 30 V, the electronics for the displacement sensors and the rapid-prototyping system used for data acquisition and control.

4.2 Actuation

The placement of the three vertical actuators, each consisting of a Lorentz actuator and an EPM, is shown in Figure 4.2. All parts are made of the aluminium alloy *EN AW-6061*, except for the yokes, which have to conduct the magnetic flux and are therefore made of steel *S235JR*. The total of 72 NdFeB cube magnets (grade N48, 10 mm), which are arranged in a Halbach array and generate the flux for the Lorentz actuator, were glued into the aluminium holders with a high-strength adhesive (see Figure 4.5). The holders

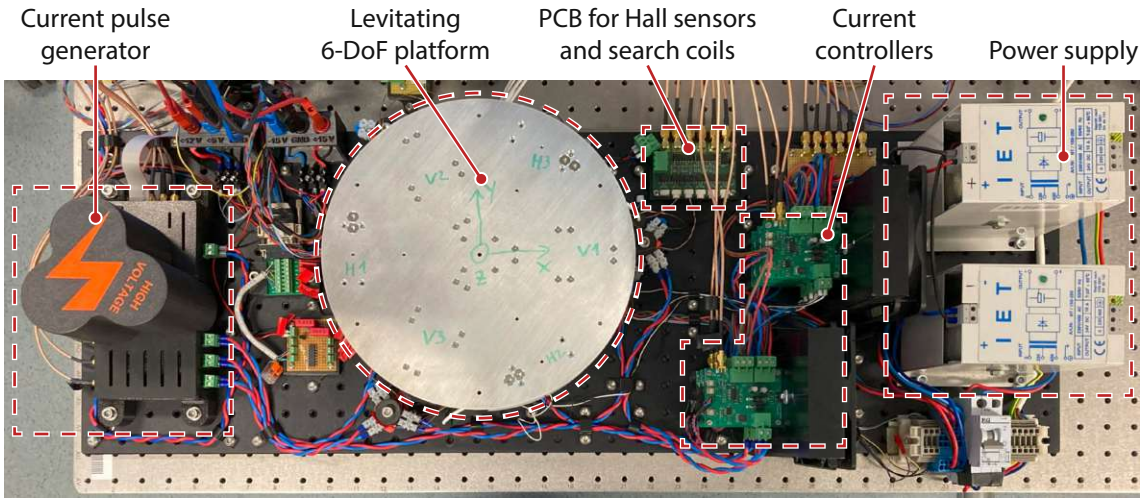

Figure 4.1: Overview of the setup showing the current pulse generator, vibration isolation system, PCB for the Hall sensors and search coils, and the current controllers with the power supply.

are mounted on the base and are connected by a cover plate. The air gap between the magnets and the mover coil is set to 1 mm and can be adjusted as required due to the elongated holes.

The mover of the vertical actuator is depicted in Figure 4.3 and comprises two copper coils, wound from a 0.4 mm thick copper wire, aluminium fastening elements and a steel yoke for the EPM. The coils have around 400 windings, and the whole mover weighs about 350 g. In contrast to [53], the windings of the coils were not glued with epoxy resin, but wound onto a screw-mountable core from a self-bonding enamelled copper wire. After winding, the coils were heated to around 200 °C, whereby the additional thermoplastic coating created a permanent bond between the windings. As the coils are therefore self-supporting, the distance to the magnets can be minimised.

The EPMs consist of AlNiCo (grade 500) and NdFeB magnets (grade 42) with the same dimensions ⌀10 mm × 30 mm, which are placed between the two vertical steel yokes. Each AlNiCo magnet is wrapped in a magnetising coil with 500 windings.

For the other three Lorentz actuators, voice coils *AVM20-10* with the specifications given in Table 4.1 were selected. These have an outer diameter of 20 mm and a length of 31 mm in the centre position. The mover and stator are mounted using aluminium holders as shown in Figure 4.5b.

Since the resistance and inductance values of the six actuator coils are required to tune the current controllers, these were measured with an LCR meter (E4980AL, Keysight Technologies, USA). Table 4.2 lists the median values for the frequency range from 20 to 100 Hz. The values for the machine-made voice coil actuators are almost identical, while there is a variation of over 20 % for the hand-made coils of the vertical actuators.

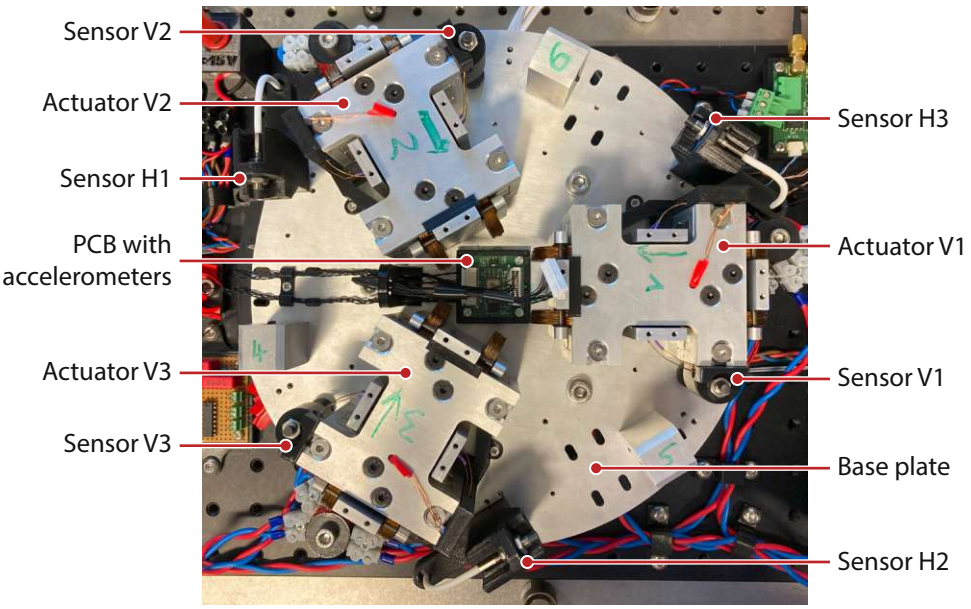

Figure 4.2: View inside the vibration isolation system showing the vertical actuators, displacement sensors and the PCB with the accelerometers.

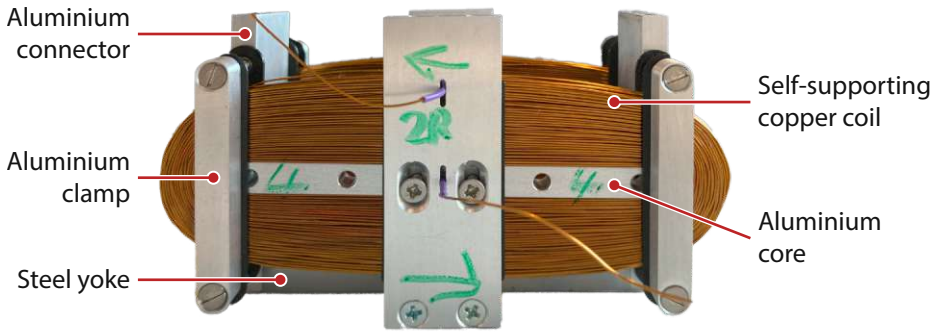

Figure 4.3: Mover of the vertical Lorentz actuator.

In addition, an estimate of the motor constant K_M is required for the first implementation of the position control, which can be derived using the following relationship

$$K_M = 8\,bNB, \tag{4.1}$$

where $b = 20\,\text{mm}$ is the width of a single Halbach array (in total there are eight air gaps), B denotes the flux density in the air gap, and N is the total number of windings (both coils). For the flux density, an average value of 430 mT was measured in the air gap between the magnets and the yoke using a gaussmeter (GM08, Hirst Magnetic Instruments, United Kingdom). This results in a motor constant of 27.5 N/A. Due to the higher number of windings, the value is larger than in [53].

Stroke	10 mm
Clearance of coil	0.5 mm
Motor constant	2 N/A
Continuous force	1.56 N
Coil assembly mass	11 g
Core assembly mass	45.1 g
Resistance	3.59 Ω
Inductance	0.5 mH

Table 4.1: Specifications of the voice coil actuator *AVM20-10* [57].

Actuator	Resistance Ω	Inductance mH
V1	20.9	22.8
V2	21.6	24.3
V3	23.6	28.0
H1	3.6	0.63
H2	3.6	0.62
H3	3.6	0.63

Table 4.2: Resistance and inductance values of the actuator coils.

4.2.1 Current Controller

For the Lorentz actuators, it is assumed that within the normal operating range the force is directly proportional to the current. Hence, the force can be regulated using a current controller, which adjusts the voltage across the coil to maintain the required current. The equivalent circuit of the actuator coil includes an inductance L and a resistor R connected in series, which results in the following transfer function from voltage U to current I

$$G(s) = \frac{I(s)}{U(s)} = \frac{1}{R + sL}\,. \tag{4.2}$$

This plant can be controlled by the following proportional-integral (PI) controller

$$C(s) = k\,\frac{R + sL}{s}\,. \tag{4.3}$$

With this choice, the dynamics of the plant are compensated and the open-loop transfer function $L(s)$ becomes an integrator

$$L(s) = C(s)G(s) = \frac{k}{s}\,. \tag{4.4}$$

Obviously, the parameter k corresponds directly to the desired crossover frequency.

The implemented current controller comprises an analogue PI control circuit that adjusts the output voltage of a power operational amplifier *OPA544* (Texas Instruments, USA) so that the desired current is maintained. To prevent the operational amplifier from overheating under a high current load, heat sinks with fans are provided. The controller parameters are set via resistors and capacitors, the values of which are determined according to the measured coil values and the desired bandwidth of 10 kHz. The current can be set via an analogue voltage input and is measured using a shunt resistor. The six current controllers are powered by two transformer power supply units, which provide ±24 V and up to 10 A.

4.2.2 Current Pulse Generator

In order to adjust the gravity compensation to the current payload, the magnetic flux of the EPMs must be modified accordingly, which in turn requires large current pulses in the magnetising coils. The necessary current is determined by the hysteresis of the AlNiCo magnet [54]. The most common method of magnetising permanent magnet materials is to use capacitor discharge magnetisers, as a higher voltage reduces energy consumption and heat dissipation [58].

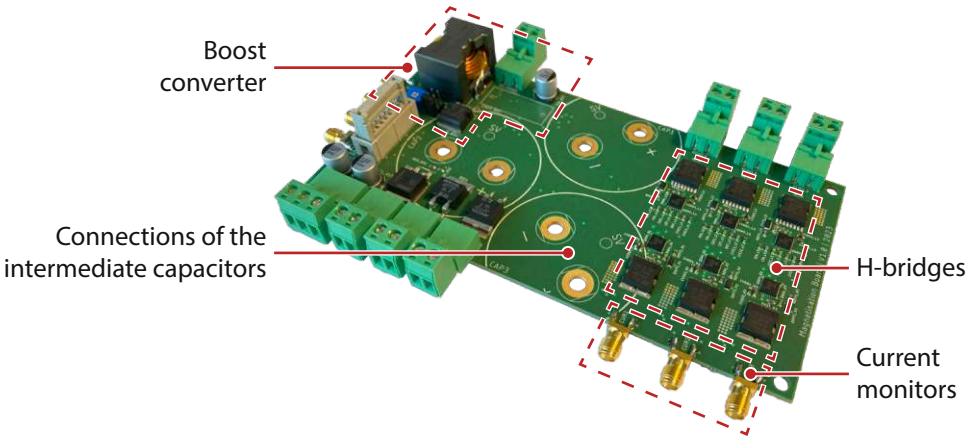

Figure 4.4: PCB of the current pulse generator (without intermediate capacitors).

For this thesis, a modified version of the magnetiser implemented in [53] is used. It consists of a boost converter, which can be supplied by a common DC power supply, and charges the intermediate capacitors (three electrolytic capacitors with 3.3 mF each) up to 350 V. The boost converter is switched by a hysteretic controller based on the set minimum and maximum boost current. A second hysteretic controller turns the boost converter off when the desired capacitor voltage is reached, and turns it on again when the voltage falls below the preset value by a certain threshold. The capacitors are followed by three full bridges, which allow the AlNiCo magnets in the EPMs to be magnetised in both directions. To monitor the magnetisation process, each of the three channels is equipped

with a Hall effect current sensor. All components are integrated on a single PCB (printed circuit board) as shown in Figure 4.4. The desired capacitor voltage is specified via an analogue input, otherwise the current pulse generator is controlled via digital signals. The measured values are provided via analogue outputs.

4.3 Sensors

This section presents the selected sensors for measuring displacement, acceleration and flux density. The required electronics and the rapid prototyping system, on which the control is implemented, are also briefly explained.

4.3.1 Displacement

The platform displacement is measured with six eddy-current sensors *eddyNCDT 3701-U1-A-C3* (Micro-Epsilon Messtechnik, Germany). They require an aluminium target with a size of at least three times the diameter of the sensor head (⌀4 mm). The mounting and the aluminium targets can be seen in Figure 4.5. Since the travel range of the platform is limited by the actuators to 0.5 mm, the measuring range of 1 mm is sufficient. The further specifications listed in Table 4.3 also fulfil the requirements. The measured value can be read out directly via the supplied electronics, which map the measuring range to an analogue voltage of 0 to 10 V.

Measuring range	1 mm
Resolution	1.3 nm
Bandwidth	10 kHz
Sensitivity	10 V/mm

Table 4.3: Specifications of the eddy-current displacement sensor *eddyNCDT 3701-U1-A-C3* [59].

4.3.2 Acceleration and Angular Rate

Due to their compact size, easy integration and good performance, MEMS sensors were chosen to measure the acceleration and angular rate. Figure 4.6 shows the circuit board with the sensors, of which one is attached to the platform and one to the base. On the top side is the 3-axis accelerometer *ADXL355* (Analog Devices, USA) and on the bottom side are the 2-axis gyroscope *ADXRS290* (Analog Devices, USA) and the IMU *LSM6DSRX* (STMicroelectronics, Switzerland). All three sensors are supplied with 3.3 V by a voltage regulator.

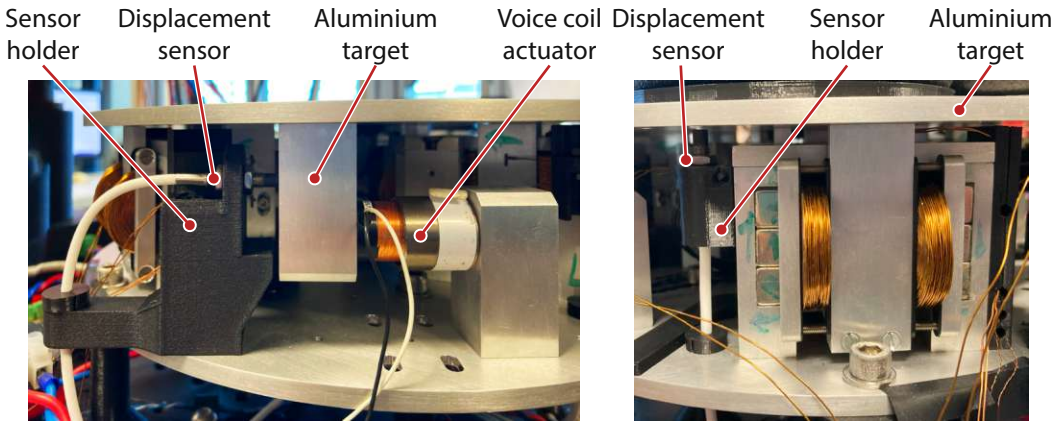

(a) Horizontal. **(b)** Vertical.

Figure 4.5: Mounting of the displacement sensors.

The specifications of the sensors are given in Table 4.4. They provide measurement data at a minimum frequency of 4 kHz and are read out via a common SPI bus, allowing an easy transfer of all 22 sensor values. To this end, the circuit board was designed so that two of them can be connected. In this case, the board on the base passes through the signals of the board on the moving platform. As the measurement is redundant for almost all axes, there is the possibility of sensor fusion, which may enable an increase in accuracy.

	ADXL355	**ADXRS290**	**LSM6DSRX**	
Type	3-axis accelerometer	2-axis gyroscope	IMU	
Axis	$\ddot{x}$, $\ddot{y}$, $\ddot{z}$	$\dot{\alpha}$, $\dot{\beta}$	$\ddot{x}$, $\ddot{y}$, $\ddot{z}$	$\dot{\alpha}$, $\dot{\beta}$, $\dot{\gamma}$
Noise density	$22.5\,\mu g/\sqrt{Hz}$	$4\,mdps/\sqrt{Hz}$	$60\,\mu g/\sqrt{Hz}$	$5\,mdps/\sqrt{Hz}$
Output data rate	4 kHz	4.25 kHz	6.67 kHz	
Sensitivity	3.9 µg/LSB (±2 g)	5 mdps/LSB (±100 dps)	61 µg/LSB (±2 g)	4.4 mdps/LSB (±125 dps)

Table 4.4: Specifications of the inertial MEMS sensors [60]–[62].

4.3.3 Flux Density

To measure the flux density in the air gap of the EPMs the linear analogue Hall sensor *HE144* (Asensor Technology, Sweden) is used. It has a thickness of only 0.5 mm and therefore still allows a small air gap. For operation, it requires a constant current of 1 mA, for which the sensitivity is 0.2 V/T [63]. Additionally, each EPM is equipped with a search coil consisting of 20 turns of a 0.1 mm thick copper wire.

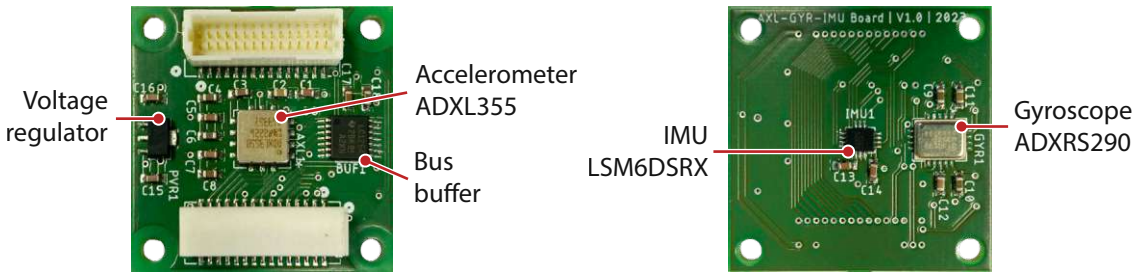

(a) Top side. **(b)** Bottom side.

Figure 4.6: PCB with the inertial sensors.

The sensors provide a voltage, which has to be filtered and amplified. For this purpose, the circuit board shown in Figure 4.7 was designed. Each of the six channels consists of a differential and common-mode low-pass filter, followed by an instrumentation amplifier and a second-order Sallen-Key low-pass filter. Moreover, there is also a temperature-compensated current source for the Hall sensors.

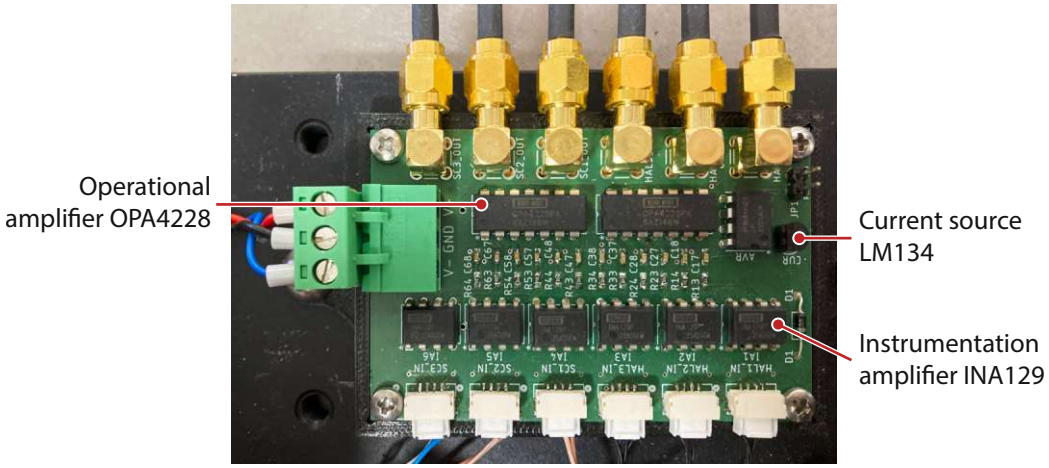

Figure 4.7: PCB with the amplifiers and filters for the Hall sensors and the search coils.

4.4 Data Acquisition and Control

The control of the platform is implemented on the rapid-prototyping system *MicroLabBox DS1202* (dSPACE, Germany). It provides analogue-to-digital converters (ADC) and digital-to-analogue converters (DAC) to record the sensor signals and control the external electronics. Moreover, digital inputs and outputs as well as a serial peripheral interface (SPI) are available for the communication with the digital sensors. The position control and active vibration suppression runs on a CPU with a clock frequency of 25 kHz. Due to

the higher timing requirements, the control of the current pulse generator is implemented on the included FPGA, which runs at 100 MHz. The programming is mainly done in MATLAB/SIMULINK and partly in C.

Chapter 5

Identification of the Platform Dynamics and Control Design

The first part of this chapter is concerned with the identification of the dynamic behaviour of the levitating platform. As it is open-loop unstable, this can only be done in closed-loop operation. Therefore, a position controller must be implemented beforehand. Subsequently, the controllers required for vibration suppression are designed. The last section provides an overview of the overall control concept and the interaction between the individual controllers.

5.1 Closed-loop Identification

The identification of the platform dynamics poses a challenge, as it can only be done in a levitating state. However, this requires the implementation of a stable position controller, for which the frequency behaviour of the platform must already be known. But since this is not the case, the controller must be designed based only on the model. The details on the design and the control loop are explained in the following section. Using the implemented position control, the transfer function matrix is measured, and the coupling between the six DoFs is examined. Also, the platform travel and the motor constant of the vertical actuators are determined.

5.1.1 Position Control

Since the platform can be positioned in six DoFs by the six actuators, it is a multi-input multi-output (MIMO) system. The controller design for such systems must take into account the coupling between the DoFs, and is therefore more complex than for a single-input single-output (SISO) system. However, as shown in Sections 3.5.2 and 3.5.3,

decoupling can be achieved by suitable transformation of the actuator forces and sensor signals. This means that a SISO controller can be used for each axis, which is also referred to as decentralised control.

Model of the control loop

The complete position control loop, including the decoupling transformations, is shown in Figure 5.1. Using decentralised control, the position controller R_p is given by the following diagonal matrix, with the six SISO controllers on the main diagonal

$$R_p(s) = \begin{bmatrix} R_{p,x} & 0 & \dots & \dots & \dots & 0 \\ 0 & R_{p,y} & \ddots & & & \vdots \\ \vdots & \ddots & R_{p,z} & \ddots & & \vdots \\ \vdots & & \ddots & R_{p,\alpha} & \ddots & \vdots \\ \vdots & & & \ddots & R_{p,\beta} & 0 \\ 0 & \dots & \dots & \dots & 0 & R_{p,\gamma} \end{bmatrix}. \tag{5.1}$$

The controller determines the required resulting forces and torques $\boldsymbol{u}$ (see Equation 3.5) from the position error $\boldsymbol{e} = \boldsymbol{x}_p - \boldsymbol{x}$, where $\boldsymbol{x}_p$ and $\boldsymbol{x}$ denote the reference and measured position of the platform, respectively. The relationship between $\boldsymbol{u}$ and the actuator forces $\boldsymbol{f}$ is given by Equation 3.9. Thus, $\boldsymbol{f}$ is determined by applying the inverse transformation V^{-1} to $\boldsymbol{u}$. From the required actuator forces, the corresponding currents $\boldsymbol{i}$ are calculated by multiplication with the inverse motor constant matrix K_M^{-1} according to Equation 3.12.

At this point, the control loop leaves the digital domain of the rapid-prototyping system through its DACs. The analogue current controllers and maintain the desired current in the actuators by another feedback loop with a bandwidth of 10 kHz (see Section 4.2.1). The transfer function L_i comprises the current controller, power amplifier and electrical plant of the actuator. Since this control loop is significantly faster than the position control loop, its dynamics are neglected. The actuators convert the currents into forces $\tilde{\boldsymbol{f}}$ according to the real motor constant matrix $\tilde{K}_M$. On the platform, the actuator forces are superposed by the transformation $\tilde{V}$, resulting in the forces and torques $\tilde{\boldsymbol{u}}$. They cause a displacement of the platform $\tilde{x}$ according to the decoupled transfer function matrix $\tilde{G}$. The displacement of the platform is measured by the sensors according to the transformation $\tilde{W}$. Their output signals $\boldsymbol{y}$ enter the digital domain through the ADCs of the rapid-prototyping system. The position and orientation of the platform $\boldsymbol{x}$ is calculated by applying the inverse transformation W^{-1}.

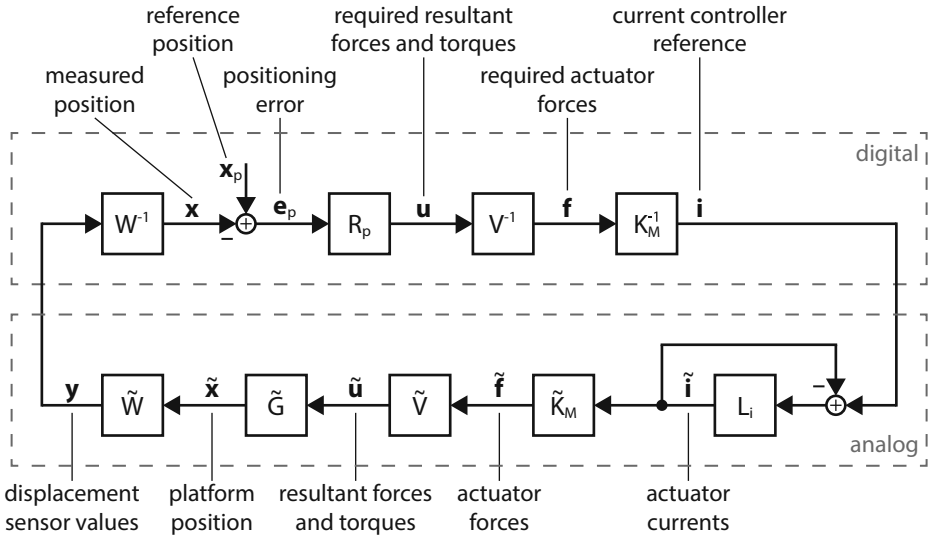

Figure 5.1: Position control loop, including the decoupling transformations and the current control loop.

The transformations $\tilde{V}$ and $\tilde{W}$ are modelled by the matrices V and W according to Sections 3.5.2 and 3.5.3. These depend on the dimensions of the sensor and actuator arrangement, and the location of the platform's centre of gravity. The former are fixed and provided in Table 5.1 together with the motor constants of the actuators (see Section 4.2). The position of the centre of gravity, however, depends on the payload placed on the platform and must therefore be adjusted when the load is changed. Table 5.2 provides the values for the unloaded case. It also contains the mass and moment of inertia of the platform without payload. These values determine the transfer function $\tilde{G}$ and its model G (see Equation 3.8). The accuracy and performance of the position control are determined by the quality of this model.

r_V^A	68 mm	r_H^A	100 mm
z_V^A	30 mm	z_H^A	30 mm
$K_{V1,V2,V3}$	27.5 N/A	$K_{H1,H2,H3}$	2 N/A
r_V^S	102.04 mm	r_H^S	106.11 mm
z_V^S	59.5 mm	z_H^S	45 mm
φ_V^S	−0.424 rad	φ_H^S	2.801 rad

Table 5.1: Values of the load-independent model parameters.

m	1.88 kg	J_x	8.10 gm^2
x_s	0 mm	J_y	8.08 gm^2
y_s	0 mm	J_z	14.53 gm^2
z_s	35 mm		

Table 5.2: Values of the load-dependent model parameters for the unloaded case (without payload).

Implementation and tuning

For the implementation of the six SISO controllers in Equation 5.1, proportional-integral-derivative (PID) control is used, which is widely applied in positioning systems [21], [64]. The transfer function of a single SISO controller is expressed as follows

$$R(s) = k_p + \frac{k_i}{s} + \frac{k_d s}{1 + \frac{s}{\omega_d}}\,. \tag{5.2}$$

The coefficients k_p, k_i, k_d and ω_d are determined using the α-tuning method [64] and are given by

$$k_p = \frac{1}{\alpha\,|G(j\omega_c)|}, \qquad k_i = k_p \frac{\omega_c}{\alpha^2}, \qquad k_d = k_p \frac{\alpha}{\omega_c}, \qquad \omega_d = \alpha\,\omega_c\,. \tag{5.3}$$

Thus, only the crossover frequency ω_c, the magnitude of the transfer function $G(s)$ of the respective axis at that frequency, and the tuning parameter α are required. The first-order low-pass with the cutoff frequency ω_d is added to tame the differentiator at high frequencies [64].

Since no identification data is available for the initial tuning of the parameters, the model presented in Section 3.5.1 must be used. In this idealised model, the platform is assumed to be a free-floating body, which is of course not entirely accurate. Firstly, a certain stiffness is expected to be observed at low frequencies due to the supply cables of the actuator coils and secondly, structural modes will appear at higher frequencies. However, prior to identification, these influences are not known. The only parameters that can be assumed to be fairly accurate are the platform's mass and moment of inertia (see Table 5.2). The controller bandwidth is therefore chosen in the range of the mass line, but must not be too high in order to avoid problems with structural modes. In addition, the controller should be robust in order to ensure stability also under parameter deviations. This can be achieved by choosing a high value for the parameter α [64].

The identification of the platform's dynamic behaviour is explained in detail in Section 5.1.4. With the obtained data, the controller parameters were retuned, and the process repeated until a sufficiently accurate identification was achieved. Table 5.3 provides the final parameter values, which were used for all measurements presented in this chapter, unless it is stated otherwise.

Axis	$\boldsymbol{\alpha}$	$\boldsymbol{f_c}$	$\boldsymbol{k_p}$	$\boldsymbol{k_i}$	$\boldsymbol{k_d}$	$\boldsymbol{\omega_d}$
		Hz	**N/m**	**N/(m s)**	**N s/m**	**1/s**
x	3	20	$5.81 \cdot 10^3$	$6.08 \cdot 10^4$	185	283
y	3	20	$4.89 \cdot 10^3$	$5.12 \cdot 10^4$	155	283
z	3	30	$2.16 \cdot 10^4$	$4.53 \cdot 10^5$	344	565
Axis	$\boldsymbol{\alpha}$	$\boldsymbol{f_c}$	$\boldsymbol{k_p}$	$\boldsymbol{k_i}$	$\boldsymbol{k_d}$	$\boldsymbol{\omega_d}$
		Hz	**N m/rad**	**N m/(rad s)**	**N m s/rad**	**1/s**
α	3	30	83.7	$1.75 \cdot 10^3$	1.33	565
β	3	30	84.0	$1.76 \cdot 10^3$	1.34	565
γ	3	20	38.6	404	1.23	283

Table 5.3: Parameters of the six SISO PID position controllers used for identification.

5.1.2 Platform Travel

The positioning range of the platform was determined by moving it to the mechanical limit on either side of each degree of freedom. The centre position is found by taking the average of the minimum and maximum values. Table 5.4 shows the maximum travel in each axis from the centre position.

x	± 0.33 mm	α	± 4.5 mrad ($\pm 0.26°$)
y	± 0.41 mm	β	± 4.7 mrad ($\pm 0.27°$)
z	± 0.35 mm	γ	± 4.2 mrad ($\pm 0.24°$)

Table 5.4: Travel of the platform around its centre position.

The travel range is primarily limited by the air gap of the voice coil actuators, which is 0.5 mm. Other limitations include assembly and alignment tolerances, as well as additional mechanical stops to prevent damage to the actuator coils from collisions.

5.1.3 Motor Constant of Vertical Actuators

As the vertical actuators were manufactured by hand, a relatively large variation in the motor constants can be expected. In order to obtain the values, which are needed to correctly calculated the reference signals for the current controllers, the static current required

to support the weight of the platform without gravity compensation was measured. To calculate the values listed in Table 5.5, it was assumed that the weight of 1.88 kg is equally distributed over all three actuators. The variation between the three actuators is around 10 %, but the values correspond well with estimation in Section 4.2.

Actuator	Motor constant N/A
V1	27.0
V2	29.0
V3	30.4

Table 5.5: Motor constants of the vertical Lorentz actuators.

5.1.4 Transfer Function Matrix

In the idealised model of Section 3.5.1, it is assumed that the transfer function matrix $G(s)$ is perfectly decoupled and therefore diagonal. The decoupling is achieved by a transformation which results from the geometry of the platform. In reality, however, the dimensions will deviate from those in the model due to inaccuracies in manufacturing and assembly. This means that if, for example, the controller sets a force or torque for one axis, it will not only affect the intended axis, but possibly all others as well. Consequently, the off-diagonal elements of the transfer function matrix $\hat{G}(s)$, which is given below, are not equal to zero.

$$\underbrace{\mathcal{L}\begin{bmatrix} x \\ y \\ z \\ \alpha \\ \beta \\ \gamma \end{bmatrix}(s)}_{\mathcal{L}\{\boldsymbol{x}\}(s)} = \underbrace{\begin{bmatrix} G_{xx} & G_{xy} & \dots & \dots & \dots & G_{x\gamma} \\ G_{yx} & G_{yy} & \ddots & & & \vdots \\ \vdots & \ddots & G_{zz} & \ddots & & \vdots \\ \vdots & & \ddots & G_{\alpha\alpha} & \ddots & \vdots \\ \vdots & & & \ddots & G_{\beta\beta} & G_{\beta\gamma} \\ G_{\gamma x} & \dots & \dots & \dots & G_{\gamma\beta} & G_{\gamma\gamma} \end{bmatrix}}_{\hat{G}(s)} \underbrace{\mathcal{L}\begin{bmatrix} F_x \\ F_y \\ F_z \\ M_\alpha \\ M_\beta \\ M_\gamma \end{bmatrix}(s)}_{\mathcal{L}\{\boldsymbol{u}\}(s)} \tag{5.4}$$

For an open-loop stable system, the entries of this matrix could simply be determined by applying a force or torque to each axis separately and measuring the frequency responses. However, the platform can only be identified in closed-loop operation, as it is open-loop unstable and must be held in the centre position by the controller. With the above identification method, the measurement results would be distorted by the additional forces and torques applied by the position controller for stabilisation.

To account for this, the first step is to do at least as many independent measurements as there are control variables. In these measurements, the system is excited, for example, by applying a sinusoidal reference signal to one axis, while the position and force are recorded for all axes. Next, the signals are Fourier transformed and combined into matrices, resulting in the following expression for each frequency ω_k [65]

$$\underbrace{\begin{bmatrix}\boldsymbol{x}_1(\omega_k) & \boldsymbol{x}_2(\omega_k) & \dots & \boldsymbol{x}_n(\omega_k)\end{bmatrix}}_{\hat{X}(\omega_k)\in\mathbb{C}^{6\times n}} = \hat{G}(\omega_k) \underbrace{\begin{bmatrix}\boldsymbol{u}_1(\omega_k) & \boldsymbol{u}_2(\omega_k) & \dots & \boldsymbol{u}_n(\omega_k)\end{bmatrix}}_{\hat{U}(\omega_k)\in\mathbb{C}^{6\times n}}, \tag{5.5}$$

where $\hat{G}(\omega_k) \in \mathbb{C}^{6\times 6}$ denotes the identified transfer function matrix, and $\boldsymbol{x}_i(\omega_k) \in \mathbb{C}^{6\times 1}$ and $\boldsymbol{u}_i(\omega_k) \in \mathbb{C}^{6\times 1}$ the discrete Fourier transforms at the frequency ω_k of the sampled position and input signals of the i-th measurement, respectively. If the number of measurements n equals the number of control variables, the matrix $\hat{U}(\omega_k)$ is quadratic and can be inverted, otherwise the pseudo inverse (denoted by $\hat{U}^\dagger(\omega_k)$) can be used to determine $\hat{G}(\omega_k)$ for each frequency ω_k

$$\hat{G}(\omega_k) = \hat{X}(\omega_k)\hat{U}^\dagger(\omega_k). \tag{5.6}$$

Figure 5.2 shows the 36 magnitude plots of the elements in $\hat{G}$, calculated according to the equation above using six measurements. The plots on the main diagonal also contain the magnitude plot of the floating-mass model in Equation 3.8 with the parameters of Table 5.2. For easier interpretation, the Bode plots of the six main axes are enlarged in Figure 5.3. The frequency responses resemble the behaviour of a damped spring-mass system. In the frequency range from 10 to 100 Hz (for the out-of-plane DoFs up to 200 Hz) there is very good agreement with the floating-mass model. Since the mounting of the actuator movers is more compliant in the horizontal direction, the first decoupling modes can already be observed at around 100 Hz in the in-plane DoFs (x, y, γ), while these only occur above 200 Hz in the out-of-plane DoFs (z, α, β). The stiffness, which dominates the behaviour at low frequencies, is presumably caused by the cables leading to the actuator coils and acceleration sensors. The cross-coupling that can be observed in the off-diagonal elements of Figure 5.2 is examined in the following section.

5.1.5 Cross-coupling

For the controller design, the cross-coupling of the axes must be assessed, as SISO controllers are not suitable if the coupling is too strong. However, an evaluation based on the identified transfer functions shown in Figure 5.2 is only possible separately for the translational and rotational degrees of freedom. The interpretation of the coupling between translational and rotational axes is difficult due to the different physical dimensions.

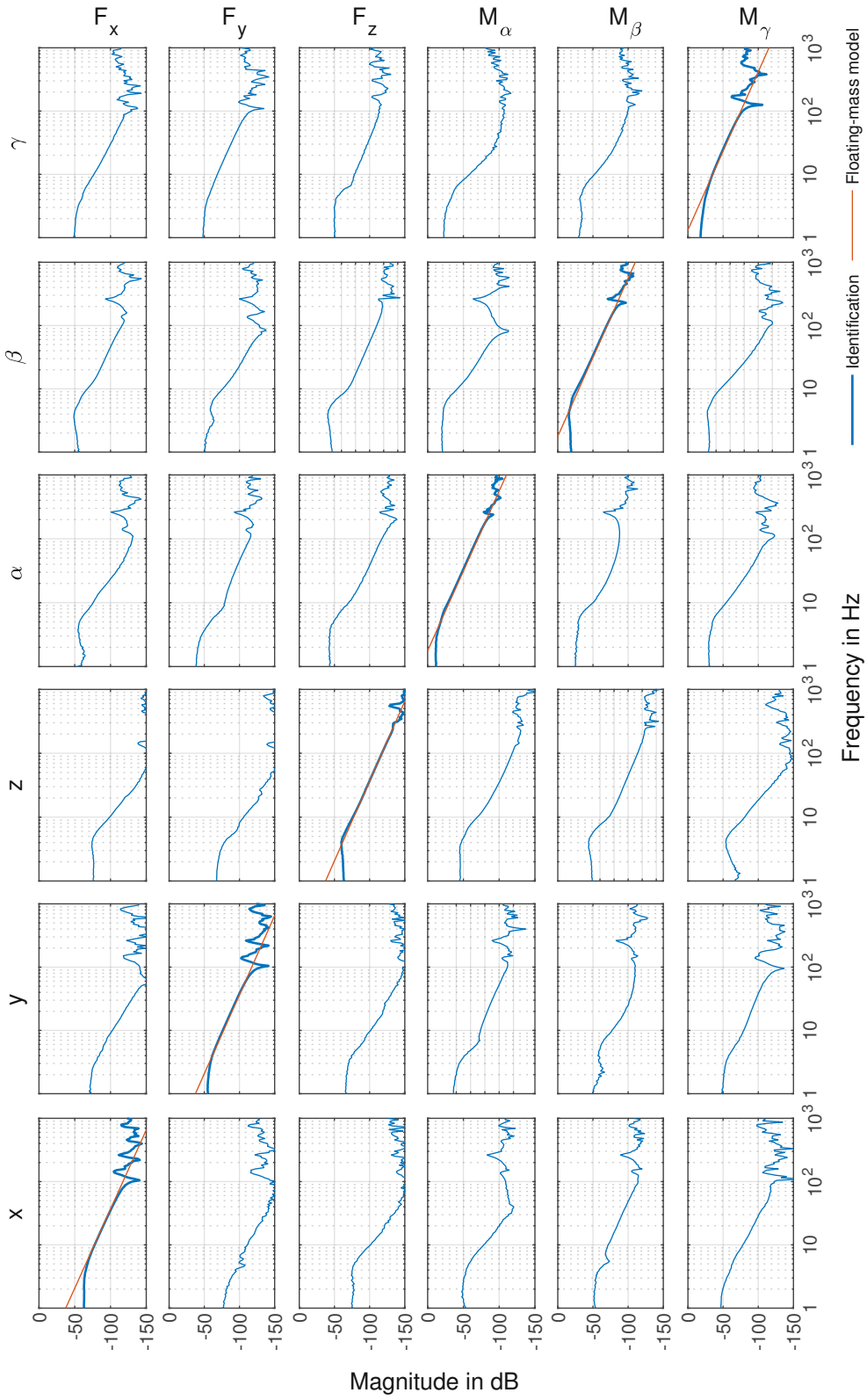

Figure 5.2: Magnitude plots of the transfer function matrix (identified in closed-loop operation without gravity compensation).

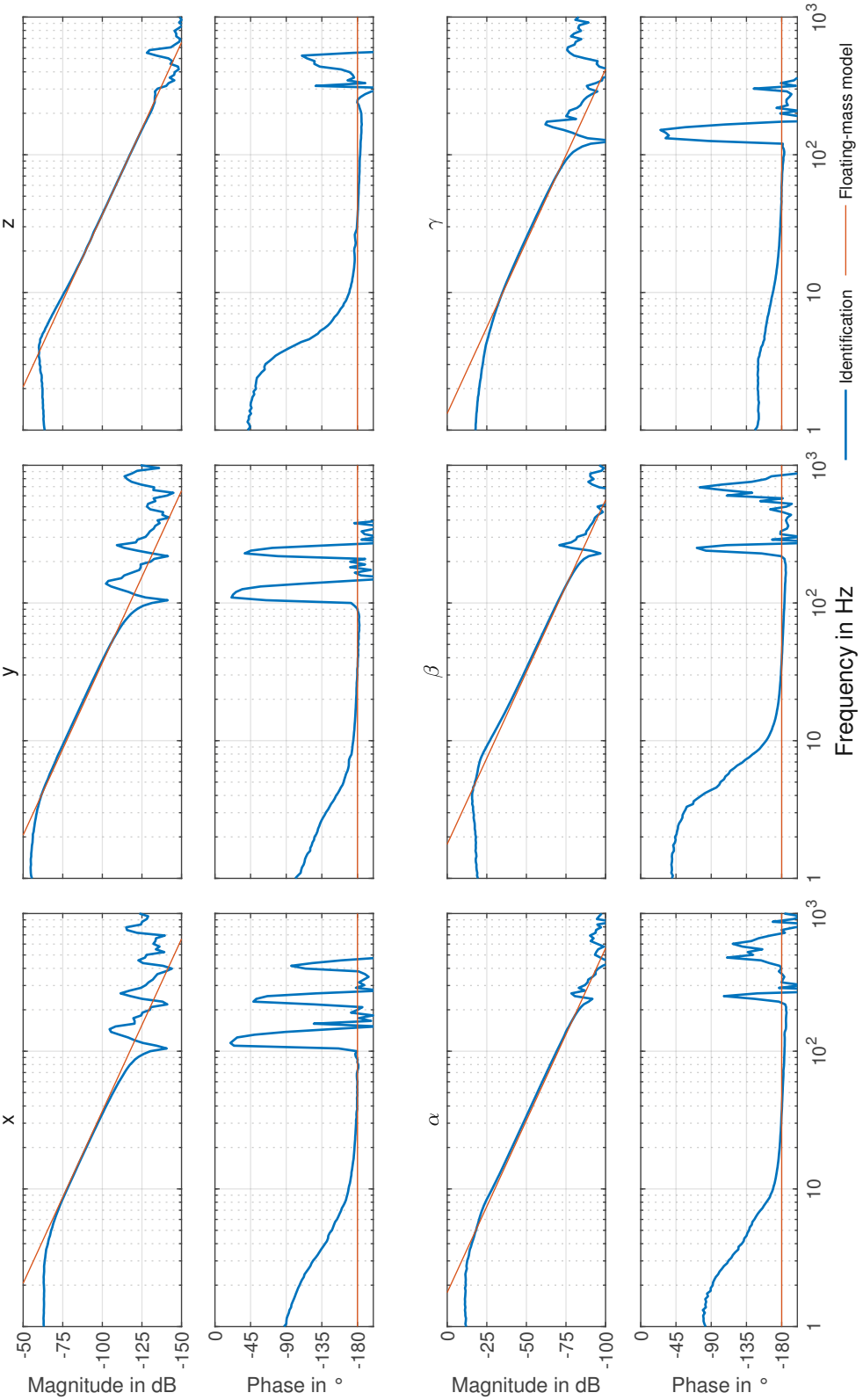

Figure 5.3: Bode plots of the transfer functions of the six main axes (identified in closed-loop operation without gravity compensation).

A measure to assess the cross-coupling between axes with different units is the so-called *relative gain array* (RGA). For a non-singular complex square matrix $\hat{G}$, it is defined as follows [66]

$$\Lambda(\hat{G}) = \hat{G} \circ \left(\hat{G}^{-1}\right)^{\mathrm{T}}. \tag{5.7}$$

where $\circ$ denotes the element-wise (also Hadamard or Schur) product of two matrices. The advantage of this measure is that it is independent of the scaling and the units of the inputs and outputs. This matrix can be calculated for every frequency ω_k, at which the transfer function matrix $\hat{G}(\omega_k)$ was identified. For stability, it is usually sufficient if the RGA is approximately an identity matrix in the range around the crossover frequency. If this is the case, the transfer function matrix has the form of an upper or lower diagonal matrix, which means that only one-way coupling is present. In this case, decentralised control is able to stabilise the system. However, a strong coupling can have a negative effect on the performance. [66]

Figure 5.4 shows the magnitude plots of the RGA matrix, which was calculated according to Equation 5.7 from the transfer function matrix presented in Figure 5.2. Up to a frequency of about 100 Hz, the main diagonal elements are close to 0 dB, and the off-diagonal elements are at least 10 dB lower. In the range of the mass line (between 10 Hz and 100 Hz), the decoupling is particularly good. For this reason, the decentralised control approach with the six SISO controllers is retained.

5.2 Acceleration Feedback

The aim of position control is to keep the distance between the base, where the position sensors are mounted, and the platform constant. Consequently, ground vibrations are transferred to the platform within the control bandwidth. In contrast, vibration isolation aims to suppress the transmission by decoupling the platform from the base. Hence, the two pursue opposing goals and must be separated in terms of their bandwidths [24].

With the focus on vibration isolation, the bandwidth of the position control should be as small as possible. However, as explained in more detail in Section 5.3, it cannot be made arbitrarily small due to the negative stiffness caused by gravity compensation. This also limits the vibration isolation, which can only be active above the position control bandwidth. There is also a limit at higher frequencies due to structural modes and the dead time of the inertial sensors. Fortunately, this is less of a problem, as high-frequency disturbances are suppressed anyway by the inertia of the mass.

With feedback and feedforward control, two possible approaches for vibration isolation were presented in the state of the art. The latter is more challenging to implement, because it requires precise knowledge of the transmissibility, which can be difficult to measure. Moreover, as shown in Section 5.3, the EPMs cause a non-linear negative stiffness in

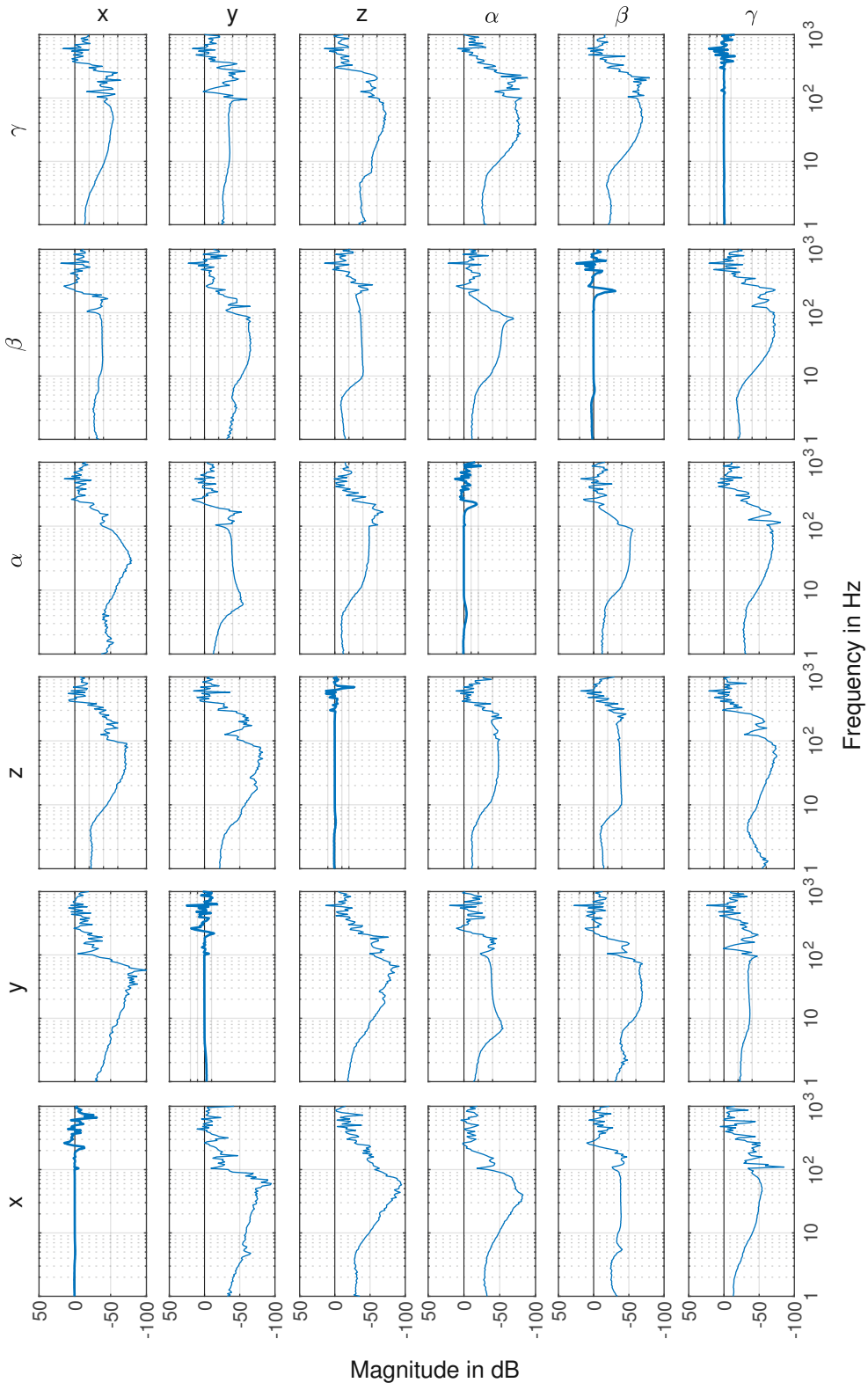

Figure 5.4: Magnitude plots of the relative gain array (identified in closed-loop operation without gravity compensation).

the vertical direction. Thus, feedback control is implemented, which uses inertial sensors mounted on the platform to generate a virtual mass, damping and stiffness. The additional stiffness reduces the transmissibility at low frequencies and can therefore not be used in this case due to the position control. It is also not necessary to add damping, since there is almost no resonance peak. Nevertheless, increasing the effective mass helps to suppress vibrations above the position control bandwidth.

Figure 5.5 shows the extended control loop, with the added acceleration feedback highlighted in red. Similar to the position sensors, the inertial sensors are not aligned with the platform coordinate system and therefore only provide the transformed acceleration signal $\ddot{y}_a$ instead of $\tilde{\ddot{x}}$. The transformation $\tilde{W}_a$ is modelled by the matrix W_a, which is used to calculate the acceleration of the platform $\ddot{x}$ from the sensor values. Since the reference for the feedback controller R_a is zero, it tries to suppress the acceleration of the platform by applying appropriate counterforces and -torques.

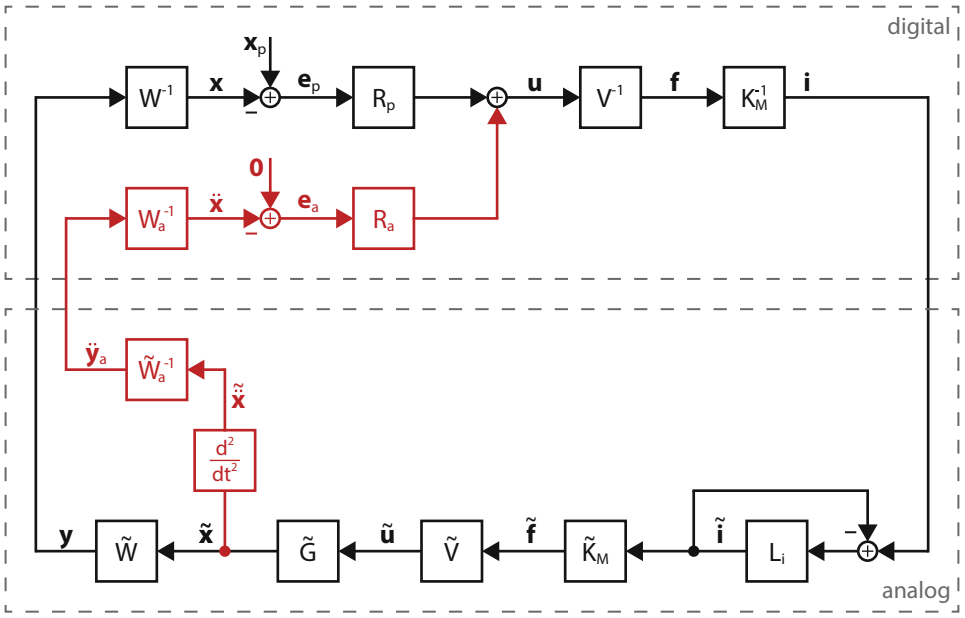

Figure 5.5: Position control loop extended with acceleration feedback highlighted in red.

Since ground vibrations primarily act on the isolation system in the vertical direction, acceleration feedback is only implemented for the z-axis, and consequently only the acceleration of the platform in z-direction is considered. Therefore, the acceleration feedback controller can be reduced to a scalar $R_a(s) = R_{a,z}(s)$. The transformation of the sensor signal is $W_a = -1$, because the accelerometer on the platform is mounted upside-down. Figure 5.6 shows the simplified control loop of the z-axis, where G_z represents the transfer function from the controller output F_z to the position of the platform z obtained from the transformation of the sensor signals.

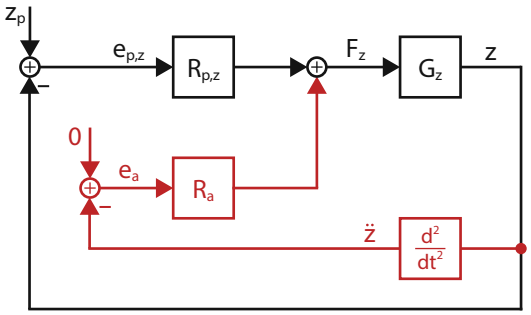

Figure 5.6: Simplified diagram of the position control loop of the z-axis with acceleration feedback highlighted in red.

When either the position control loop or the acceleration control loop is closed at a time, the following open-loop transfer functions are obtained[1]

$$L_{p,z} = \frac{\mathcal{L}\{z\}}{\mathcal{L}\{e_{p,z}\}} = \frac{G_z R_{p,z}}{1 + s^2 G_z R_a} \tag{5.8}$$

$$L_a = \frac{\mathcal{L}\{\ddot{z}\}}{\mathcal{L}\{e_a\}} = \frac{s^2 G_z R_a}{1 + G_z R_{p,z}} \tag{5.9}$$

where $L_{p,z}$ describes the open loop of the position control with closed acceleration feedback and L_a the reverse case. G_z is the platform's transfer function in z-direction. If the two controllers $R_{p,z}$ and R_a are designed to operate in separate frequency ranges, the approximations $L_{p,z} \approx G_z R_{p,z}$ and $L_a \approx s^2 G_z R_a$ can be used. The separation is achieved by setting the bandwidth of the position control is sufficiently lower than the frequency at which the acceleration feedback starts. In this case, the mutual influence of the position control and the vibration suppression can be neglected. This allows the stability of the two control loops to be treated separately. For position control, a stable controller has already been designed in Section 5.1.1, which is therefore taken as given here.

The acceleration feedback controller R_a is designed based on the frequency response of the platform in z-direction $s^2 G_z$. For this purpose, a Bode diagram of the transfer function from the resulting force in the z-direction to the corresponding acceleration was recorded using the accelerometer *ADXL355*. As can be seen in Figure 5.7, the magnitude first increases with frequency (corresponding to the spring line) and then continues horizontally (corresponding to the mass line) until structural modes occur at around 300 Hz. The phase decreases from initially 180° to 0° and is further reduced at higher frequencies due to the time lag of the sensor.

The first task of the controller R_a is to reduce the amplitude within the bandwidth of the position control in order to avoid a conflict between them. Furthermore, proportional gain is required to generate a virtual mass. This may shift the magnitude of the open-loop

[1]For better readability, the dependence of the Laplace transform on the variable s is omitted in the following derivations.

above the 0 dB-line, requiring sufficient phase margin at the crossover in order to ensure stability. For the same reason, the 0 dB-line must be crossed again, before the phase drops below $-180°$ at higher frequencies. In Figure 5.7, the two crossings of the 0 dB-line are indicated by the dashed black lines. Moreover, the structural modes must be suppressed by appropriate filters. The requirement for sufficient phase margin at both crossovers limits the achievable gain, meaning that a smaller bandwidth allows for a larger virtual mass and better suppression within that range and vice versa. This trade-off must be considered in the controller design. Based on these considerations, the entire controller is given by

$$R_a(s) = g_a \, H_{hp}(s) \, H_{lp}(s) \, H_n(s) \, H_{lead}(s) \, H_{lag}(s) \, H_{sm}(s), \tag{5.10}$$

where

$$H_{hp}(s) = \frac{\frac{s}{2\pi f_1}}{1 + \frac{s}{2\pi f_1}}, \qquad \dots \text{ high-pass filter}$$

$$H_{lp}(s) = \frac{1}{1 + \frac{s}{2\pi f_2}}, \qquad \dots \text{ low-pass filter}$$

$$H_n(s) = \frac{1 + 2\zeta_{31}\frac{s}{2\pi f_3} + \left(\frac{s}{2\pi f_3}\right)^2}{1 + 2\zeta_{32}\frac{s}{2\pi f_3} + \left(\frac{s}{2\pi f_3}\right)^2}, \qquad \dots \text{ notch filter}$$

$$H_{lead}(s) = \frac{2\pi f_{42}}{2\pi f_{41}} \frac{1 + \sqrt{2}\frac{s}{2\pi f_{41}} + \left(\frac{s}{2\pi f_{41}}\right)^2}{1 + \sqrt{2}\frac{s}{2\pi f_{42}} + \left(\frac{s}{2\pi f_{42}}\right)^2}, \qquad \dots \text{ lead compensator}$$

$$H_{lag}(s) = \frac{1 + \sqrt{2}\frac{s}{2\pi f_{51}} + \left(\frac{s}{2\pi f_{51}}\right)^2}{1 + \sqrt{2}\frac{s}{2\pi f_{52}} + \left(\frac{s}{2\pi f_{52}}\right)^2}, \qquad \dots \text{ lag compensator}$$

$$H_{sm}(s) = \frac{1 + 2\zeta_{61}\frac{s}{2\pi f_{61}} + \left(\frac{s}{2\pi f_{61}}\right)^2}{1 + 2\zeta_{61}\frac{s}{2\pi f_{62}} + \left(\frac{s}{2\pi f_{62}}\right)^2}, \frac{1 + 2\zeta_{63}\frac{s}{2\pi f_{63}} + \left(\frac{s}{2\pi f_{63}}\right)^2}{1 + 2\zeta_{63}\frac{s}{2\pi f_{64}} + \left(\frac{s}{2\pi f_{64}}\right)^2}. \dots \text{ structural modes filter}$$

The gain g_a determines the virtual mass that is generated by the feedback. Due to the gravitational acceleration, the sensor signal has a large offset, which is removed by the first-order high-pass filter $H_{hp}(s)$. To ensure the separation from position control, the second-order lead compensator $H_{lead}(s)$ reduces the amplitude. It is used instead of another high-pass filter, because there is less phase lift and the plant acts already as a second-order high-pass anyway. The notch filter $H_n(s)$ removes the small resonance peak and makes the amplitude response smoother. The second-order lag compensator $H_{lag}(s)$ is used to achieve a crossing of the 0 dB-line at higher frequencies without reducing the phase significantly. The additional first-order low-pass filter $H_{lp}(s)$ attenuates residual structural modes that

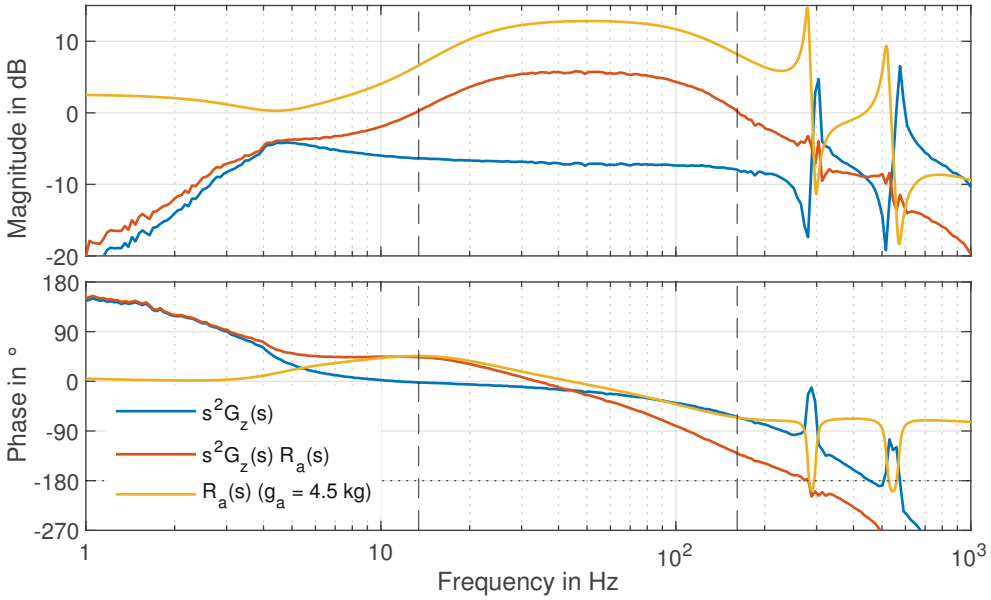

Figure 5.7: Bode plots of the plant in the z-direction seen by the acceleration feedback controller R_a (blue), the open-loop transfer function (red), and the acceleration feedback controller R_a with a gain $g_a = 4.5\,\mathrm{kg}$ (yellow).

have not been removed by the compensator $H_{sm}(s)$. Table 5.6 provides the chosen filter coefficients, and Figure 5.7 shows both the unfiltered and filtered plant, as well as the transfer function of the controller R_a.

f_1	0.1 Hz	f_{41}	13 Hz	f_{62}	298 Hz
f_2	500 Hz	f_{42}	20 Hz	f_{63}	519 Hz
f_3	4.5 Hz	f_{51}	250 Hz	f_{64}	569 Hz
ζ_{31}	1.25	f_{52}	125 Hz	ζ_{61}	0.015
ζ_{32}	0.6	f_{61}	280 Hz	ζ_{63}	0.02

Table 5.6: Parameters of the acceleration feedback controller in Equation 5.10.

The effect of position control and vibration suppression on the transmissibility of the active vibration isolation system can be explained using Equation 2.2. The externally applied force F_d is in this case the sum of the forces generated by the position and acceleration controllers $R_{p,z}$ and R_a. The compliance $\mathcal{C}$, which describes the reaction of the platform to this force, is given by the transfer function in z-direction G_z. Therefore, the equation can be written as

$$\mathcal{L}\{z\} = \mathcal{T}_z\mathcal{L}\{z_0\} + G_z R_{p,z} \underbrace{(\mathcal{L}\{z_0\} - \mathcal{L}\{z\})}_{\substack{\text{position}\\\text{error}}} + G_z R_a \underbrace{(0 - s^2\mathcal{L}\{z\})}_{\substack{\text{acceleration}\\\text{error}}}. \tag{5.11}$$

where $\mathcal{T}_z$ is the passive transmissibility in z-direction. Rewriting this equation, gives the transmissibility with active control

$$\frac{\mathcal{L}\{z\}}{\mathcal{L}\{z_0\}} = \frac{\frac{\mathcal{T}_z}{G_z} + R_{p,z}}{\frac{1}{G_z} + R_{p,z} + s^2 R_a}. \tag{5.12}$$

Assuming $G_z = \frac{1}{ms^2+cs+k}$ and $\mathcal{T}_z = \frac{cs+k}{ms^2+cs+k}$ yields

$$\frac{\mathcal{L}\{z\}}{\mathcal{L}\{z_0\}} = \frac{cs + k + R_{p,z}}{\underbrace{(m + R_a)}_{\text{effective mass}} s^2 + cs + \underbrace{k + R_{p_z}}_{\text{effective stiffness}}}. \tag{5.13}$$

This expression shows that the position controller $R_{p,z}$ extends the transmission of floor vibrations to its bandwidth by increasing the effective stiffness. In contrast, the acceleration feedback R_a adds a virtual mass, which reduces the transmissibility. The generation of additional virtual mass can be seen in the Bode plots in Figure 5.8. They show the transfer of the plant seen by the position controller with different values of the acceleration feedback gain g_a. This factor corresponds to an additional mass in kg and shifts the mass line downwards within the control bandwidth.

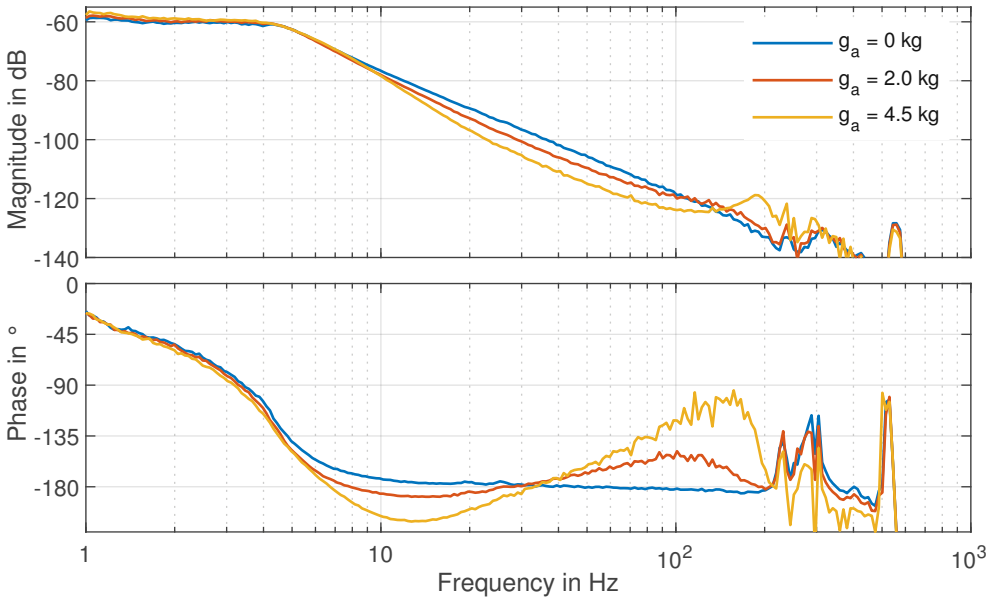

Figure 5.8: Bode plots of the plant in the z-direction seen by the position controller, showing the generation of an additional virtual mass by the acceleration feedback for different values of the gain g_a.

5.3 Gravity Compensation

The compensation of the weight of the platform and the payload is achieved by tuning the reluctance force of the EPMs. Since this force decreases when the air gap becomes larger, the EPMs have a negative stiffness. As a result, the overall stiffness of the platform may become negative in the vertical direction, when the flux density of the EPMs is increased in order to carry a heavier payload.

Figure 5.9 shows the Bode plot of the transfer function in z-direction from force to position without gravity compensation and when the weight of the platform is compensated by the EPMs. The first difference is that the phase in the compensated case already starts at $-180°$. The reason is that in this case the stiffness is negative and hence there is no resonance [21]. In addition, the absolute value of the stiffness is larger, which is why the spring line is shifted downwards.

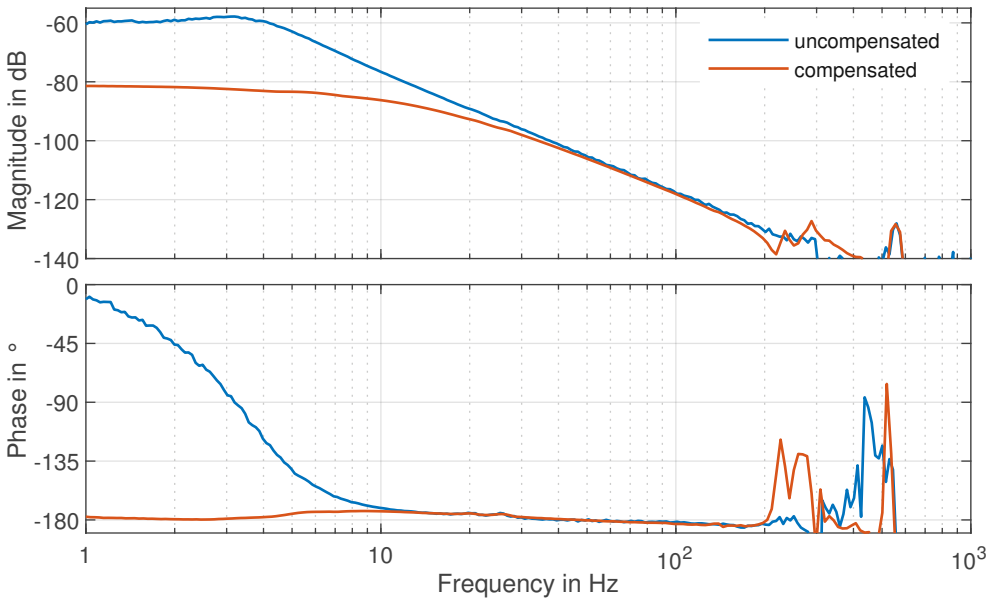

Figure 5.9: Bode plots of the plant in the z-direction seen by the position controller without gravity compensation (blue) and when the weight of the platform is compensated (red).

The transition from the descending mass line to the flat spring line represents a lower limit for the bandwidth of the PID position control. This is because, on the one hand, an integrator is required to achieve a crossing of the 0 dB-line in the flat region of the amplitude response and, on the other hand, a differentiator is needed in order to generate the phase margin necessary for stability. However, both cannot be achieved at the same time. This also limits the bandwidth of the vibration isolation, which must be higher than that of the position control.

To reduce the bandwidth of the position control and thus be able to extend the vibration isolation to lower frequencies, a further control loop is added, as shown in Figure 5.10. Like the acceleration feedback controller, the additional controller R_s is only active in the z-axis. Its purpose is to generate a positive stiffness at the operating point set by z_s in order to compensate the negative stiffness and shift the spring line upwards. This extends the mass line towards lower frequencies.

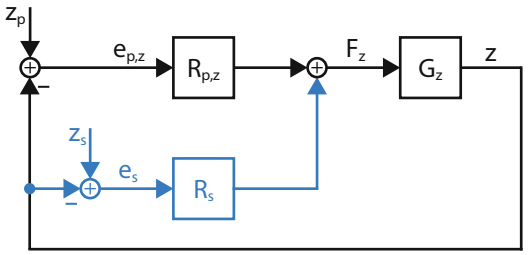

Figure 5.10: Simplified diagram of the position control loop of the z-axis with stiffness compensation highlighted in blue.

If both the position controller $R_{p,z}$ and the stiffness compensator R_s are active, the following expression is obtained for the closed control loop of the platform's z-coordinate[2]

$$\begin{aligned}\mathcal{L}\{z\} &= \frac{G_z R_{p,z}}{1+G_z R_{p,z}+G_z R_s}\mathcal{L}\{z_p\} + \frac{G_z R_s}{1+G_z R_{p,z}+G_z R_s}\mathcal{L}\{z_s\} \\ &= \underbrace{\frac{\frac{G_z R_{p,z}}{1+G_z R_s}}{1+\frac{G_z R_{p,z}}{1+G_z R_s}}}_{\frac{L_{p,z}}{1+L_p}}\mathcal{L}\{z_p\} + \underbrace{\frac{\frac{G_z R_s}{1+G_z R_{p,z}}}{1+\frac{G_z R_s}{1+G_z R_{p,z}}}}_{\frac{L_s}{1+L_s}}\mathcal{L}\{z_s\}\,, \end{aligned} \tag{5.14}$$

where z_p and z_s denote the reference signals of the respective controllers. $L_{p,z}$ and L_s are the open-loop transfer functions of the position and stiffness control loops when only one of them is closed at a time, and given by

$$L_{p,z} = \frac{G_z}{1+G_z R_s} R_{p,z}, \tag{5.15}$$

$$L_s = \frac{G_z}{1+G_z R_{p,z}} R_s. \tag{5.16}$$

[2]For better readability, the dependence of the Laplace transform on the variable s is omitted in the following derivations.

Using a simple proportional controller $R_s = k_s > 0$ and assuming a damped mass-spring system for the plant G_z yields the following expression for $L_{p,z}$

$$L_{p,z} = \frac{G_z}{1 + G_z R_s} R_{p,z} = \frac{1}{\frac{1}{G_z} + R_s} R_{p,z} = \frac{1}{ms^2 + cs + \underbrace{k + k_s}_{\text{effective stiffness}}} R_p. \tag{5.17}$$

This shows that the independent position feedback with the positive proportional gain k_s increases the effective stiffness of the plant seen by the position controller $R_{p,z}$. The two control loops are stable as long as k_s is not chosen so large that it changes the crossover of the position control loop. The value for k_s should be as close as possible to the absolute value of the negative stiffness.

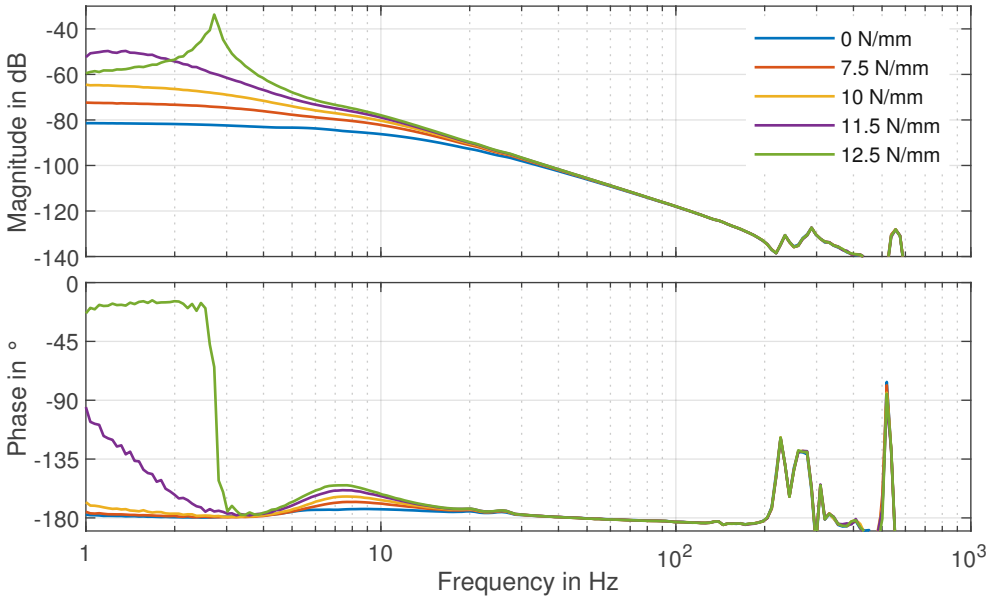

Figure 5.11: Bode plots of the plant in the z-direction seen by the position controller for different values of the virtual stiffness k_s with compensation of the platform weight.

To verify the statements above, the plant was again identified in close-loop operation, with both controllers active for different values of k_s. The resulting Bode plots of the plant in z-direction seen by the position controller are shown in Figure 5.11. As expected, the effective stiffness increases for larger values of k_s, but stays negative for $k_s \leq 10\,\text{N/mm}$. If the negative stiffness is overcompensated, as in the case of $k_s = 12.5\,\text{N/mm}$, the behaviour changes to that of a mass-spring system with positive stiffness, which is characterised by a resonance peak and a corresponding phase shift. A good compensation is obtained for $k_s = 11.5\,\text{N/mm}$, where the mass line starts at already at about 2 Hz. Besides that, a phase lift can be observed between 5 and 10 Hz, because the damping becomes more pronounced when the stiffness decreases.

5.4 Summary of the Control Concept

In this chapter, three different controllers were designed for the z-axis, which is the most relevant with regard to ground vibrations. The resulting control structure is depicted in Figure 5.12. Firstly, a position controller $R_{p,z}$ is required to keep the levitating platform in its operating position. This is also necessary for the other DoFs (see Section 5.1.1). Since the displacement sensors are mounted to the base, the position control tries to keep the distance between the base and the platform constant for a static reference. Thereby, the controller also transmits seismic vibrations within its bandwidth.

The purpose of the controller R_a is to suppress any motion of the platform with respect to an inertial reference, which is achieved by feeding back the acceleration $\ddot{z}$, as explained in Section 5.2. This improves the decoupling between the platform and base by adding a virtual mass. However, this is in conflict with the position control, which is why both controllers can only be active in separated frequency ranges. Consequently, the bandwidth of the position control sets a lower limit for the bandwidth of the acceleration feedback. The separation is achieved by a high-pass filter that suppresses the acceleration feedback below its cut-off frequency. This also means that both controllers can be designed independently of each other.

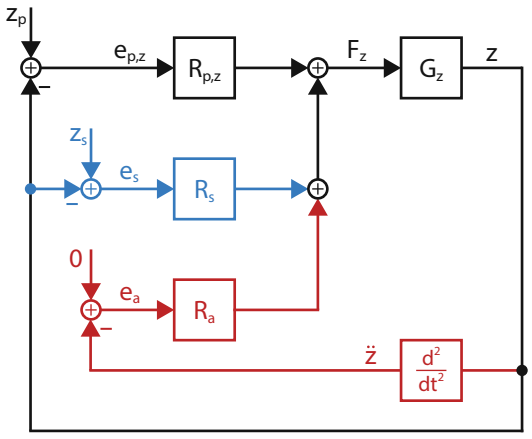

Figure 5.12: Simplified diagram of the control structure of the z-axis with position control, acceleration feedback (red) and stiffness compensation (blue).

In order to enable vibration suppression for low frequencies, the bandwidth of the position control should be set as low as possible. However, as discussed in Section 5.3, this is limited by the negative stiffness of the EPMs. For this reason, the controller R_s was introduced to compensate for the negative stiffness at the operating point of the platform. Accordingly, a careful design of all three controllers is required to achieve the desired vibration suppression behaviour.

Chapter 6

Evaluation of the System Performance

This chapter presents the evaluation of the three main functions of the implemented vibration isolation system: position control, gravity compensation and vibration suppression.

6.1 High-bandwidth Position Control

Even though for vibration isolation a low bandwidth of the position control is preferred, a faster controller was implemented to evaluate the performance of the decentralised control. The parameters of the six SISO PID controllers, which were used for the following measurements, were determined with the α-tuning method and are given in Table 6.1. With $\alpha = 3$, a good compromise between performance and robustness is achieved [64]. The crossover frequency f_c is limited by structural modes, but could be increased using suitable filters.

Figure 6.1 shows the complementary sensitivity and sensitivity functions of the six main axes without any additional filters. As can be seen, the intended bandwidth given Table 6.1 is achieved, but due to the decreasing phase there is a slight increase of the magnitude before the crossover. Moreover, the limiting structural modes are visible, which can be filtered to achieve a higher bandwidth using for example notch filters. The sensitivity functions show good suppression of disturbances acting on the position measurement within the bandwidth.

The maximum achievable resolution of the positioning is determined by the noise of the displacement sensors. Through the feedback, the noise is amplified, resulting in a trade-off between bandwidth and resolution. Table 6.3 specifies the RMS value of the noise which is present in the position signal of each axis. Comparing these values with the RMS noise of the individual sensors given in Table 6.2, shows that they are in the same

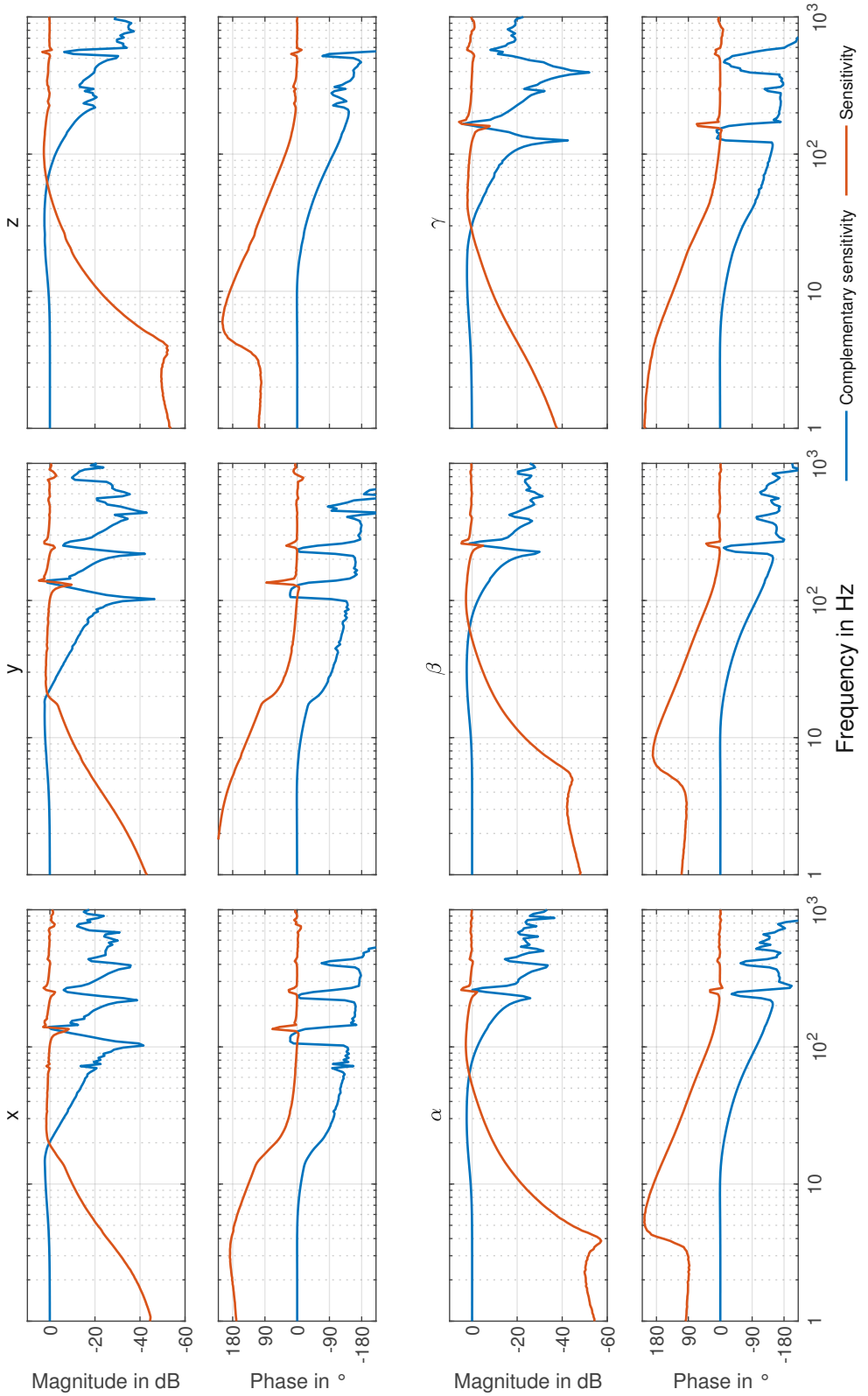

Figure 6.1: Complementary sensitivity and sensitivity functions of the six position control loops.

Axis	α	f_c	k_p	k_i	k_d	ω_d
		Hz	N/m	N/(m s)	N s/m	1/s
x	3	20	$2.39 \cdot 10^4$	$5.01 \cdot 10^5$	380	565
y	3	20	$2.00 \cdot 10^4$	$4.19 \cdot 10^5$	318	565
z	3	60	$8.82 \cdot 10^4$	$3.69 \cdot 10^6$	702	$1.13 \cdot 10^3$
Axis	α	f_c	k_p	k_i	k_d	ω_d
		Hz	N m/rad	N m/(rad s)	N m s/rad	1/s
α	3	60	336	$1.41 \cdot 10^4$	2.67	$1.13 \cdot 10^3$
β	3	60	345	$1.44 \cdot 10^4$	2.74	$1.13 \cdot 10^3$
γ	3	30	151	$3.16 \cdot 10^3$	2.40	565

Table 6.1: Parameters of the six SISO PID position controllers used for evaluation.

range, or even below. In particular, for the rotational degrees of freedom, the noise levels are significantly lower than those of the sensors. The reason for this is that the individual position coordinates of the platform are calculated as a weighted average of multiple sensor values. For example, the z-coordinate is the equally weighted average of the values of the three vertically mounted sensors V1, V2 and V3. Under the assumption of uncorrelated sources, this ideally reduces the noise by a factor of $1/\sqrt{3}$. In addition, for the rotational degrees of freedom, the angle is essentially determined by dividing the linear displacement by the distance of the sensors from the axis of rotation. The larger this lever arm, the better the signal-to-noise ratio (SNR).

A comparison of the measured sensor noise values given in Table 6.2 with the value specified by the manufacturer in Table 4.3 shows that the former are almost 100 times larger. The deviation can be explained in part by the fact, that the value specified in the data sheet refers to a bandwidth of 1 kHz, while for the measurement no other filter was used apart from the built-in 10 kHz low-pass filter. Other possible sources of noise might be the connecting cables to the rapid prototyping system and the DACs.

Sensor	RMS noise	Sensor	RMS noise
	nm		nm
V1	97.7	H1	99.9
V2	99.8	H2	128.9
V3	87.6	H3	67.1

Table 6.2: RMS noise of the displacement sensors.

The resolution of the position control can also be observed in Figure 6.2. For this measurement, each axis had to follow a step function with a step height of 0.5 µm in the linear and 0.5 mdeg in the rotational coordinates.

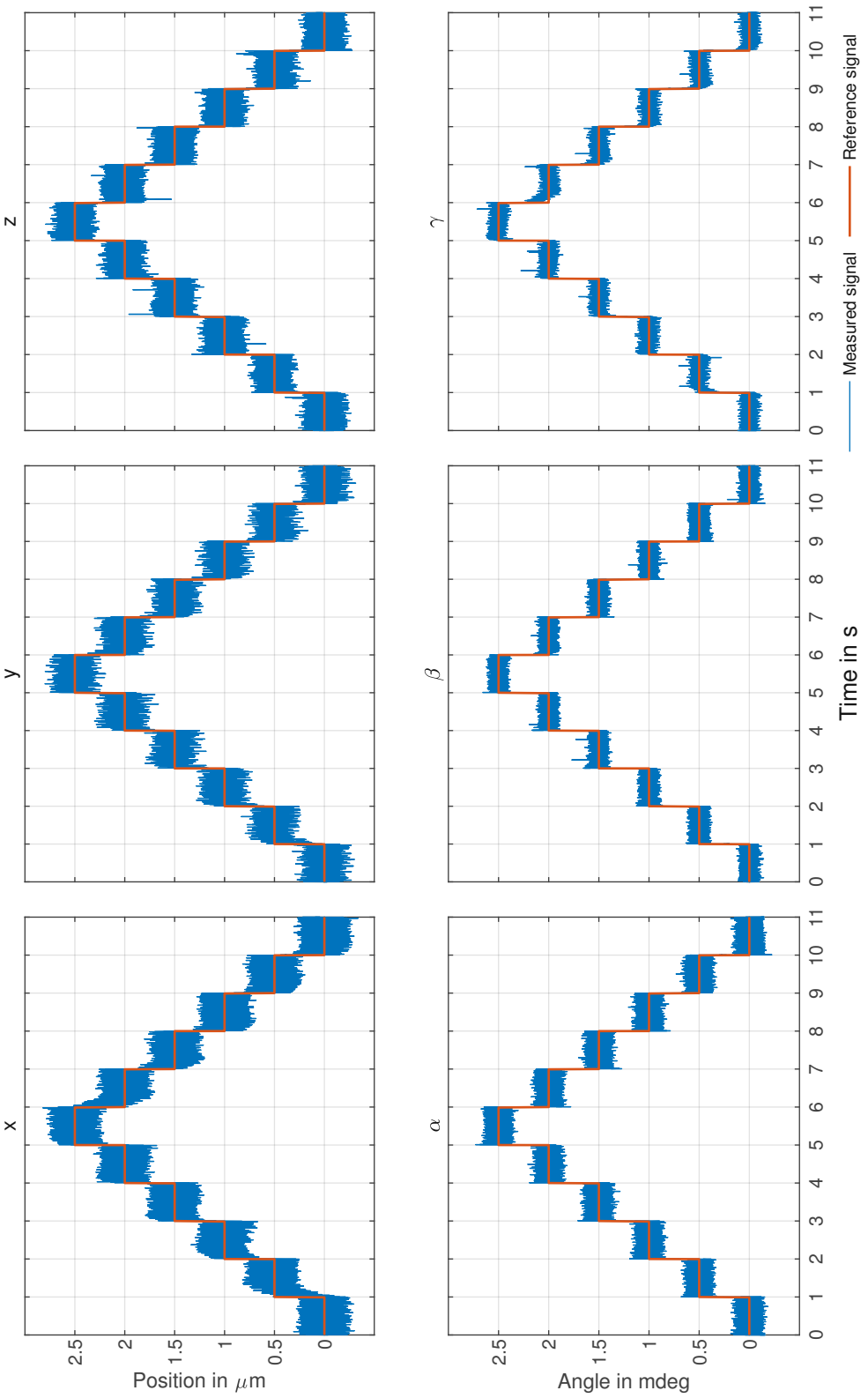

Figure 6.2: Measured position signal of the six main axes for a reference signal with 0.5 µm and 0.5 mdeg steps.

Axis	RMS noise	Axis	RMS noise	
	nm		nrad	µdeg
x	98.4	α	948	54.3
y	87.0	β	658	37.7
z	76.6	γ	657	37.6

Table 6.3: RMS noise of the six main axes with high-bandwidth position control (parameters given in Table 6.1).

6.2 Gravity Compensation

Without gravity compensation, the entire weight of the platform must be supported by the Lorentz actuators. Under a heavy payload, this leads to a high power consumption and heat dissipation, which may not only adversely affect measurements, but also cause damage if the thermal limit of the coils is exceeded. Moreover, if the temperature becomes too high, the permanent magnets are weakened or even lose their magnetisation completely. To avoid this, the EPMs are tuned to minimise the static power consumption of the Lorentz actuators.

Table 6.4 shows the effect of the gravity compensation for two load cases. In the first one, only the weight of the platform, which is 1.88 kg, is lifted and in the second case, an additional load of 4.46 kg is added, resulting in a total payload of 6.34 kg. The table provides the DC current of each Lorentz actuator and the total power consumption, which was calculated by multiplying the squared current with the coil resistance (see Table 4.2).

The measurement results show that the currents are significantly lower in the compensated case. However, they are not exactly zero because, on the one hand, the EPMs were tuned manually until a satisfactory result was achieved and, on the other hand, mutual forces occur between the six actuators due to the limited accuracy of the decoupling transformation. For the negative current values, there is a slight over-compensation, meaning that the Lorentz actuators have to push the mover away from the EPM. Nevertheless, the power consumption could be reduced in both cases by more than 96 %.

Total load	EPM tuning	DC current V1	V2	V3	Total power	Power saving
kg		mA	mA	mA	W	%
1.88	off	225	218	221	3.24	
	on	23	−49	−42	0.10	96.8
6.34	off	820	773	808	42.36	
	on	103	101	43	0.48	98.9

Table 6.4: DC value of the current and total power consumption of the Lorentz actuators for two load cases with and without gravity compensation.

To confirm the results, the total lifting force F_a generated by the EPMs and Lorentz actuators is calculated according to the following equation and compared with the gravitational force of the payload.

$$F_a = \underbrace{\sum_{i=1}^{3} 2\frac{B_{Vi}^2 A}{2\mu}}_{\text{EPMs}} + \underbrace{\sum_{i=1}^{3} K_{Vi} I_{Vi}}_{\substack{\text{Lorentz} \\ \text{actuators}}} \tag{6.1}$$

The reluctance force of the EPMs depends on the squared flux density B_{Vi}, the cross-section $A = 20\,\text{mm} \times 20\,\text{mm}$ of the vertical yoke (in total there are two per EPM) and the magnetic permeability of air $\mu \approx \mu_0 = 4\pi\,10^{-7}\,\text{H/m}$. The flux density values were measured with the integrated Hall sensors and are given in Table 6.5. The force of the Lorentz actuators is calculated by multiplying the motor constant K_{Vi} (see Table 5.5) by the corresponding current I_{Vi} (see Table 6.4).

Table 6.6 provides the values of the total actuator force F_a and the gravitational force $F_g = mg$, where m is the payload mass and $g = 9.81\,\text{m/s}^2$ the gravitational acceleration, for both load cases. The comparison shows that the calculated lifting force is always slightly higher than the force actually required to carry the load. The maximum deviation is just under 12 % and most likely a result of inaccuracies in the measurement of the current and the flux density, which is also not homogeneous across the air gap.

Total load	**Flux density**		
	V1	**V2**	**V3**
kg	**mT**	**mT**	**mT**
1.88	149	155	159
6.34	257	245	255

Table 6.5: Flux density in the air gap of the tuned EPMs for two load cases.

Total load	**EPM tuning**	F_g	F_a	**Deviation**
kg		**N**	**N**	**%**
1.88	off	18.4	19.1	3.7
	on		20.6	11.8
6.34	off	62.2	69.1	11.1
	on		67.8	9.0

Table 6.6: Comparison of the gravitational force F_g and the computed lifting force of the actuators F_a.

6.3 Vibration Isolation

The performance in terms of vibration isolation is evaluated by determining the transmissibility of disturbances from the base to the levitating platform. For this purpose, the frame on which the vibration isolation system is mounted was excited manually while the acceleration sensors measured the motion of the base and the platform. By taking the ratio of the Fourier-transformed time signals, the transmissibility $\mathcal{T}$ is obtained as a function of the discrete frequencies ω_k

$$\mathcal{T}(\omega_k) = \frac{\mathcal{F}\{\ddot{z}_p\,[n]\}(\omega_k)}{\mathcal{F}\{\ddot{z}_b\,[n]\}(\omega_k)} \tag{6.2}$$

where $\ddot{z}_p\,[n]$ and $\ddot{z}_b\,[n]$ denote the discrete acceleration signals measured on the platform and the base respectively. In a final step, the transfer function was smoothed by applying a moving median filter. The measurements were performed for two load cases and different gain values of the acceleration feedback controller.

In the first case, only the platform's weight of 1.88 kg was lifted without gravity compensation. The position controllers of each axis were tuned with a crossover frequency of 6 Hz and $\alpha = 3$. For the vibration suppression, the acceleration feedback controller according to Equation 5.10 was used with the parameters given in Table 5.6. Figure 6.3 shows the magnitude of the transmissibility without active vibration isolation ($g_a = 0$) as well as for a proportional gain $g_a = 2\,\text{kg}$ and $g_a = 4\,\text{kg}$.

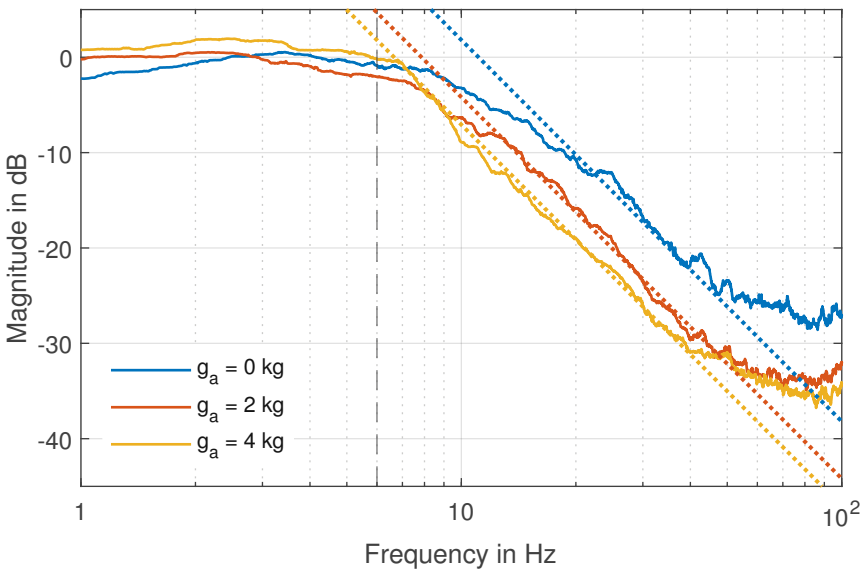

Figure 6.3: Transmissibility of floor vibrations for different values of the acceleration feedback gain g_a without gravity compensation and no additional payload. The dotted lines indicated the fitted mass lines.

For frequencies up to 8 Hz, the transmissibility is close to 0 dB, meaning that no attenuation of disturbances is taking place. This is because the position controller tries to keep the distance between the base and the platform constant within its bandwidth and thus transmits the vibrations from the base to the platform. Above this frequency, the transmissibility decreases by approximately 40 dB/decade in all three cases due to the inertia of the platform mass and the acceleration feedback. As discussed in Section 5.2, the feedback gain g_a corresponds to an additional virtual mass, which pushes the mass line downwards within a certain frequency range, leading to a better attenuation of disturbances. This shift is indicated in Figure 6.3 by the dotted lines, which represent the fitted mass lines. The dashed black line shows the crossover frequency of the position controller in the z-direction.

The shift of the mass line, which corresponds to the additional vibration suppression that is achieved, can be expressed by the ratio v of the real mass m (platform and payload) to the sum of the real and virtual mass, which is generated by the feedback controller and equal to the gain g_a.

$$v = \frac{m}{m + g_a} \tag{6.3}$$

The values given in Table 6.8 show a good agreement between the theoretical and measured results. For a gain $g_a = 2\,\text{kg}$, the amplitude of the transmitted disturbances is additionally reduced by half above 10 Hz compared to the case without active vibration isolation. With $g_a = 4\,\text{kg}$ the reduction amounts to a factor close to three. The value of the gain is limited by the phase margin required for the stability of the acceleration feedback and the structural modes occurring at higher frequencies.

For the second load case, an additional payload of 4.46 kg was placed on the platform, resulting in a total load of 6.34 kg. Since the Lorentz actuators cannot carry the weight permanently, the gravity compensation was tuned accordingly. Due to the changed mass, moment of inertia and stiffness, the position controllers had to be redesigned. As already explained in Section 5.3, the negative stiffness generated by the EPMs sets a lower limit to the bandwidth of the position control in the z-direction. From the blue Bode plot ($k_s = 0$) in Figure 6.4, it can be seen that the amplitude response of the plant's transfer function flattens out below 20 Hz and that the phase shift is $-180°$. Since it is not possible to achieve a crossover and the phase margin required for stability at the same time in this frequency range, the bandwidth of the PID controller can only be set above. Consequently, vibration isolation can only begin at even higher frequencies due to the necessary separation from the position control. This would severely limit the ability to suppress vibrations, which is why the negative stiffness is compensated by another control loop, as shown in Section 5.3. The other Bode plots in Figure 6.4 demonstrate that the stiffness can be increased as required. With $k_s = 35\,\text{N/mm}$ the overall stiffness even becomes positive, resulting in a resonance

peak and phase shift which corresponds to an ordinary mass-spring system. A suitable compensation is achieved with $k_s = 32.7\,\mathrm{N/mm}$, by which the mass line is extended down to 1 to 2 Hz.

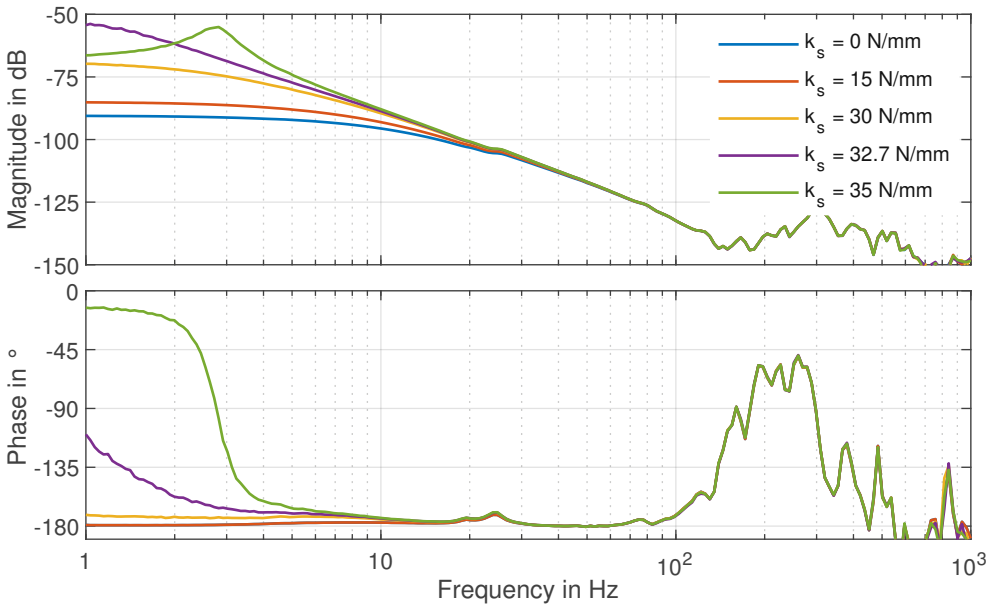

Figure 6.4: Bode plots of the transfer function in the z-direction seen by the position controller for different values of the virtual stiffness k_s when the gravity compensation is tuned to carry 6.34 kg.

Placing an additional payload on the platform, not only changes the total mass, but also the moments of inertia and the location of the centre of gravity. This must be taken into account both for the tuning of the controllers and for the matrices V and W from Sections 3.5.2 and 3.5.3, which are required for the decoupling of the DoFs. The changed parameters for the second load case are given in Table 6.7.

m	6.34 kg	J_x	$24.91\,\mathrm{gm^2}$
x_s	0 mm	J_y	$24.88\,\mathrm{gm^2}$
y_s	0 mm	J_z	$42.63\,\mathrm{gm^2}$
z_s	71 mm		

Table 6.7: Load-dependent model parameter values with additional payload

The implemented stiffness compensation allows the position controller of the z-axis to be tuned as before with a crossover frequency of 6 Hz and $\alpha = 3$. However, the slow controller is not suitable to move the platform to the operating point, because the negative stiffness has a non-linear dependence on the position of the platform, and is only compensated correctly at the operating point. For the same reason, the crossover frequency is not reduced

further, as the controller might get unstable if the excitations are too large. Therefore, all position controllers are tuned with a crossover frequency of 12 Hz and $\alpha = 3$. This faster position control is used to move the platform into its operating point. Subsequently, the stiffness compensation is set to $k_s = 32.7\,\mathrm{N/mm}$, and finally the crossover frequency of the controller for the z-axis is reduced to 6 Hz. For robustness, the other controllers are not changed.

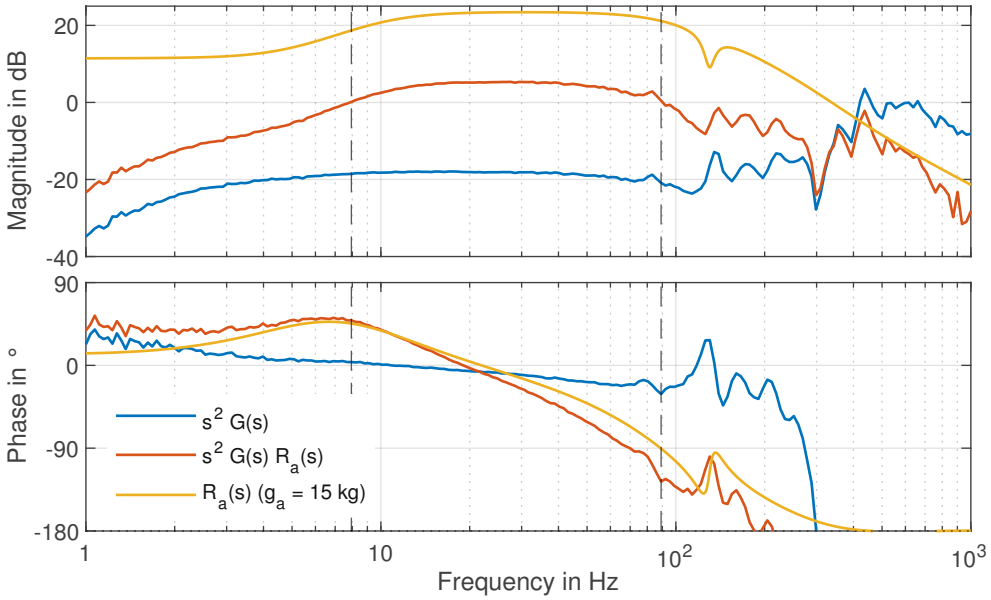

Figure 6.5: Bode plots of the plant in the z-direction seen by the acceleration feedback controller R_a (blue), the open-loop transfer function (red), and the acceleration feedback controller R_a with a gain $g_a = 15\,\mathrm{kg}$ (yellow).

The acceleration feedback controller is designed similarly to Section 5.2 and shown in Figure 6.5. At low frequencies, a lead compensator reduces the gain in order to achieve a separation from the position control, and at higher frequencies the modes are attenuated by a low-pass filter and additional notch filters. In addition to the Bode plot of the controller, Figure 6.5 also shows the unfiltered and filtered transfer function of the plant measured with the acceleration sensor. With a gain $g_a = 15\,\mathrm{kg}$, the open-loop transfer function has two crossings of the 0 dB-line, which are indicated by the black dashed lines.

As before, the transmissibility was determined with this controller for different values of the feedback gain g_a. The results in Figure 6.6 show again that the acceleration feedback results in a downward shift of the mass line. A major difference, however, is that the measured transmissibility is significantly below 0 dB for low frequencies. This is not a consequence of the vibration isolation, but is due to the fact that no sufficient excitation was possible in this frequency range and the measurement is therefore not accurate. The shift of the mass line caused by the additional virtual mass is again indicated by the fitted

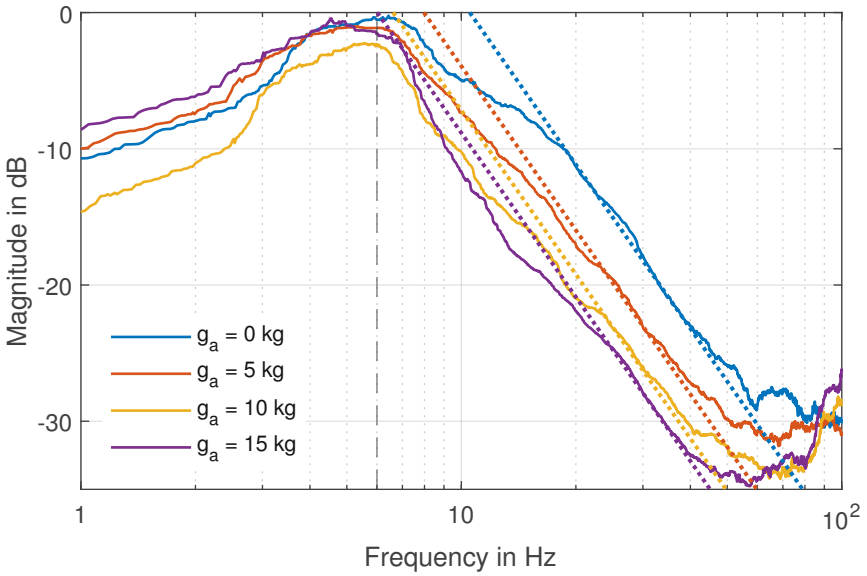

Figure 6.6: Transmissibility of floor vibrations for different values of the acceleration feedback gain g_a with gravity compensation and a total load of 6.34 kg. The dotted lines indicated the fitted mass lines.

dotted lines, which verify the expected behaviour. The dashed black line indicates the crossover frequency of the position controller in z-direction. The numerical values given in Table 6.8 and the Bode plots in Figure 6.6 show that a similar vibration suppression was achieved as in the previous load case. This is because the same bandwidth was chosen for the position controller of the z-axis, and the mass ratios are also similar. A higher gain than $g_a = 15\,\text{kg}$ could not be achieved due to structural modes. Nevertheless, the transmissibility is reduced by almost 10 dB compared to the case without acceleration feedback.

Total load m	**Feedback gain g_a**	**Theoretical mass ratio v**		**Fitted mass ratio**	
kg	**kg**		**dB**		**dB**
1.88	0	1	0	1	0
	2	0.48	−6.3	0.50	−6.0
	4	0.32	−9.9	0.36	−8.9
6.34	0	1	0	1	0
	5	0.56	−5.1	0.57	−4.8
	10	0.39	−8.2	0.40	−8.1
	15	0.30	−10.5	0.33	−9.7

Table 6.8: Shift of the mass line by active vibration isolation for two load cases and different values of the acceleration feedback gain g_a.

Chapter 7

Conclusion and Outlook

In this thesis, the design, assembly and control of a vibration isolation system with a levitating 6-DoF platform and zero-power gravity compensation was demonstrated. The first part of this chapter presents the main conclusions and answers the research questions posed in Section 2.6. In the second part, an outlook is given on possible further research topics and improvements of the prototype.

7.1 Conclusion

Based on the requirements stated in Section 1.2, an experimental setup was implemented. The main component is the vibration isolation system, consisting of a base and a levitating platform with six DoFs. For the actuation of the out-of-plane DoFs (z, α, β) and the gravity compensation, three Lorentz actuators with integrated EPMs were built based on the design of [53]. These enable both dynamic motion and compensation of a static force. For the tuning of the three EPMs, a current pulse generator is used. Furthermore, the vibration isolation system is equipped with sensors to measure the position of the platform, the flux density in the EPMs, and the acceleration, which is required for the suppression of disturbances.

The control of the vibration isolation system was implemented on a rapid prototyping system. This includes position control, readout of the acceleration sensors via SPI, control of the current pulse generator by the FPGA, acceleration feedback control and stiffness compensation. Due to the levitation, the identification of the platform dynamics was only possible in closed-loop operation. This required a reliable model, based on which the position control was designed. Following the identification, the controllers required for vibration isolation were implemented (see Sections 5.2 and 5.3). The results of the measurements and performance evaluations carried out on the prototype are presented in Chapter 6. Based on this, the research questions posed in Section 2.6 are answered below.

First research question

> *Is it feasible to design a levitating platform with six DoFs that can be positioned without static power consumption at an arbitrary operating point, independent of the payload?*

As explained in Chapter 3, the positioning of a platform with six DoFs requires at least six actuators and displacement sensors. The separate actuation and measurement of each individual DoF independently of the others would lead to a rather complex design. Thus, there is usually a coupling between the DoFs. In order to implement decentralised control, which only requires six independent SISO controllers, it is necessary to decouple the axes. This is achieved by a transformation of the actuator forces and sensor signals, as shown in Sections 3.5.2 and 3.5.3. This approach allows robust position control of the out-of-plane DoFs with a bandwidth of around 60 Hz and a resolution of 77 nm (see Section 6.1).

In Section 6.2, the gravity compensation was evaluated for two load cases: First, only for the weight of the platform (1.88 kg) was compensated. Then an additional payload of 4.46 kg was placed on the platform, resulting in a total load of 6.34 kg. In both cases, the platform was positioned at the same operating point. By tuning the EPMs, the power consumption could be reduced by about 97 %. The remaining energy consumption is a result of the manual tuning and the mutual forces of the actuators due to inaccuracies of the assembly. Therefore, the answer to the above question is that it is possible to achieve at least an almost zero-power gravity compensation at an arbitrary operating point.

Second research question

> *Can position control, magnetic levitation with zero-power gravity compensation and active vibration suppression be achieved at the same time?*

A key aspect that had to be taken into account when designing the control in Chapter 5 is the influence of position control on vibration suppression. On the one hand, it is needed to keep the levitating platform at its operating point, but on the other hand, it transmits ground vibrations within its bandwidth. Moreover, the acceleration feedback used to improve the suppression of disturbances can only be active above the position control bandwidth, which should therefore be chosen as low as possible. This, however, is limited by the negative stiffness created by the EPMs, which necessitates the compensation by a virtual positive stiffness (see Section 5.3).

By compensating the negative stiffness, it was possible to set the bandwidth of the position control in the z-direction to 6 Hz. This resulted in a transmissibility with a cutoff frequency of about 8 Hz and a slope of -40 dB/decade (see Section 6.3). The performance of the vibration isolation was evaluated for two load cases. By applying acceleration feedback above the position control bandwidth, it was possible to more than triple the effective mass.

This resulted in a downwards shift of the mass line, and thus improved the suppression of vibrations by a factor of three. These results show that it is possible to integrate position control, gravity compensation and active vibration suppression with proposed control design.

7.2 Outlook

The experimental setup allows the implementation of more complex control strategies. In this thesis, the accelerometers mounted on the base were only used to evaluate the transmissibility, but they also enable the use of feedforward control. With this approach, floor vibrations are measured directly and are then compensated by the actuators (see Section 2.2.2). Potentially, this could further improve the vibration suppression but requires the accurate knowledge of the transmissibility [11].

Another improvement concerns the tuning of the EPMs, which could be done automatically, when a payload is added to or removed from the platform. This requires a more sophisticated position control, as it must adapt to the unknown mass of the payload, and also be able to suppress the impacts that occur during the tuning of the EPMs. Moreover, in static operation the bandwidth should be as low as possible in order not to transmit floor vibrations.

Currently, the reduction of the position control bandwidth is limited by the robustness of the stiffness compensation. The negative stiffness of the EPMs depends non-linearly on the position of the platform and on the magnetisation state of the EPMs, which is adjusted to the weight of the payload. Therefore, an adaptive stiffness compensation would have to take both into account. This could be achieved by using the measurement of the platform position and the flux density in the air gaps of the EPMs in combination with a suitable model.

Bibliography

[1] H. Bachmann and W. Ammann, *Vibrations in Structures, Induced by Man and Machines* (Structural Engineering Documents). Zürich, Switzerland: International Association for Bridge and Structural Engineering, 1987, vol. 3e.

[2] E. I. Rivin, *Passive Vibration Isolation*. New York, NY, USA: ASME Press, 2003.

[3] M. F. Heertjes, H. Butler, N. J. Dirkx *et al.*, 'Control of Wafer Scanners: Methods and Developments,' in *Proceedings of the 2020 American Control Conference (ACC)*, (Denver, CO, USA, 1st–3rd Jul. 2020), 2020, pp. 3686–3703.

[4] H. Butler, 'Position Control in Lithographic Equipment, An Enabler for Current-Day Chip Manufacturing,' *IEEE Control Systems Magazine*, vol. 31, no. 5, pp. 28–47, 2011.

[5] W. B. Hakvoort and M. A. Beijen, 'Filtered-error RLS for self-tuning disturbance feedforward control with application to a multi-axis vibration isolator,' *Mechatronics*, vol. 89, p. 102 934, 2023.

[6] D. Wertjanz, E. Csencsics, T. Kern and G. Schitter, 'Bringing the Lab to the Fab: Robot-Based Inline Measurement System for Precise 3-D Surface Inspection in Vibrational Environments,' *IEEE Transactions on Industrial Electronics*, vol. 69, no. 10, pp. 10 666–10 673, 2022.

[7] S. Ito, S. Unger and G. Schitter, 'Vibration isolator carrying atomic force microscope's head,' *Mechatronics*, vol. 44, pp. 32–41, 2017.

[8] R. DeRosa, J. C. Driggers, D. Atkinson *et al.*, 'Global feed-forward vibration isolation in a km scale interferometer,' *Classical and Quantum Gravity*, vol. 29, no. 21, pp. 215 008–215 020, 2012.

[9] B. Sedghi, P. Zuluaga-Ramírez, U. Lampater *et al.*, 'ESO ELT - vibration sources characterization: a step forward towards requirement and performance verification,' in *Modeling, Systems Engineering, and Project Management for Astronomy IX*, (Online Only, USA, 14th–18th Dec. 2020), 2020, pp. 27–39.

[10] S. Hol, E. Lomonova and A. Vandenput, 'Design of a magnetic gravity compensation system,' *Precision Engineering*, vol. 30, no. 3, pp. 265–273, 2006.

[11] M. A. Beijen, 'Disturbance feedforward control for vibration isolation systems: analysis, design, and implementation,' Department of Mechanical Engineering, Ph.D. dissertation, Technische Universiteit Eindhoven, Eindhoven, 2018.

[12] C. M. Harris and A. G. Piersol, Eds., *Harris' Shock and Vibration Handbook*, 5. ed., New York, NY, USA: McGraw-Hill, 2002.

[13] P. K. Subrahmanyan, 'A Modal Approach to Precision Motion Control,' Department of Mechanical Engineering, Ph.D. dissertation, Massachusetts Institute of Technology, Cambridge, MA, USA, 1999.

[14] C. Erin, B. Wilson and J. Zapfe, 'An improved model of a pneumatic vibration isolator, Theory and experiment,' *Journal of Sound and Vibration*, vol. 218, no. 1, pp. 81–101, 1998.

[15] D. L. Platus, 'Negative-stiffness-mechanism vibration isolation systems,' in *Proceesings of SPIE's International Symposium on Optical Science, Engineering, and Instrumentation*, (Denver, CO, USA, 18th Jul. 1999), 1999, pp. 98–105.

[16] 'VIBe™ VIP100 Super Compact Mechanical Vibration Isolation Platforms,' Newport Corporation. (2023), [Online]. Available: https://www.newport.com/f/vip100-super-compact-mechanical-vibration-isolation-platform (visited on 19th Dec. 2023).

[17] 'Zeiss Microscope Isolation Platforms,' Newport Corporation. (2023), [Online]. Available: https://www.newport.com/f/zeiss-microscope-isolation-platforms (visited on 19th Dec. 2023).

[18] 'Optical Table Supports: Active Vibration Isolation,' Thorlabs. (2023), [Online]. Available: https://www.thorlabs.com/newgrouppage9.cfm?objectgroup_id=1095 (visited on 19th Dec. 2023).

[19] C. Collette, S. Janssens and K. Artoos, 'Review of Active Vibration Isolation Strategies,' *Recent Patents on Mechanical Engineering*, vol. 4, no. 3, pp. 212–219, 2011.

[20] C. R. Fuller, *Active Control of Vibration*. Oxford, U.K.: Elsevier Science & Technology, 1996.

[21] R. M. Schmidt, G. Schitter, A. Rankers and J. van Eijk, *The Design of High Performance Mechatronics, High-Tech Functionality by Multidisciplinary System Integration*, 2nd revised edition. Amsterdam, Netherlands: IOS Press under the imprint Delft University Press, 2014.

[22] D. Karnopp, M. J. Crosby and R. A. Harwood, 'Vibration Control Using Semi-Active Force Generators,' *Journal of Engineering for Industry*, vol. 96, no. 2, pp. 619–626, 1974.

[23] C. Collette and F. Matichard, 'Sensor fusion methods for high performance active vibration isolation systems,' *Journal of Sound and Vibration*, vol. 342, pp. 1–21, 2015.

[24] M. A. Beijen, M. F. Heertjes, H. Butler and M. Steinbuch, 'Mixed feedback and feedforward control design for multi-axis vibration isolation systems,' *Mechatronics*, vol. 61, pp. 106–116, 2019.

[25] A. Preumont, M. Horodinca, I. Romanescu *et al.*, 'A six-axis single-stage active vibration isolator based on Stewart platform,' *Journal of Sound and Vibration*, vol. 300, no. 3-5, pp. 644–661, 2007.

[26] T. Zhu, 'Six degree of freedom active vibration isolation using quasi-zero stiffness magnetic levitation,' Department of Mechanical Engineering, Ph.D. dissertation, University of Adelaide, Adelaide, 2013.

[27] M. A. Beijen, R. Voorhoeve, M. F. Heertjes and T. Oomen, 'Experimental estimation of transmissibility matrices for industrial multi-axis vibration isolation systems,' *Mechanical Systems and Signal Processing*, vol. 107, pp. 469–483, 2018.

[28] S. Ito and G. Schitter, 'Comparison and Classification of High-Precision Actuators Based on Stiffness Influencing Vibration Isolation,' *IEEE/ASME Transactions on Mechatronics*, vol. 21, no. 2, pp. 1169–1178, 2016.

[29] A. Preumont, *Mechatronics, Dynamics of electromechanical and piezoelectric systems*. Dordrecht, Netherlands: Springer, 2006, vol. 136.

[30] D. Wertjanz, E. Csencsics and G. Schitter, 'Three-DoF Vibration Compensation Platform for Robot-Based Precision Inline Measurements on Free-Form Surfaces,' *IEEE Transactions on Industrial Electronics*, vol. 69, no. 1, pp. 613–621, 2022.

[31] C. C. Ding, 'Vibration isolation control of a contactless electromagnetic suspension system,' Department of Electrical Engineering, Ph.D. dissertation, Technische Universiteit Eindhoven, Eindhoven, 2013.

[32] G. Stadler, E. Csencsics, S. Ito and G. Schitter, 'High Precision Hybrid Reluctance Actuator With Integrated Orientation Independent Zero Power Gravity Compensation,' *IEEE Transactions on Industrial Electronics*, vol. 69, no. 12, pp. 13 296–13 304, 2022.

[33] S. J. Rupitsch, *Piezoelectric Sensors and Actuators, Fundamentals and applications*. Berlin, Germany: Springer, 2019.

[34] F. Tajdari, A. P. Berkhoff, M. Naves, M. Nijenhuis and A. de Boer, 'A low-profile flexural displacement-converter mechanism for piezoelectric stack actuators,' *Sensors and Actuators A: Physical*, vol. 313, p. 112 198, 2020.

[35] C. Collette, S. Janssens, K. Artoos and C. Hauviller, 'Active vibration isolation of high precision machines,' *Diamond Light Source Proceedings*, vol. 1, no. MEDSI-6, 2010.

[36] C. Collette, S. Janssens, P. Fernandez-Carmona *et al.*, 'Review: Inertial Sensors for Low-Frequency Seismic Vibration Measurement,' *Bulletin of the Seismological Society of America*, vol. 102, no. 4, pp. 1289–1300, 2012.

[37] N. Ackerley, 'Principles of Broadband Seismometry,' in *Encyclopedia of Earthquake Engineering*, M. Beer, I. A. Kougioumtzoglou, E. Patelli and S.-K. Au, Eds., Berlin, Heidelberg, Germany: Springer, 2015, pp. 1941–1970.

[38] G. Alguacil and J. Havskov, 'Passive Seismometers,' in *Encyclopedia of Earthquake Engineering*, M. Beer, I. A. Kougioumtzoglou, E. Patelli and I. S.-K. Au, Eds., Berlin, Heidelberg, Germany: Springer, 2021, pp. 1–17.

[39] J. G. Korvink and O. Paul, Eds., *MEMS, A Practical Guide to Design, Analysis, and Applications*, Norwich, NY, USA: William Andrew, 2006.

[40] G. Alguacil and J. Havskov, 'Seismic Accelerometers,' in *Encyclopedia of Earthquake Engineering*, M. Beer, I. A. Kougioumtzoglou, E. Patelli and S.-K. Au, Eds., Berlin, Heidelberg, Germany: Springer, 2015, pp. 2504–2519.

[41] D. Cardarelli, 'An integrated MEMS inertial measurement unit,' in *Proceedings of the 2002 IEEE Position Location and Navigation Symposium*, (Palm Springs, CA, USA, 15th–18th Apr. 2002), 2002, pp. 314–319.

[42] A. J. Fleming, 'A review of nanometer resolution position sensors: Operation and performance,' *Sensors and Actuators A: Physical*, vol. 190, pp. 106–126, 2013.

[43] W. Gao, S. W. Kim, H. Bosse *et al.*, 'Measurement technologies for precision positioning,' *CIRP Annals*, vol. 64, no. 2, pp. 773–796, 2015.

[44] 'capaNCDT, Capacitive displacement sensors and systems,' Micro-Epsilon Messtechnik. (2023), [Online]. Available: https://www.micro-epsilon.de/download/products/cat--capaNCDT--en.pdf (visited on 4th Dec. 2023).

[45] 'eddyNCDT, Inductive sensors based on eddy currents,' Micro-Epsilon Messtechnik. (2023), [Online]. Available: https://www.micro-epsilon.de/download/products/cat--eddyNCDT--de.pdf (visited on 4th Dec. 2023).

[46] G. A. Reider, *Photonik, Eine Einführung in die Grundlagen*, 4. Auflage. Berlin, Heidelberg, Germany: Springer Vieweg, 2022.

[47] 'Displacement Measuring Interferometer, Datasheet,' attocube systems. (2023), [Online]. Available: https://www.attocube.com/downloads/displacement-measuring-interferometer.pdf (visited on 4th Dec. 2023).

[48] J. Janssen, J. Paulides, E. A. Lomonova, B. Delinchant and J.-P. Yonnet, 'Design study on a magnetic gravity compensator with unequal magnet arrays,' *Mechatronics*, vol. 23, no. 2, pp. 197–203, 2013.

[49] T. Zhu, B. Cazzolato, W. S. Robertson and A. Zander, 'Vibration isolation using six degree-of-freedom quasi-zero stiffness magnetic levitation,' *Journal of Sound and Vibration*, vol. 358, pp. 48–73, 2015.

[50] S. Earnshaw, 'On the Nature of the Molecular Forces which Regulate the Constitution of the Luminiferous Ether,' *Transactions of the Cambridge Philosophical Society*, vol. 7, p. 97, 1848.

[51] M. Raab, M. Hutter, A. Kazi, W. Schinkoethe and B. Gundelsweiler, 'Magnetically Levitated Linear Drive Using an Active Gravity Compensation Based on Hybrid Shape Memory Actuators,' *IEEE/ASME Transactions on Mechatronics*, vol. 26, no. 3, pp. 1380–1391, 2021.

[52] A. N. Knaian, 'Electropermanent Magnetic Connectors and Actuators, Devices and Their Application in Programmable Matter,' Department of Electrical Engineering and Computer Science, Ph.D. dissertation, Massachusetts Institute of Technology, Cambridge, MA, USA, 2010.

[53] A. Pechhacker, D. Wertjanz, E. Csencsics and G. Schitter, 'Integrated electromagnetic actuator with adaptable zero power gravity compensation,' *IEEE Transactions on Industrial Electronics*, pp. 1–9, 2023.

[54] A. Pechhacker, D. Wertjanz, E. Csencsics and G. Schitter, 'Model-based flux control of an electropermanent magnet for adaptive zero power gravity compensation,' *IFAC-PapersOnLine*, vol. 56, no. 2, pp. 5352–5357, 2023.

[55] W. Heywang and R. Müller, *Sensorik*. Berlin, Heidelberg, Germany: Springer, 1993.

[56] K.-H. Grote, B. Bender and D. Göhlich, *Dubbel, Taschenbuch für den Maschinenbau*, 25. Auflage. Berlin, Heidelberg, Germany: Springer Vieweg, 2018.

[57] 'Linear Voice Coil Actuators AVM,' TDS Precision Products. (2021), [Online]. Available: https://www.tds-pp.com/fileadmin/user_upload/datenblatt/aktuatoren/Voice_Coil_motor_AVM.pdf (visited on 12th Nov. 2023).

[58] G. H. Ravell, 'An overview of magnet processing,' in *Proceedings of the Electrical Electronics Insulation Conference and Electrical Manufacturing & Coil Winding Conference*, (Rosemont, IL, USA, 18th–21st Sep. 1995), 1995, pp. 69–71.

[59] 'eddyNCDT 3700, Instruction Manual,' Micro-Epsilon Messtechnik. (2010), [Online]. Available: https://www.micro-epsilon.com/download/man_archiv/man--eddyNCDT-3700--en.pdf (visited on 1st Dec. 2023).

[60] 'ADXL354/ADXL355,' Analog Devices. (2020), [Online]. Available: https://www.analog.com/media/en/technical-documentation/data-sheets/adxl354_adxl355.pdf (visited on 1st Dec. 2023).

[61] 'ADXRS290, Datasheet,' Analog Devices. (2014), [Online]. Available: https://www.analog.com/media/en/technical-documentation/data-sheets/ADXRS290.pdf (visited on 1st Dec. 2023).

[62] 'LSM6DSRX, Datasheet,' STMicroelectronics. (2020), [Online]. Available: https://www.st.com/resource/en/datasheet/lsm6dsrx.pdf (visited on 1st Dec. 2023).

[63] 'HE144, Datasheet,' Asensor Technology. (2017), [Online]. Available: https://asensor.eu/onewebmedia/Datasheet-HE144X.pdf (visited on 1st Dec. 2023).

[64] E. Csencsics and G. Schitter, 'Parametric PID controller tuning for a fast steering mirror,' in *Proceedings of the 2017 IEEE Conference on Control Technology and Applications (CCTA)*, (Mauna Lani Resort, HI, 27th–30th Aug. 2017), 2017, pp. 1673–1678.

[65] E. Wernholt and S. Gunnarsson, 'On the use of a multivariable frequency response estimation method for closed loop identification,' in *Proceedings of the 43rd IEEE Conference on Decision and Control*, (Nassau, Bahamas, 14th–17th Dec. 2004), 2004, 827–832 Vol.1.

[66] S. Skogestad and I. Postlethwaite, *Multivariable Feedback Control, Analysis and Design*, 2nd ed. Chichester: John Wiley & Sons, 2005.

Eigenständigkeitserklärung

Hiermit erkläre ich, dass die vorliegende Arbeit gemäß dem *Code of Conduct - Regeln zur Sicherung guter wissenschaftlicher Praxis*, insbesondere ohne unzulässige Hilfe Dritter und ohne Benutzung anderer als der angegebenen Hilfsmittel, angefertigt wurde. Die aus anderen Quellen direkt oder indirekt übernommenen Daten und Konzepte sind unter Angabe der Quelle gekennzeichnet. Die Arbeit wurde bisher weder im In- noch im Ausland in gleicher oder ähnlicher Form in anderen Prüfungsverfahren vorgelegt.

Wien, im Dezember 2023

Benjamin Friedl, BSc, BSc (WU)